RETURN MAP CHARACTERIZATIONS OF SINGULAR SOLUTIONS FOR A MODEL OF BURSTING WITH TWO SLOW VARIABLES.

by

Roger Evan Griffiths

A dissertation submitted in partial fullfillment
of the requirements for the degree

of

Doctor of Philosophy

in

Mathematical Sciences

MONTANA STATE UNIVERSITY
Bozeman, Montana

July 2003

©COPYRIGHT

by

Roger Evan Griffiths

2003

All Rights Reserved

APPROVAL

of a dissertation submitted by

Roger Evan Griffiths

This dissertation has been read by each member of the dissertation committee and has been found to be satisfactory regarding content, English usage, format, citations, bibliographic style, and consistency, and is ready for submission to the college of Graduate Studies.

Dr. Mark C. Pernarowski _____ _____
(Signature) Date

Approved for Department of Mathematical Sciences

Dr. Kenneth Bowers _____ _____
(Signature) Date

Approved for the College of Graduate Studies

Dr. Bruce R. McLeod _____ _____
(Signature) Date

STATEMENT OF PERMISSION TO USE

In presenting this dissertation in partial requirements for a doctoral degree at Montana State University, I agree that the Library shall make it available to borrowers under rules of the Library. I further agree that copying of this dissertation is allowable only for scholarly purposes, consistent with "fair use" as prescribed in the U.S. Copyright Law. Requests for extensive copying or reproduction of this dissertation should be referred to Bell & Howell Information and Learning, 300 North Zeeb Road, Ann Arbor, Michigan 48106, to whom I have granted "the exclusive right to reproduce and distribute my dissertation in and from microform along with the non-exclusive right to reproduce and distribute my abstract in any format in whole or in part."

Signature _____

Date _____

ACKNOWLEDGMENTS

First, I would like to thank my advisor, Dr. Mark Pernarowski. I feel fortunate to have had the opportunity to work with him and truly appreciate his commitment to my project and his time, assistance, sense of humor and patience. To detail all of his efforts would require another volume, which might be more interesting to read.

Third, a special thanks to my readers Dr. Jack Dockery, and Dr. Tomas Gedeon for their helpful suggestions and corrections.

I am indebted to many educators, but mention only a few here. I wish to thank Gary Grefsrud for, among many things, directing me to Montana State University to work with such a wonderful group of mathematicians. J. Arnott for his help on the hard stuff. Tom Schaffter who has been an inspiration in more ways than he realizes.

I thank my family for teaching me by example the many character traits (disorders) that one must have to complete a project such as this. Thanks Mom for not really trading me for that bowl of gold fish, and thanks Dad for your continued interest in 'non-apologetic linear chaotic non-dynamical systems'.

To my widow, Lina you can dig me up now, turns out I was not dead after all. I would like to thank her for her continuous love and faith in my ability to finish. She did the worrying for me. And finally, my daughter Sofia, for her tight grip on my heart, which always kept life in its proper perspective, and without whom this would have had a 2002 copy write.

TABLE OF CONTENTS

LIST OF TABLES vi

LIST OF FIGURES vii

1. INTRODUCTION 1

History and Motivation 3
Analysis, Background and Overview 7

2. MODEL DEFINITIONS AND DEVELOPMENT 11

Model definition 12
Subsystem derivation/definitions 15
Parameter Classification 33
Equilibria 37

3. THE RETURN MAP 55

Overview 55
Construction of the Map 58
Degenerate Case 61

4. NUMERICAL CONSTRUCTION OF THE RETURN MAP 73

Overview of Numerical Methods Used 73
Evaluation of the numerical methods 84

5. ISSUES AND APPLICATION OF THE RETURN MAP 89

Map composition issues 90
Domain issues 91
Bistability 106
Another Example 112

6. CONCLUSIONS AND FUTURE WORK 116

REFERENCES CITED 119

LIST OF TABLES

Table		Page
1	Two slow variable model variations (overview)	36
2	Dependence of (SS) equilibria on parameters.	45
3	(SS) Parameter sets	75

LIST OF FIGURES

Figure		Page
1	Examples of bursting	2
2	Representation of an activation variable	7
3	Square wave bursting	12
4	Fast subsystem bifurcation diagram	16
5	Bifurcation diagram - when z is an inactivation variable	19
6	FS parameter selection diagram.	35
7	Region of the SS parameter diagram where there exist three equilibria of (FULL).	38
8	The partition of the SS parameter diagram, based on the location of equilibria on $\mathcal{S}_U$, $\mathcal{S}_M$ or $\mathcal{S}_L$.	40
9	The SS parameter diagram.	41
10	Bifurcation diagram in the bifurcation parameter τ_1.	49
11	SS parameter diagram with Hopf bifurcation curve superimposed.	51
12	Slow flow near a Hopf point.	52
13	Bifurcation diagram in the bifurcation parameter β_2.	53
14	Caricature of the return map definition	58
15	Caricature of the one dimensional return map definition.	60
16	Projection of the invariant subspace onto the (x, y)-plane, in the degenerate case.	64
17	Illustration of the global attraction of projected trajectories, in the degenerate case.	65
18	Projected trajectories on S_L associated with the singular map in the degenerate $\tau_1 = \tau_2$ case.	67

19 Projected active phase trajectories associated with the singular map in the degenerate $\tau_1 = \tau_2$ case. 70

20 SS parameter diagram indicating the location of equilibria for the two parameter sets used throughout this chapter. 74

21 A caricature of $\widetilde{\phi}$ (SS), projected onto the (x, y)-plane. 77

22 Map $\widetilde{\phi}(x)$ generated numerically using AUTO. 78

23 $\widehat{u}(z)$ plotted as AUTO generated data along with our fitted function. 81

24 Map $\widehat{\phi}(x)$ generated numerically using AUTO 82

25 The map ϕ as the composition of $\widetilde{\phi}(x)$ with $\widehat{\phi}(x)$. 83

26 Comparison of the numerical computations of $\widehat{\phi}(x)$ (AUTO vs Matlab). 85

27 Verification of the fixed point $\bar{x} = \phi(\bar{x})$ obtained in the map composition for both the $(+,+)$ and $(+,-)$ cases. 87

28 An active phase trajectory of (FULL) projected onto the (x, y)-plane along with the explicit $\widehat{u}(z)$ function. 88

29 Another (AFS)-(FULL) comparison. 88

30 A bursting cycle projected onto the (x, y)-plane illustrating an alternate definition of the map ϕ: $\phi_a = \widehat{\phi} \circ \widetilde{\phi}$. 90

31 (SS) nullclines in the $(+,-)$ case. 93

32 The normal vectors $\mathbf{N}_-$ and $\mathbf{N}_+$, orthogonal to an arbitrary Γ_u. . . . 94

33 Several (SS) trajectories along with a plot of the curve $\widetilde{C}_{\text{SS}}$ in the $(+,-)$ case. 96

34 (AFS) nullclines in the $(+,-)$ case. 98

35 Several (AFS) trajectories along with a plot of the curve $\widehat{C}_{\text{AFS}}$. 99

36 Summary of the range information for the $(+,-)$ example. 101

37 Numerical verification of Theorem 5.1 (i). 102

38 A tangency example in the (SS) of the $(+,+)$ case 103

39 A generic example of a single unstable equilibrium on $\mathcal{S}_L$. 105

40 A generic example of a single stable equilibrium on $\mathcal{S}_L$. 106

41 Caricature of a generic bistability example. 107

42 Bistability: bursting solutions. 108

43 Bistability: The stable equilibrium on $\mathcal{S}_L$. 109

44 SS Parameter diagram for the bistable example 110

45 Numerical map construction of this bistability example. 111

46 A last example. 113

47 Numerical map construction of this example. 115

ABSTRACT

Various physiological systems display bursting electrical activity (BEA). There exist numerous three variable models to describe this behavior. However, four variables may be required to explain some qualitative features of the BEA.

In this dissertation a model with two slow and two fast variables is presented. For some parameter values the system has stable equilibria while for other values there exist bursting solutions. A singular construction of the latter solutions corresponds to the existence of a fixed point of a one dimensional map. The map is the composition of two maps derived from the slow-subsystem and the averaged fast-subsystem. In a degenerate case this fixed point is determined. For non-degenerate cases numerical methods for calculating these maps will be presented.

CHAPTER 1

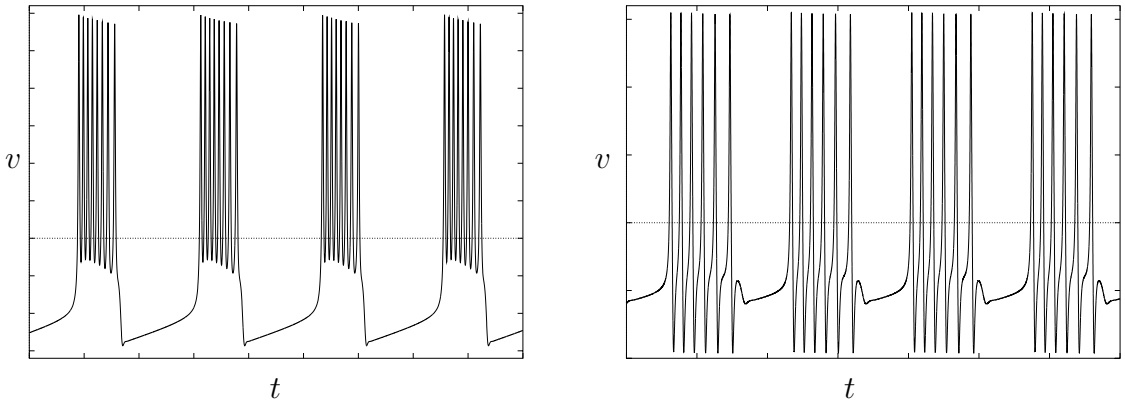
INTRODUCTION

Generally when discussing electrical activity of cells, the cells may be organized into two groups, excitable cells and nonexcitable cells. Nonexcitable cells tend to maintain a stable equilibrium potential. Excitable cells, on the other hand, respond in an 'all or nothing' fashion and when an applied current is sufficiently strong the cell responds via a large excursion in cell membrane potential (action potential). Examples of excitable cells include, most neurons and muscle cells, and secretory cells. This excitatory type of cell will be dealt with in this work. Examples of excitability in nature include a household match and, as a continuous example, a fuse [32].

The electrical activity of all cells depends on the movement of charge in the form of ionic currents across the plasma membrane. The specific mechanisms of ion transport are not the subject of this work, but are well described in books such as From Neuron to Brain [40], The Neuron [37] and Neuroscience [46]. These three books are also the primary reference for the other aspects of neuroscience discussed through out this work.

Bursting electrical activity (bursting) in cells is the phenomenon in which the membrane potential of the cell goes through a succession of alternating active (spiking) and silent states, illustrated in Figure 1. Bursting is characterized by a period of rapid oscillations interspersed with quiescent periods during which the membrane potential changes slowly. Bursting was first observed in the electrical activity of the Aplysia R-15 neuron (1967) [57], [1].

The Hodgkin-Huxley model [25] is the first model of excitability of cellular electrical activity based on ionic mechanisms and is considered the most important



Square-Wave Bursting Nearly parabolic Bursting

Figure 1: Some examples of bursting, with their classification type indicated.

model in all of the physiological literature [32]. Most single cell models are variants of the Hodgkin-Huxley model and begin with a current balance equation:

$$C_m \frac{dv}{dt} = -\sum_x I_x, \tag{1.1}$$

where v is the membrane potential, C_m is the total cell capacitance, and I_x is the membrane ionic current through channels of type x. Often, the currents are in the form of voltage gated Nernst currents:

$$I_x = \bar{g}_x n_x^p (v - v_x) = g_x (v - v_x), \tag{1.2}$$

where

$$\frac{dn_x}{dt} = \frac{n_\infty^x(v) - n_x}{\tau_x(v)}. \tag{1.3}$$

In (1.2), $\bar{g}_x$ is the maximal conductance of the channel, n_x^p is the fraction of open channels, v_x is the Nernst potential and g_x is the time dependent channel conductance for channel x. Some models have Goldman-Hodgkin-Katz currents which are different, and are not addressed here. In some models $p > 1$ (such as the Hodgkin-Huxley model) but it is often the case that $p = 1$.

Because of the variable magnitudes of the gating time constants $\tau_x(v)$, many such models result in a system of ordinary differential equations of the form:

$$C_m \frac{dv}{dt} = -\sum_X I_X(v, w, z) \ , \tag{1.4}$$

$$\frac{dw}{dt} = \frac{w_\infty(v, z) - w}{\tau(v, z)} \ , \tag{1.5}$$

$$\frac{dz_i}{dt} = \varepsilon \frac{(z_{i\infty}(v) - z_i)}{\tau_i}, \quad i = 1, 2... \ , \tag{1.6}$$

where w is a channel activation variable, τ is a time constant, ε is a small parameter (relative to the other dimensional time constants), and the variables z_i in this model are either activation/inactivation variables associated with the voltage gating or concentrations of slowly varying regulatory chemicals (such as calcium).

History and Motivation

A goal of mathematical modeling of biological systems is to reproduce as many of the qualitative dynamics of individual cells and/or groups of particular types of cells as compared with experimental observations. We do not necessarily expect mathematical models to give exact quantitative results. Many mathematical models may be categorized as *biophysical* or *phenomenological*. Biophysical models attempt to incorporate as many known cellular facts and data as deemed relevant, whereas, phenomenological models attempt to reflect qualitative features of the experimental observations, but in as simple a model as possible. The Hodgkin-Huxley model is an example of a biophysical model and the equally well known FitzHugh-Nagumo [20] model is a phenomenological model which extracts the essential behavior of the Hodgkin-Huxley model in a vastly simplified form. We do not argue the superiority of one type of model over the other, but rather acknowledge that both types have their particular strengths, and feel that the best mechanism for advancing the body

of knowledge is a combination of both types.

If we were constructing a biophysical model, we would identify the underlying cellular mechanisms that produce bursting in our model (slow voltage- or calcium-dependent processes, cellular coupling, or other mechanisms). Since biophysical models are not amenable to mathematical analysis this necessitates the construction of phenomenological models to aid in analyses. The nonlinearities essential in biophysical models exhibiting bursting are part of what make any form of analysis difficult. Phenomenological models have allowed the use of averaging, Melnikov's method [41], [44], bifurcation theory and other tools which have allowed for characterizations of model parameter spaces.

From a modeling (mathematical) perspective, bursting depends on processes with distinctly different time scales, typically termed fast and slow (Rinzel [47]). The fast processes remain in quasi-steady state except for the jumps between states, while the slow processes modulate the fast dynamics between the silent and active states. Models of bursting all involve multiple time scales and can be written as a system of the form:

$$\begin{aligned} \frac{dx}{dt} &= f(x,y)\,, \quad x \in \mathbb{R}^M, \\ \frac{dy}{dt} &= \varepsilon g(x,y)\,, \quad y \in \mathbb{R}^K. \end{aligned}$$

Here the x equation, with y treated as a constant, is the fast subsystem.

The first formal classification scheme of bursting is due to Rinzel (1987) [48]. In this thesis we will look at a generalization of type Ia or 'square wave' bursting (see Figure 1A), according to Rinzel's classification. A more recent classification scheme by Izhikevich (2000) [29] refers to this type of bursting as a 'fold/homoclinic burster'. Issues surrounding the classification and types of bursting will be dealt with in Chapter 2.

The first biophysical mechanisms of bursting related to pancreatic β-cell electrical activity were developed by Atwater *et al* (1980) [2]. Chay and Keizer (1983) [13] used this work to create the first 'minimal' (biophysical) mathematical model, based on the Hodgkin-Huxley model. Since then there have been a large number of β-cell models [12], [23], [33], [53], [34], [11], [54] and other cellular models exhibiting bursting behavior.

In addition to studying bursting models in the context of pancreatic β-cells (or other endocrine cells), there has been great interest in modeling nerve cells [17], [22], [61], [60], [7], [35]. Nerve cells, or neurons, are specialized for rapid electrical signaling over long distances. Neurons, structurally consist of a soma, axons and dendrites. Whereas, axons and dendrites are unique to neurons, the soma resembles the cells in other organs. The basic mechanism of communication between neurons is the transmission of action potentials along axons. Many neurons exhibit bursting behavior. It has been speculated that bursting is a process that makes communication across synapses (between neurons) reliable [38], [31], [28], [60].

We have indicated that bursting requires both fast and slow processes. Many of the models we have mentioned use one slow variable as this slow process, but there are several models that utilize two slow variables. The Chay model (1988) [12] was a β-cell model which has led to the development of several other two slow variable models for β-cells, notably the models developed in: Smolen, Keizer (1992) [54]; Bertram, Previte, Sherman, Kinard, Satin [4]. Other models with more than one slow variable models include: Keizer, Smolen [34]; the CRAC β–cell model [5]; Plant, Kim [45].

We originally set out to model the spatial patterns observed in the visual cortex when presented different orientation stimuli. We realized early on in our work that individual cortical neurons had several qualitative features not obtainable us-

ing a simple phenomenological model of the type found in [42], [44], [15], [14], [10], [12], [53]. One such feature is an absence of a rapid transition from the active phase to the silent phase as is the case with square wave bursters (see Figure 1A). We decided to adapt the simple polynomial model of [42], [44] by adding one additional slow variable. Our original goal was to see if the addition of one slow variable would allow reasonable reproduction of cortical neuron experimental data. But the additional slow variable greatly complicated issues such as parameter selection, location of equilibria and even the existence of bursting solutions, and forced a revised set of goals. Considering the prevalence of models with more than one slow variable, and this issue of the dynamics of such cortical neurons, the goal of this thesis is to examine the mathematical structure of a phenomenological model of bursting with two slow variables.

Activation and Inactivation

Opening and closing of ionic channels, in response to changes in membrane potential, is the basis for electrical excitability. Thus, the generation and transmission of action potentials is via these ionic currents. There are several terms used to describe these changes in membrane potential and some of the controlling mechanisms, which shall now be defined. Depolarization is a reduction in magnitude of the membrane potential toward zero (algebraic increase), whereas, hyperpolarization refers to an increase in magnitude of the membrane potential; the potential becomes even more negative (tends to reduce excitability).

An electrophysiologist would say, in reference to ionic channels with low probability of opening, that when the channels are *activated*, the probability of openings increase. *Inactivation* is when channels that usually respond to membrane depolarization, enter a state such that activation no longer occurs. For our needs in this

work, we present a caricature of an activation variable in Figure 2. Briefly, if the cell depolarizes, then $z_\infty(v)$ in (1.6) is larger so z will tend to a larger value, thus driving the total current to a larger value in (1.4). Activation (also referred to as positive feedback) results in the opening of more ion channels, an increased current and triggers the growth of an action potential. As one might expect, inactivation is essentially the opposite and triggers closing of channels and is sometimes referred to as negative feedback or inhibition. The key point to remember is that cell depolarization (increase in voltage v) increases current if the channel is of activation type ($z'_\infty(v) > 0$) but decreases if the channel is of inactivation type ($z'_\infty(v) < 0$).

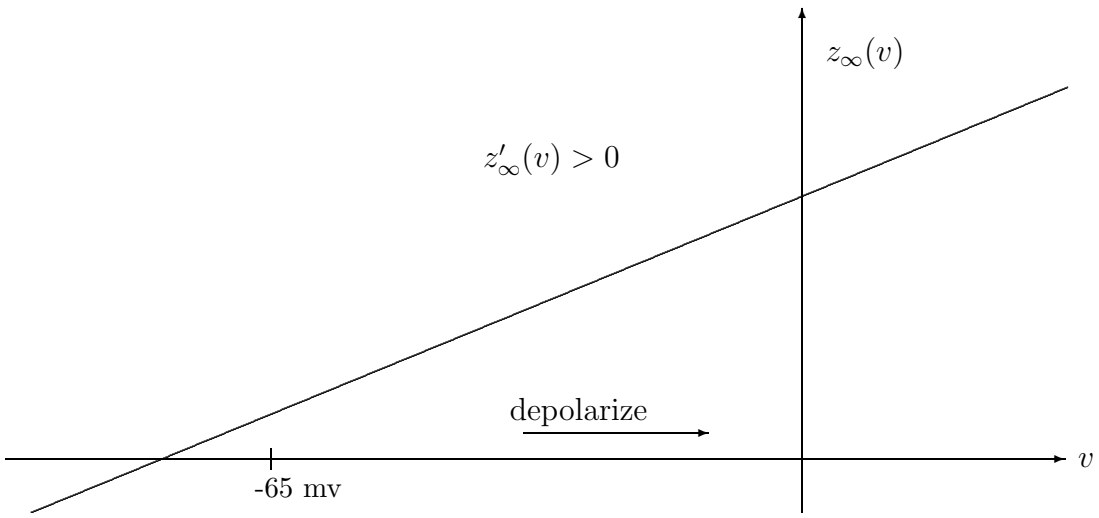


Figure 2: Representation of an activation variable. When the cell depolarizes, more channels open resulting in an increase of current.

Analysis, Background and Overview

The idea of using maps as a means to do analysis on bursting models is not a new

idea. Terman [58] used a map in his landmark 1991 paper to prove the existence of chaotic dynamics in a simple bursting model. This was an example where a fixed point of the full system was close to a homoclinic orbit of the fast subsystem, which allowed him to prove the existence of a hyperbolic structure similar to a Smale horseshoe. In a more recent paper, Butera [8] presents a simple two slow variable model then goes on to construct a map in order to organize the parameter space and aid in his analysis.

As indicated above, there is prior work defining and analyzing models with two slow variables. One such work is the Smolen, Terman, Rinzel (1993) [56] paper in which they analyze the model developed in [54]. In their paper they analyze a Hodgkin-Huxley type of model with two slow inactivation variables (inhibitory). In a more recent work by Bertram *et al* [4], they too looked at a model with two slow inactivation variables. But in their model the slow variables operate on vastly different time scales. In this thesis we will examine a phenomenological model with both activation and inactivation variables. Furthermore, to aid in the analysis we will work with dimensionless variables.

In the construction and analysis of the two slow variable models mentioned above, there have been no attempts at explicit construction of maps, nor any examination of the bifurcation of equilibria in the slow subsystem and the resulting dynamics. The only organization of the parameter space was for the purpose of identifying limit cycles. There have been no examples showing bistability between bursting solutions and stable equilibria. The existence of bistability of this type could offer an alternative explanation for why some cells burst and others do not, other than the current explanation involving heterogeneity between cells [43], [55] . The bistability explanation is that some cells are locked in bursting mode while others are trapped near a stable equilibrium. All of these issues are addressed in this thesis.

Organization of thesis

In Chapter 2 we make all the definitions necessary to describe our model, the subsystems and parameters. We begin by extending the one slow variable Pernarowski model [42] to our two slow variable model defined in (2.8)-(2.11). We go on to define the fast and slow subsystems and describe the dynamics of each. Then in preparation of our map definition, we rigorously derive the averaged fast subsystem using multiple scales averaging. This averaged fast subsystem is used to describe approximate solutions in the active phase and the subsequent leading order slow flow in the fast subsystem. With the distinction between fast and slow parameters made, the possible variations in model parameters will be considered.

Since we are interested in bursting solutions, the location, stability and number of equilibria are of necessary importance to us. We have an entire section devoted to addressing equilibria questions and Hopf bifurcation issues in terms on our slow subsystem parameters.

With the aforementioned model definitions and derivations we are adequately prepared, in Chapter 3, to carefully define the return map. We begin with an overview of what we expect the map to describe and the manner in which we accomplish this goal. Our map is constructed as the composition of two composite maps, one for the active phase, $\widehat{\phi}$, and one for the silent phase, $\widetilde{\phi}$. Then we define a composite map in terms of our two slow variables and, finally using the functional dependence of the slow variables on certain transition curves, we present a reduction of the two dimensional map to a one dimension map. Singular approximations to bursting solutions are then described as fixed points $\bar{x}$ of the composite map which we define by $\bar{x} = \widetilde{\phi}(\widehat{\phi}(\bar{x}))$.

With our theoretic map defined we proceed to a special case of our two slow model. This special case (when our two slow time constants are equal) is shown to

reduce our model to a one slow variable model, which serves as a convenient starting point for our analysis, including the important role of verifying that our theoretical map has non-trivial domain.

In Chapter 4 we use several numerical methods to construct the map defined in Chapter 3. Our first goal is to numerically approximate the composite maps. We present results obtained using Matlab to numerically integrate our model and the averaged fast subsystem of Chapter 2 to approximate the map functions, and then go on to indicate why this method is not that well suited for our goals. Next, we carefully explain how we use AUTO [18] to homotope from a boundary value problem (BVP) with a known solution to the solution to our system, also stated as a BVP. We then numerically generate the two maps $\widetilde{\phi}$ and $\widehat{\phi}$ from these BVPs using AUTO. The final section in the chapter evaluates the various numerical methods utilized and we show that the singular solutions characterized by our return map match well those obtained by our full model. The aforementioned Matlab simulations corroborate the results obtained using AUTO, and then xppaut [19] is used to further verify and help illustrate the results.

In Chapter 5 we further delve into some of the issues involved in the construction of the map ϕ and some of the complications associated with its domain and range. Then we discuss some of the interesting dynamics of solutions of our model. We carefully examine the bistability scenario, in which bursting solutions coexist with a stable fixed point on the slow manifold. While examining these qualitatively interesting examples we illustrate how our map and the other tools we generated are helpful in locating these examples.

CHAPTER 2

MODEL DEFINITIONS AND DEVELOPMENT

There have been many models exhibiting bursting, consisting of three variables (one of which is a slow process). The Pernarowski polynomial model (1994) [42] is such a one slow variable phenomenological model that has been further studied by others [14], [3] and will be the starting point for our model in this thesis. Other such one slow variable models exhibiting bursting include the Hindmarsh and Rose (1984) [24] and a modified Morris-Lecar model (1981) [39]. Bursting in pancreatic β-cells has been widely studied, and many one slow variable models have been developed, a few of which we mention here. Chay simplified the Chay-Keizer (1983) model [13] to a one slow variable model of pancreatic β-cells (1985) [9]. The Sherman-Rinzel-Keizer (SRK) [53] is another β-cell model that has been investigated by others [41]; as was the Sherman-Rinzel (1991) model [52] by Sherman (1994) [50] and de Vries-Sherman-Zhu (1998) [16]. Sherman (1997) used a minimal model to discuss general β-cell models [51]. Terman (1991) used a general model to prove a variety of results for a class of models exhibiting bursting solutions [58].

The aforementioned Pernarowski polynomial model is:

$$\frac{du}{dt} = f(u) - w - z \ , \tag{2.1}$$

$$\frac{dw}{dt} = \frac{1}{\tau}(g(u) - w) \ , \tag{2.2}$$

$$\frac{dz}{dt} = \varepsilon(h(u) - z) \ , \tag{2.3}$$

where $0 < \varepsilon \ll 1$ is a parameter, f and g are cubic polynomials, and

$$h(u) = \beta(u - \alpha), \tag{2.4}$$

where α, β are parameters. By comparing Eqn (1.4) with (2.1) we see that the variable z in (2.1)-(2.3) is analogous to the conductance seen in the current balance

equation. This model will be a starting point for our construction of a two-slow variable model involving two slowly varying conductances.

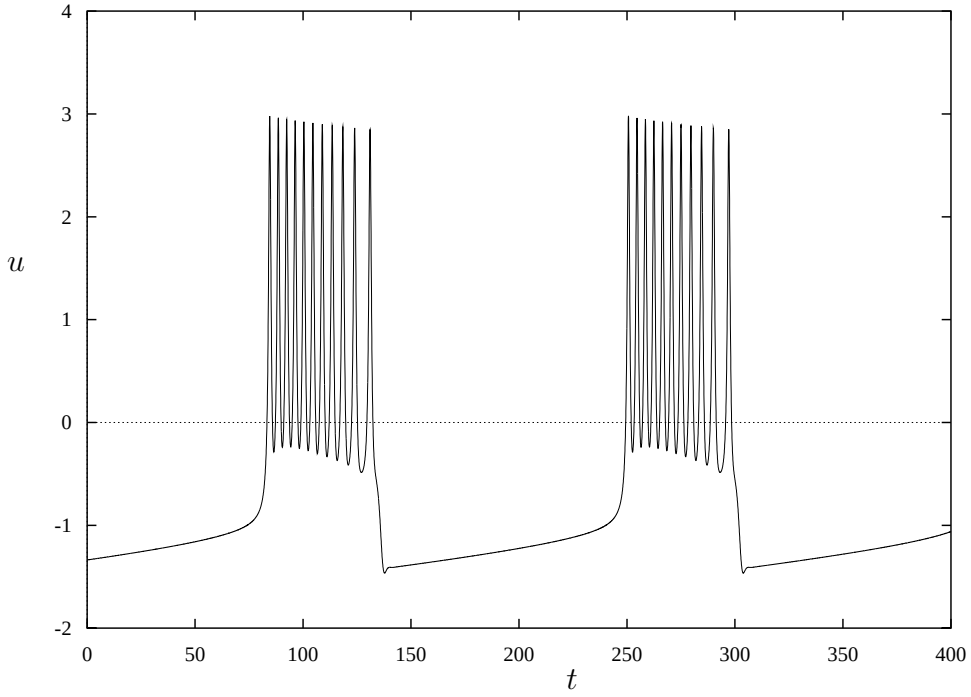


Figure 3: Square wave bursting - solution of (2.1)-(2.3).

A range of parameters, for which (2.1)-(2.3) yields square wave bursts such as those in Figure 3, will be discussed in a subsequent section.

Model definition

Here we define a two slow variable model similar to (2.1)-(2.3), motivated by analogy with more biophysical models involving complex current balance equations like (1.4). Let us suppose there exist two slow currents of the same ion in (1.4) of the form (1.2),

$$I_x = \bar{g}_x n_x^p (v - v_x) = g_x (v - v_x).$$

Then we may rewrite the current balance equation as the sum of the fast currents I_f and the two slow currents mentioned above:

$$C_m \frac{dv}{dt} = -\sum_f I_f - \bar{g}_x x(v - v_x) - \bar{g}_y y(v - v_x).$$

Then, for $v > v_x$,

$$\frac{C_m}{v - v_x}\frac{dv}{dt} = -\sum_f I_f^* - \bar{g}_x x - \bar{g}_y y. \tag{2.5}$$

Now define u via:

$$du = \frac{dv}{v - v_x}, \tag{2.6}$$

thus

$$u = \ln(v - v_x). \tag{2.7}$$

If the membrane potential v, time and our channel conductances are nondimensionalized then we may write (2.5):

$$\frac{du}{d\tau} = -\sum_f I_f^* - x - \gamma y.$$

where γ is some dimensionless parameter,

$$\frac{dx}{d\tau} = \frac{x_\infty(u) - x}{\tau_x(u)},$$

and $\frac{dy}{d\tau}$ has the same form. With an appropriate choice in scaling, the physiological intuition associated with the membrane potential v is retained in our variable u. If in addition, $\tau_x(u)$ and $\tau_y(u)$ are relatively constant over a range of voltages u then a reasonable form for a model with two slow variables would be:

$$\frac{du}{dt} = f(u) - w - x - \gamma y\ , \tag{2.8}$$

$$\frac{dw}{dt} = \frac{g(u) - w}{\tau_w}\ , \tag{2.9}$$

$$\frac{dx}{dt} = \varepsilon\frac{h_1(u) - x}{\tau_1}\ , \tag{2.10}$$

$$\frac{dy}{dt} = \varepsilon\frac{h_2(u) - y}{\tau_2}\ . \tag{2.11}$$

Notice that the model (2.1)-(2.3) is extended in a simple fashion to our two-slow variable model (2.8)-(2.11), hereafter referred to as (FULL). In this model τ_w, τ_1, τ_2 and γ are constants, and

$$f(u) = -\frac{a}{3}u^3 + a\mu u^2 + (1 - a(\mu^2 - \eta^2))u, \tag{2.12}$$

$$g(u) = (1 - \frac{a}{3})u^3 + a\mu u^2 - (2 + a(\mu^2 - \eta^2))u - 3, \tag{2.13}$$

are the same functions used in (2.1)-(2.3), and (a, μ, η) are parameters. Finally,

$$h_i(u) = \beta_i(u - \alpha_i), \quad i = 1, 2, \tag{2.14}$$

where α_i and β_i are also constants. In this model u should be interpreted as the membrane potential, whereas w is a fast conductance and x, y are slow conductances for gating channels of the same ion.

It is worth pointing out the similarity between (2.1)-(2.3) and (FULL). This similarity will be utilized in several key places in this work, and will allow us to build on the great deal of already completed analysis and utilize the simplicity of the fast subsystem of the Pernarowski model. The complicated form of the polynomials f and g, which appear in both models, is due in part to their derivation from a Liénard form in Pernarowski [42], [43]. An advantage of the Liénard form is the availability of Melnikov theory to analytically approximate homoclinic bifurcation points [44], [42]. We mention these facts here for reference purposes only, but will not need them in subsequent analysis.

In (2.9) there appears a time constant τ_w. It's appearance in this model is primarily for modeling purposes since its inclusion makes (FULL) resemble biophysical models (i.e., CRAC [5]) more closely. As far as the model is concerned, τ_w affects the stability but not the location of equilibria of the fast subsystem of (FULL). It's value will also effect the averaged fast subsystem (defined later in this chapter)

dynamics, but has no effect at all on the slow subsystem of (FULL). With that said, we will set $\tau_w = 1$ and will not mention it again, but recognize that much of what is to follow could be generalized to include the effect of this parameter.

Subsystem derivation/definitions

In (FULL), x and y are slow variables whereas u and w are fast variables. We will use this fact in Chapter 3 to recast the construction of bursting solutions of this system as a singular perturbation problem. In order to get an understanding of the complex dependence of the dynamics of this system on the various parameters we will show that singular bursting solutions correspond to fixed points of a one-dimensional return map. With this goal in mind we first define the fast, slow and averaged fast subsystems of (FULL).

Fast subsystem dynamics

On the fast t time scale the dynamics of (FULL) is governed by the Fast Subsystem (FS) obtained by letting $\varepsilon = 0$,

$$\frac{du}{dt} = f(u) - w - z \quad , \quad z \equiv x + \gamma y \, , \tag{2.15}$$

$$\frac{dw}{dt} = g(u) - w \, , \tag{2.16}$$

with the slow variables x and y treated as parameters and combined as shown above. Note that the (FS) of (FULL) is the same as the (FS) of (2.1)-(2.3). We introduced the bifurcation parameter $z = x + \gamma y$ to generate the (FS) bifurcation diagram in Figure 4. The u-values of equilibria states are plotted against z. The projection of the equilibria of (FS) onto the (u, z)-plane yields a Z-shaped curve

$$z = G(u) \equiv f(u) - g(u), \tag{2.17}$$

where, given the definitions of f and g,

$$G(u) = -u^3 + 3u + 3. \tag{2.18}$$

Note here that despite the dependence of f and g on the parameters (a, μ, η), G

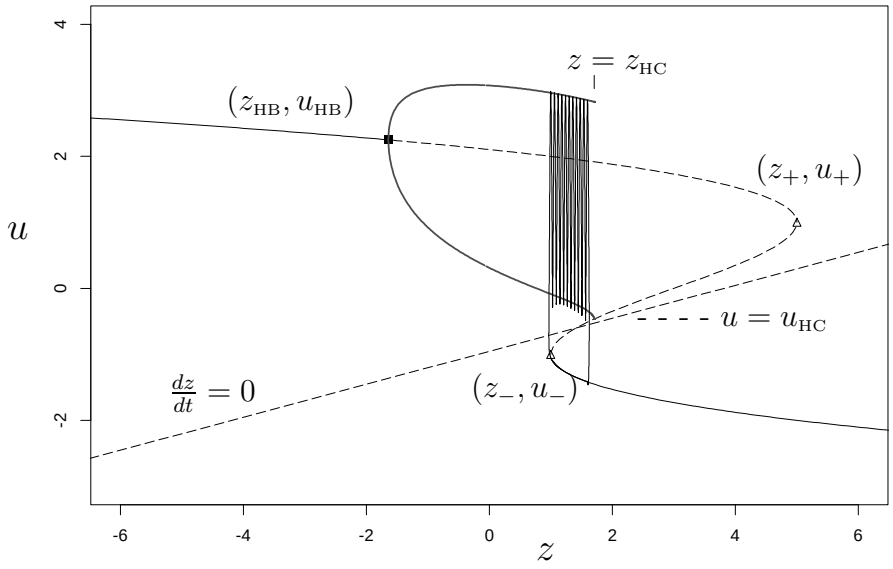


Figure 4: Fast subsystem bifurcation diagram for (2.15)-(2.16) when $(a, \eta, \mu) = \left(\frac{1}{4}, \frac{3}{4}, \frac{3}{2}\right)$ with a bursting solution of (2.1)-(2.3) superimposed.

depends on no parameters. Solid lines on the Z curve indicate stable equilibria, whereas the dashed portion indicates unstable equilibria. Equilibria on the lower branch are stable nodes, steady states on the middle branch are saddle points (as shown in the next section). The stability of the steady states on the upper branch changes at a supercritical Hopf bifurcation at $z = z_{\mathrm{HB}}$. Though Figure 4 is computed numerically using xppaut [19], the aforementioned stabilities and bifurcations were proven analytically in [42]. Stable periodic orbits, the dark thick lines, emanate from the Hopf point and terminate at a homoclinic bifurcation on the middle branch at $z = z_{\mathrm{HC}}$. The upper and lower portions indicate the extreme values of u during the

oscillation. With limit points (saddle node bifurcations), as indicated, at $z = z_-$ and $z = z_+$, the (FS) has a region of bistability where stable lower branch equilibria and stable periodic orbits coexist for $z \in (z_-, z_{\rm HC})$. In later sections we will make reference to the values $u_+, u_-, u_{\rm HC}$ as the u value at which the upper limit point, the lower limit point and the homoclinic bifurcation occur, respectively. As indicated on Figure 4, when we refer to $u_{\rm HC}$ we mean the u value on the middle branch when $z = z_{\rm HC}$.

Also shown in Figure 4 is the z (slow) nullcline of (2.1)-(2.3), as the dashed line passing through the middle branch of the Z curve. Given the definition of $h(u)$ in (2.4), if $\beta > 0$ then $\dot{z} < 0$ below the nullcline and $\dot{z} > 0$ above the nullcline, so that z decreases for trajectories below the nullcline and increases when above the nullcline on the slow time scale $\tilde{t} = \varepsilon t$. As shown, z is a slow activation variable, because as u increases (membrane depolarizes), $h(u)$ increases so z follows (2.3), as we illustrated in Figure 2. We observe, the statement that z is an activation variable is equivalent to $h'(u) > 0$ which in turn is equivalent to $\beta > 0$.

At this point in the thesis we are just trying to describe the overall dynamics of the system, hence a bursting solution of the one slow variable model, (2.1)-(2.3), is superimposed on this bifurcation diagram. Our use of the one slow variable model rather that (FULL) is for simplicity. We also wish to emphasize that the (FS) of both models are the same. Later on in the thesis we will explore the more complicated dynamics of (FULL). In what is often referred to as the "silent phase" of (2.1)-(2.3), trajectories lie close to the lower branch of equilibria. As indicated above, the trajectory moves to the left until bistability is lost at the limit point (z_-, u_-). As z decreases below z_-, trajectories are then attracted to the only stable object, the (FS) limit cycle manifold, initiating the "active phase" marked by bursting oscillations. Above the z nullcline, movement on the limit cycle manifold is to the right and

continues until bistability is lost at $z = z_{\text{HC}}$. This bistability is lost when the (FS) limit cycles coalesce with the middle branch equilibria at a homoclinic bifurcation, whence trajectories are attracted to the lower branch, initiating the silent phase again.

In the classification scheme of Rinzel [48] this is described as type I bursting. Further discussion of the phenomenological and topological aspects of these bursters is nicely organized in Bertram *et al.* [3]. A more recent classification scheme by Izhikevich (2000) [29] refers to this type of burst as a 'fold/homoclinic burster'. The Izhikevich classification scheme is meant to be more descriptive, in that the name refers to the type of bifurcations involved. Our fold/homoclinic burster, as described above and illustrated in Figure 4, gets its name due to the silent phase ends via a *fold* bifurcation and the active phase terminates via a saddle *homoclinic* orbit bifurcation.

In (FULL), we note that the case in which both x and y are inactivation variables and $\tau_1 = \tau_2$ is not interesting. In order better explain why this is true, we again revert to the one slow variable model (2.1)-(2.3), but emphasize that this explanation generalizes to (FULL) in the $\tau_1 = \tau_2$ case as shall be shown in Chapter 3. Using the definition of $h(u)$ in (2.4) we see that the z nullcline is plotted as $u = \frac{1}{\beta}z + \alpha$. Recalling, z being an inactivation variable is equivalent to the condition $\beta < 0$, the z nullcline shown in Figure 5 has negative slope. Since $\dot{z} > 0$ below the nullcline and $\dot{z} < 0$ above the nullcline, z decreases for trajectories below the nullcline and increases when above the nullcline on the slow time scale $\tau = \varepsilon t$. This means that trajectories below the nullcline will continue to move to the right, near the lower branch of equilibria, until the z nullcline intersects the lower branch, at which point there will be a stable equilibrium. Above the nullcline, movement on the limit cycle manifold is to the left and continues until the termination of the limit cycles at the

Hopf bifurcation $z = z_{\text{HB}}$, at which point trajectories continue moving to the left near the stable upper branch of equilibria, stopping only if the z nullcline intersects the upper branch, in which instance there will be another stable equilibrium. Hence, our description of the inactivation case as not interesting is because it cannot yield bursting solutions. This result, though explained in terms of the one slow variable model, holds for our two slow variable model in the $\tau_1 = \tau_2$ case. Again, details of the two slow variable case where both x and y are inactivation variables will be postponed. However, we point out the similarities between the functions $h_i(u)$ in (2.14) of (FULL) and $h(u)$ in (2.4) of the one slow variable model, such as the condition for a slow variable (x, y) to be an activation variable is that the parameter $\beta_i > 0$. Similarly, (x, y) is an inactivation variable whenever $\beta_i < 0$.

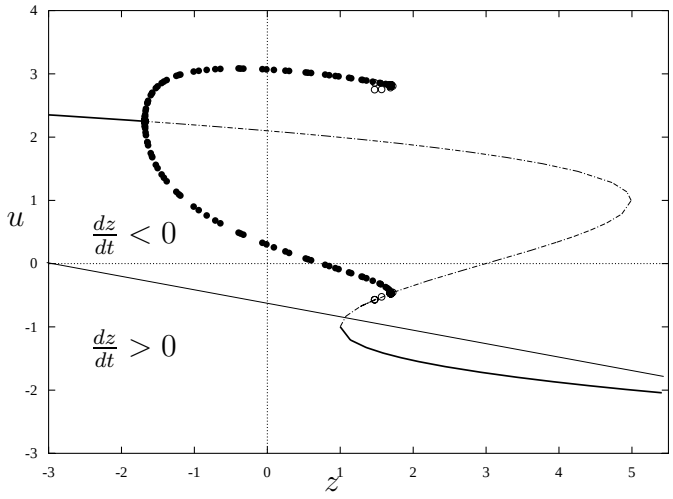


Figure 5: Bifurcation diagram for (2.15)-(2.16) when $(a, \eta, \mu) = \left(\frac{1}{4}, \frac{3}{4}, \frac{3}{2}\right)$. Superimposed on the figure is the z nullcline in the case when z is an inactivation variable.

Recall that the lower branch equilibria of (FS) forms a stable manifold for the

fast dynamics, this is a two dimensional manifold in $\mathbb{R}^4$ defined as follows:

$$\mathcal{S}_L = \{(u, w, x, y) : x + \gamma y = G(u), w = g(u), u < u_-\}, \tag{2.19}$$

where u_- is the value of u at the limit point, as indicated in Figure 4. If $P : \mathbb{R}^4 \rightarrow \mathbb{R}^4$ is the projection operator:

$$P = \begin{pmatrix} u \\ w \\ x \\ y \end{pmatrix} = \begin{pmatrix} 0 \\ 0 \\ x \\ y \end{pmatrix},$$

then we define the projection onto the (x, y)-plane, $P(\mathcal{S}_L) = S_L$:

$$S_L = \{(u, w, x, y) : x + \gamma y = G(u), u < u_-, u = 0, w = 0\}.$$

For ease of notation from now on we will drop the conditions $u = 0$ and $w = 0$ and simply write

$$S_L = \{(x, y) : x + \gamma y = G(u), u < u_-\}. \tag{2.20}$$

The reason we distinguish S_L from $\mathcal{S}_L$ is that it will become easier later to visualize trajectories on S_L than on $\mathcal{S}_L$. We note, for instance, that equilibria of (FULL) truly only exist on $\mathcal{S}_L$.

In an analogous fashion we define the upper and lower (FS) manifolds, respectively, as:

$$\begin{aligned} \mathcal{S}_U &= \{(u, w, x, y) : x + \gamma y = G(u), w = g(u), u > u_+\}, \\ \mathcal{S}_M &= \{(u, w, x, y) : x + \gamma y = G(u), w = g(u), u \in (u_-, u_+)\}, \end{aligned}$$

with projections onto the (x, y)-plane, $P(\mathcal{S}_j) = S_j$ for $j = U, M, L$:

$$S_U = \{(x, y) : x + \gamma y = G(u), u > u_+\}, \tag{2.21}$$

$$S_M = \{(x, y) : x + \gamma y = G(u), u \in (u_-, u_+)\}. \tag{2.22}$$

For ease of reading, and to retain consistency with the one-slow variable model, we will continue to use the references upper branch, middle branch and lower branch for the two dimensional manifolds $(\mathcal{S}_U, \mathcal{S}_M, \mathcal{S}_L)$, respectively.

Slow subsystem dynamics

We start with (2.8)-(2.11) in our derivation of the Slow Subsystem (SS) which is used to describe the slow flow on $\mathcal{S}_L$. Letting $\tilde{t} = \varepsilon t$ be the slow time then

$$\varepsilon \frac{du}{d\tilde{t}} = f(u) - w - x - \gamma y \ , \tag{2.23}$$

$$\varepsilon \frac{dw}{d\tilde{t}} = g(u) - w \ , \tag{2.24}$$

$$\frac{dx}{d\tilde{t}} = \frac{h_1(u) - x}{\tau_1} \ , \tag{2.25}$$

$$\frac{dy}{d\tilde{t}} = \frac{h_2(u) - y}{\tau_2} \ . \tag{2.26}$$

Setting $\varepsilon = 0$ we get, to leading order,

$$x + \gamma y = f(u) - g(u) \equiv G(u) \ , \tag{2.27}$$

$$w = g(u) \ , \tag{2.28}$$

$$\frac{dx}{d\tilde{t}} = \frac{h_1(u) - x}{\tau_1} \ , \tag{2.29}$$

$$\frac{dy}{d\tilde{t}} = \frac{h_2(u) - y}{\tau_2} \ . \tag{2.30}$$

For $u < u_-$, equations (2.27)-(2.30) define the (SS) of (FULL). Solutions of (2.27)-(2.30) yield trajectories on $\mathcal{S}_L$ which are leading order approximations to the silent phase of (FULL).

Equation (2.27) gives us the algebraic condition requiring flow to remain on the slow manifold. Recalling our definitions $z = x + \gamma y$ and (2.18), $G(u) = -u^3 + 3u + 3$, we are able to rewrite (2.27) as the cubic

$$u^3 - 3u - 3 + z = 0. \tag{2.31}$$

We note again that the u in (2.29)-(2.30) are restricted to $\mathcal{S}_L$ (lower branch) or equivalently that $u < u_-$. These u values may be computed explicitly as a function of z by solving (2.31) for u and picking the root having $u < u_-$. For implementation purposes in programing code, the selection of the root on the lower branch is easily accomplished using the trigonometric form of the cubic root formula. A cubic in the form:

$$x^3 + c_1 x + c_0 = 0,$$

with $c_1 c_0 \neq 0$, can always be solved by transforming it to the trigonometric identity:

$$4\cos^3\theta - 3\cos\theta - \cos(3\theta) \equiv 0,$$

by letting $x = m\cos\theta$ [6], providing

$$\begin{aligned} m &= 2\sqrt{\frac{-c_1}{3}}, \\ cos(3\theta) &= \frac{3c_0}{c_1 m}. \end{aligned} \tag{2.32}$$

If θ_1 is any solution of (2.32), then the following are solutions as well

$$\theta_1 + \frac{2\pi}{3}, \theta_1 + \frac{4\pi}{3},$$

where θ_1 has the form:

$$\theta_1 = \frac{1}{3}\arccos\left(\frac{3c_0}{c_1 m}\right).$$

As such, the roots of the cubic $x^3 + c_1 x + c_0 = 0$ are

$$m\cos\left(\theta_1 + \frac{k\pi}{3}\right),\ k = 0, 2, 4.$$

In this development, the $k = 2$ case was the lower branch root, then u_{LB}, of (2.31) for $1 \leq z \leq 5$ is

$$u_{\text{LB}}(z) = 2\cos\left(\frac{1}{3}\arccos\left(\frac{3-z}{2}\right) + \frac{2\pi}{3}\right). \tag{2.33}$$

For $z > 5$, u_{LB} is given by

$$u_{\text{LB}}(z) = -2\cosh\left(\frac{1}{3}\ln\left(\frac{z-3}{2} + \sqrt{\left(\frac{z-3}{2}\right)^2 - 1}\right)\right). \tag{2.34}$$

This allowed us to rewrite (2.29)-(2.30) as,

$$\frac{dx}{d\tilde{t}} = F_1(x,y) \equiv \frac{\beta_1(u_{\text{LB}}(z) - \alpha_1) - x}{\tau_1}, \tag{2.35}$$

$$\frac{dy}{d\tilde{t}} = F_2(x,y) \equiv \frac{\beta_2(u_{\text{LB}}(z) - \alpha_2) - y}{\tau_2}. \tag{2.36}$$

Solutions of (2.35)-(2.36) are the projections of leading order approximations of (FULL) onto the (x, y)-plane when initial conditions are close to $\mathcal{S}_L$.

When discussing the dynamics of (FULL) we have mentioned a quick transition to the slow manifold, when $z \geq z_{\text{HC}}$. After such a transition the flow remains on the slow manifold $\mathcal{S}_L$, to leading order, until u increases above u_-. It will become important to us to understand the behavior of this slow flow. For example, one might need to know the stability and existence of equilibria of (FULL) when they occur on $\mathcal{S}_L$. Additionally, provided there are no such equilibria on the slow manifold, is the flow 'compressive'? If we could somehow show that the flow converged toward an invariant subspace, this would help us in determining if there exist bursting solutions. We will address this particular issue in Chapter 3.

Averaged Fast subsystem

In this section we derive the Averaged Fast subsystem (AFS) needed to define the return map in Chapter 3. In the previous section we described approximations to the silent phase. However, in the active phase of the bursting solution it is harder to approximate. One method used to approximate such solutions is the method of averaging [59], [49], [36], [26]. Here multiple scales averaging will be applied.

The precise definition, expansions and assumptions are carefully delineated in this section.

First consider the set

$$S_A = \{(x, y) : z_{HB} < x + \gamma y < z_{\text{HC}}\},$$

and note that (see Figure 4) for every $(x, y) \in S_A$ the (FS) has a stable T-periodic limit cycle $(u, w) = (\Omega_1(t, z), \Omega_2(t, z))$ where the period T is a function of $z = x+\gamma y$ alone. The slow flow in the (AFS) is defined so long as $(x(\tilde{t}), y(\tilde{t})) \in S_A$. In the singular limit, when $z = z_{\text{HC}}$, bistability of (FS) is again lost and a transition to the silent phase must occur. We will use the (AFS) to describe the slow flow in the active region S_A.

The method of multiple scales averaging will be applied to the system

$$\frac{d\mathbf{u}}{dt} = F(\mathbf{u}, \mathbf{z}), \tag{2.37}$$

$$\frac{d\mathbf{z}}{dt} = \varepsilon G(\mathbf{u}, \mathbf{z}), \tag{2.38}$$

where $\mathbf{u} \in \mathbb{R}^2$ and $\mathbf{z} \in \mathbb{R}^2$. In the active phase, we assume that we have a family of limit cycles $\Omega = \Omega(t, \mathbf{z})$ that are $T(\mathbf{z})$-periodic in t and satisfy

$$\frac{d\Omega}{dt} = F(\Omega, \mathbf{z}), \quad \forall \mathbf{z} \in S_A. \tag{2.39}$$

We seek an asymptotic approximation of (2.37)-(2.38) valid to $O(\varepsilon)$ for $t = O(\frac{1}{\varepsilon})$.

Toward that end, we assume an expansion of the form

$$\mathbf{u}(t) = U(\tau, \tilde{t}, \varepsilon) = U_0(\tau, \tilde{t}) + \varepsilon U_1(\tau, \tilde{t}) + O(\varepsilon^2), \tag{2.40}$$

$$\mathbf{z}(t) = Z(\tau, \tilde{t}, \varepsilon) = Z_0(\tau, \tilde{t}) + \varepsilon Z_1(\tau, \tilde{t}) + O(\varepsilon^2), \tag{2.41}$$

where $\tilde{t}$ is a slow time:

$$\tilde{t} = \varepsilon t, \tag{2.42}$$

and the strained (fast) time τ is defined by

$$\frac{d\tau}{dt} = \omega(\tilde{t}), \tag{2.43}$$

for a function ω as yet to be determined.

As with other multiple scales methods, it is possible to choose an appropriate ω so that U_0 is 1-periodic in τ. In addition to the aforementioned periodicity we want our leading order approximation $U_0(\tau, \tilde{t})$ close to $u(t)$ for times $\tilde{t} = O(1)$. With U_0 and Z_0 suitably determined, we also require $U_i(\tau, \tilde{t})$ and $Z_i(\tau, \tilde{t})$ to be 1-periodic in τ for $i = 0, 1, 2, \ldots$. The periodicity of the U_i and Z_i in τ assures the functions U, Z are bounded in τ, so that $|U - U_0| = O(\varepsilon)$ for $\tilde{t} = O(1)$, for instance.

Using these definitions, the time derivatives of $U(\tau, \tilde{t}, \varepsilon)$ are

$$\frac{dU}{dt} = \omega\frac{\partial U}{\partial \tau} + \varepsilon\frac{\partial U}{\partial \tilde{t}}\,, \tag{2.44}$$

$$\frac{d^2U}{dt^2} = \omega^2\frac{\partial^2 U}{\partial \tau^2} + 2\varepsilon\omega\frac{\partial^2 U}{\partial \tau \partial \tilde{t}} + \varepsilon\frac{\partial \omega}{\partial \tilde{t}}\frac{\partial U}{\partial \tau} + \varepsilon^2\frac{\partial^2 U}{\partial \tilde{t}^2}\,, \tag{2.45}$$

with similar expressions for $Z(\tau, \tilde{t}, \varepsilon)$. The expansions (2.44)-(2.45) are valid for any choice of ω.

Expanding $F(\mathbf{u}, \mathbf{z})$ about (U_0, Z_0) gives

$$F(\mathbf{u}, \mathbf{z}) = F(U_0, Z_0) + \varepsilon D_{\mathbf{u}} F(U_0, Z_0) U_1 + \varepsilon D_{\mathbf{z}} F(U_0, Z_0) Z_1 + O(\varepsilon^2)\,, \tag{2.46}$$

where for $\mathbf{u} = (u_1, u_2)^T$

$$D_{\mathbf{u}} F = \begin{bmatrix} \frac{\partial F_1}{\partial u_1} & \frac{\partial F_1}{\partial u_2} \\ \frac{\partial F_2}{\partial u_1} & \frac{\partial F_2}{\partial u_2} \end{bmatrix}, \tag{2.47}$$

and in a similar fashion $D_{\mathbf{z}} F$ is the Jacobian of F in $\mathbf{z}$.

Putting this all together, (2.37)-(2.38) become

$$\omega\frac{\partial U_0}{\partial \tau} + \varepsilon\left(\frac{\partial U_0}{\partial \tilde{t}} + \omega\frac{\partial U_1}{\partial \tau}\right) = F^{(0)} + \varepsilon\left(D_{\mathbf{u}} F^{(0)} U_1 + D_{\mathbf{z}} F^{(0)} Z_1\right) + O(\varepsilon^2)\,, \tag{2.48}$$

$$\omega\frac{\partial Z_0}{\partial \tau} + \varepsilon\left(\frac{\partial Z_0}{\partial \tilde{t}} + \omega\frac{\partial Z_1}{\partial \tau}\right) = \varepsilon G(U_0, Z_0) + O(\varepsilon^2)\,, \tag{2.49}$$

where the superscript$^{(0)}$ in (2.48) means evaluated at (U_0, Z_0). These equations can be written as a system of partial differential equations. The $O(1)$ terms from (2.48)-(2.49) are

$$\omega \frac{\partial U_0}{\partial \tau} = F(U_0, Z_0)\,, \tag{2.50}$$

$$\frac{\partial Z_0}{\partial \tau} = 0\,, \tag{2.51}$$

and the $O(\varepsilon)$ terms,

$$\frac{\partial U_0}{\partial \tilde{t}} + \omega \frac{\partial U_1}{\partial \tau} = D_{\mathbf{u}} F(U_0, Z_0) U_1 + D_{\mathbf{z}} F(U_0, Z_0) Z_1\,, \tag{2.52}$$

$$\frac{\partial Z_0}{\partial \tilde{t}} + \omega \frac{\partial Z_1}{\partial \tau} = G(U_0, Z_0)\,. \tag{2.53}$$

From (2.51) it is evident that Z_0 does not depend on τ. Henceforth, we write $Z_0 = Z_0(\tilde{t})$.

Now we choose ω so that U_0 is 1-periodic in τ and is a solution of (2.50). To begin this determination, recall our earlier assumption that Ω is $T(\mathbf{z})$-periodic in t. By way of example, if $\Omega(s, \mathbf{z})$ is $T(\mathbf{z})$-periodic in s then $\Omega(Ts, \mathbf{z})$ is 1-periodic in s. With this said, we choose

$$\omega(\tilde{t}) = \frac{1}{T(Z_0(\tilde{t}))}\,. \tag{2.54}$$

To see that this choice of ω now yields a U_0 which is 1-periodic in τ. We start with

$$U_0(\tau, \tilde{t}) = \Omega(\tau T(Z_0(\tilde{t})) + \psi(\tilde{t}), Z_0(\tilde{t}))\,, \tag{2.55}$$

where $\psi(\tilde{t})$ is a slowly varying phase. Now take the partial derivative of (2.55) in τ

$$\frac{\partial U_0}{\partial \tau} = T(Z_0) \frac{\partial \Omega}{\partial t}\,, \tag{2.56}$$

which can be rewritten as

$$\frac{1}{T(Z_0)} \frac{\partial U_0}{\partial \tau} = \frac{\partial \Omega}{\partial t} = F(U_0, Z_0)\,. \tag{2.57}$$

The right hand equality above comes from our assumption in (2.39). This shows that with our choice of ω in (2.54) and U_0 defined in (2.55) we now have a 1-periodic solution to (2.50) provided $Z_0(\tilde{t}) \in S_A$.

Several remarks are worth noting at this point. It is now clear that the straining of the fast time in (2.43) is required to ensure that U_0 is 1-periodic in τ. Although we have accounted for the slowly varying phase ψ in (2.55), we will show it is not needed to determine $Z_0(\tilde{t})$. This will become important in Chapter 3 since there only $Z_0(\tilde{t})$ is needed to determine the map ϕ used to construct singular approximations to bursting solutions.

We now turn our attention to the Z equation. The requirement that Z_1 be 1-periodic in τ helps us derive necessary conditions for Z_0. Integrating (2.53) over $\tau \in (0,1)$

$$\int_0^1 G(U_0(\tau,\tilde{t}),Z_0(\tilde{t}))d\tau = \int_0^1 \left(\frac{\partial Z_0}{\partial \tilde{t}} + \omega(\tilde{t})\frac{\partial Z_1}{\partial \tau}(\tau,\tilde{t})\right) d\tau \tag{2.58}$$

$$= \frac{\partial Z_0}{\partial \tilde{t}} + \omega(\tilde{t})[Z_1(1,\tilde{t}) - Z_1(0,\tilde{t})]\,. \tag{2.59}$$

Thus, choosing Z_0 as a solution to

$$\frac{\partial Z_0}{\partial \tilde{t}} = \int_0^1 G(U_0(\tau,\tilde{t}),Z_0(\tilde{t}))d\tau, \tag{2.60}$$

implies $Z_1(1,\tilde{t}) = Z_1(0,\tilde{t})\ \ \forall \tilde{t}$ in (2.59). If we incorporate (2.55), the slow evolution equation (2.60) becomes

$$\frac{\partial Z_0}{\partial \tilde{t}} = \int_0^1 G\left(\Omega(\tau T(Z_0)+\psi(\tilde{t})),Z_0\right) d\tau. \tag{2.61}$$

We will now verify that if $Z_0(\tilde{t})$ satisfies (2.61) it must be the case that Z_1 is 1-periodic in τ. If we evaluate (2.53) at $\tau \to \tau + \bar{\psi}$ for an arbitrary fixed phase $\bar{\psi} \in (0,1)$ and integrate over $\tau \in (0,1)$ we get

$$\frac{\partial Z_0}{\partial \tilde{t}} = \int_0^1 G(\Omega(\tau T(Z_0)+\bar{\psi}T(Z_0)+\psi(\tilde{t})),Z_0)d\tau - \omega(\tilde{t})[Z_1(1+\bar{\psi},\tilde{t}) - Z_1(\bar{\psi},\tilde{t})]\,. \tag{2.62}$$

However, our choice of Z_0 in (2.60) implies

$$Z_1(1+\bar{\psi},\tilde{t}) - Z_1(\bar{\psi},\tilde{t}) = 0\,. \tag{2.63}$$

Since $\bar{\psi}$ was arbitrary, (2.63) implies that Z_1 is 1-periodic in τ and guarantees its boundedness in τ.

As mentioned previously, ψ in (2.55) will disappear from our immediate calculations. In order to show that ψ does not affect the value of the integral (2.61), let us introduce the change of coordinates $\eta = \tau T(Z_0) + \psi(\tilde{t})$ to rewrite (2.61)

$$\frac{\partial Z_0}{\partial \tilde{t}} = \frac{1}{T}\int_{\psi}^{T+\psi} G(\Omega(\eta, Z_0), Z_0) d\eta\,. \tag{2.64}$$

Since $G(\Omega(\eta, Z_0), Z_0)$ is $T(Z_0)$-periodic in η

$$\frac{\partial Z_0}{\partial \tilde{t}} = \frac{1}{T}\int_{0}^{T} G(\Omega(\eta, Z_0), Z_0) d\eta \equiv \widehat{G}(Z_0)\,, \tag{2.65}$$

showing that the value of the integral does not depend on $\psi(\tilde{t})$. The right hand equality in (2.65) has been added to emphasize that there is no explicit dependence on $\tilde{t}$ in $\widehat{G}$. In summary, we may now conclude that if

$$\frac{dZ_0}{d\tilde{t}} = \widehat{G}(Z_0)\,, \tag{2.66}$$

then Z_1 is 1-periodic in τ. Since there is no dependence on τ in Z_0, the partial derivative is replaced by the total derivative.

We now apply the preceding general development to (FULL) through the identification that

$$\mathbf{u} = \begin{pmatrix} u \\ w \end{pmatrix}, \qquad \mathbf{z} = \begin{pmatrix} x \\ y \end{pmatrix},$$

in (2.37)-(2.38) and

$$Z_0 = \begin{pmatrix} x_0 \\ y_0 \end{pmatrix}.$$

Specifically, in terms of x we can write

$$\frac{dx_0}{d\tilde{t}} = \frac{1}{T}\int_0^T \left[\frac{h_1(\Omega(\eta, x)) - x(\tilde{t})}{\tau_1}\right] d\eta\,. \tag{2.67}$$

Now define the average of u as

$$\hat{u}(z) \equiv \frac{1}{T(z)}\int_0^{T(z)} \Omega(\eta, z) d\eta\,. \tag{2.68}$$

Recall from (2.14) that $h_1(u)$ was linear. Taking advantage of that linearity and using our definition of the average of u we may rewrite (2.67):

$$\frac{dx_0}{d\tilde{t}} = \frac{\beta_1(\hat{u}(z) - \alpha_1) - x}{\tau_1}\,. \tag{2.69}$$

Then, to leading order, the Averaged Fast Subsystem (AFS) is defined as:

$$\frac{dx}{d\tilde{t}} = \frac{h_1(\hat{u}(x + \gamma y)) - x}{\tau_1} \equiv \widehat{G}_1(x, y), \tag{2.70}$$

$$\frac{dy}{d\tilde{t}} = \frac{h_2(\hat{u}(x + \gamma y)) - y}{\tau_2} \equiv \widehat{G}_2(x, y), \tag{2.71}$$

where we have dropped the subscript$_0$ in both equations.

Below in Theorem 2.1 [27] we will see that to leading-order, the method of averaging implies solutions of (2.70)-(2.71) are asymptotically close to $(x(t), y(t))$ in (2.8)-(2.11) for times $\tilde{t} = O(1)$ (for suitable initial conditions). The Theorem is stated verbatim from the above reference and the proof is expanded and completed from the proof outlined in same.

THEOREM 2.1. *Consider a T-periodic dynamical system of the form*

$$\dot{X} = F(X, t) + \varepsilon G(X, t), \quad X \in \mathbb{R}^n, \tag{2.72}$$

and suppose that the unperturbed system, $\dot{X} = F(X, t)$, has a k-parameter family of T-periodic solutions

$$X(t) = U(t, \alpha), \tag{2.73}$$

where $\alpha = (\alpha_1, ..., \alpha_k)^\top \in \mathbb{R}^k$ *is a vector of independent parameters, which implies that the rank of the* $n \times k$ *matrix* $D_\alpha U$ *is* k*. Suppose the adjoint linear problem*

$$\dot{Q}_i = -\{DF(U(t,\alpha))\}^\top Q_i \tag{2.74}$$

has exactly k *independent* T*-periodic solutions* $Q_1(t,\alpha), ..., Q_k(t,\alpha) \in \mathbb{R}^m$*. Let* Q *be the matrix whose columns are these solutions such that*

$$Q^\top D_\alpha U = I \tag{2.75}$$

where I *is the identity* $k \times k$ *matrix. Then the perturbed system (2.72) has a solution of the form*

$$X(t) = U(t, \alpha(\varepsilon t)) + O(\varepsilon), \tag{2.76}$$

where

$$\frac{d\alpha}{d\tau} = \frac{1}{T}\int_0^T Q(t,\alpha)^\top G(U(t,\alpha),t)dt, \tag{2.77}$$

where $\tau = \varepsilon t$ *is slow time.*

Proof: Let

$$X(t) = U(t, \alpha(\varepsilon t)) + \varepsilon P(t) + O(\varepsilon^2), \tag{2.78}$$

and then substitute $\dot{X}$ into the left hand side of (2.72) and the Taylor expansion of F about U into the right hand side of (2.72) to obtain

$$\dot{U} + \varepsilon D_\alpha U \frac{d\alpha}{d\tau} + \varepsilon \dot{P} + O(\varepsilon^2) = F(U,t) + \varepsilon D_X F(U,t)P + \varepsilon G(U,t) + O(\varepsilon^2). \tag{2.79}$$

Since U was defined as the solution to the unperturbed system, then $\dot{U} = F(U,t)$, so we have

$$\dot{P} = D_X F(U,t)P + G(U,t) - D_\alpha U \frac{d\alpha}{d\tau}, \tag{2.80}$$

which we can rewrite in the form

$$\dot{P} = A(t,\alpha)P + b(t,\alpha), \tag{2.81}$$

where

$$A(t,\alpha) = D_X F(U(t,\alpha),t), \tag{2.82}$$

$$b(t,\alpha) = G(U(t,\alpha),t) - D_\alpha U(t,\alpha)\frac{d\alpha}{d\tau}. \tag{2.83}$$

The Fredholm alternative (see page 146 of Hale [21] for proof of this variation) implies that the linear T-periodic equation (2.81) has a unique solution if and only if the orthogonality condition

$$\langle q, b\rangle = \int_0^T q(t,\alpha)^\top b(t,\alpha)dt = 0 \tag{2.84}$$

is satisfied for any T-periodic solution $q(t,\alpha) \in \mathbb{R}^m$ of the homogeneous adjoint system

$$\dot{q} = -A^\top(t,\alpha)q. \tag{2.85}$$

By assumption, this system has exactly k independent T-periodic solutions $Q_1, ..., Q_k \in \mathbb{R}^m$, which satisfy (2.75). We may rewrite the orthogonality condition in matrix form as

$$\langle Q, b\rangle = \int_0^T Q(t,\alpha)^\top b(t,\alpha)dt \tag{2.86}$$

$$= \int_0^T Q(t,\alpha)^\top \left(G(U(t,\alpha),t) - D_\alpha U(t,\alpha)\frac{d\alpha}{d\tau}\right)dt \tag{2.87}$$

$$= \int_0^T Q(t,\alpha)^\top G(U(t,\alpha),t)dt - \frac{d\alpha}{d\tau}\int_0^T Q(t,\alpha)^\top D_\alpha U(t,\alpha)dt \tag{2.88}$$

$$= 0. \tag{2.89}$$

Now we claim that $Y(t,\alpha) = D_\alpha U(t,\alpha)$ is a matrix solution to the homogeneous linear problem $\dot{Y} = A(t,\alpha)Y$ (the $b \equiv 0$ case in (2.81)). To see this claim, equation (2.73) implies

$$\frac{d}{dt}U(t,\alpha) = F(U(t,\alpha),t), \tag{2.90}$$

thus

$$D_\alpha\left(\frac{d}{dt}U(t,\alpha)\right) = D_\alpha\left(F(U(t,\alpha),t)\right), \tag{2.91}$$

$$\frac{d}{dt}\left(D_\alpha U(t,\alpha)\right) = D_X F(U(t,\alpha),t) D_\alpha U(t,\alpha), \tag{2.92}$$

$$\frac{dY}{dt} = D_X F(U(t,\alpha),t) Y, \tag{2.93}$$

as was claimed. Then by assumption (2.75), we may rewrite the orthogonality condition (2.88)-(2.89) as

$$\int_0^T Q(t,\alpha)^\top G(U(t,\alpha),t)dt - \frac{d\alpha}{d\tau}T = 0. \tag{2.94}$$

Which simplifies to the form given in (2.77). ∎

We should point out that in the application of Theorem 2.1 to our two slow variable model, $k = 1$ with $\alpha = z = x + \gamma y$. In terms of our model, the functions in (2.72) are:

$$X = \begin{pmatrix} u \\ w \\ x \\ y \end{pmatrix}, \tag{2.95}$$

$$F(X,t) = \begin{pmatrix} f(u) - w - x - \gamma y \\ g(u) - w \\ 0 \\ 0 \end{pmatrix}, \tag{2.96}$$

$$G(X,t) = \begin{pmatrix} 0 \\ 0 \\ \frac{h_1(u)-x}{\tau_1} \\ \frac{h_2(u)-y}{\tau_2} \end{pmatrix}. \tag{2.97}$$

Secondly, we start the proof with an assumed expansion (2.78). The existence of such an expansion is guaranteed for systems of the form $\dot{x} = f(x,\varepsilon)$ provided f is C^k smooth in x and ε then $f(x,\varepsilon)$ has $(k-1)^{th}$ order Taylor series expansion [21].

At this point the observant reader may ask, why not first present the theorem and then do the construction of the condition for a valid periodic expansion? Essentially,

the reason is that the construction portion of the theorem requires the determination of the fundamental matrix solution Q. Since this is a difficult process, we choose to instead use a multiple scales approach, as detailed above since the averaged system (2.65) is known explicitly in terms of the periodic orbits Ω (and not in terms of the periodic solutions of the adjoint problem). The theorem is used to validate the existence of periodic solutions with expansions of the form (2.76) (and hence (2.40)-(2.41)) to the perturbed problem valid for long times, $t = O\left(\frac{1}{\varepsilon}\right)$.

Finally, if (2.77) has a stable equilibrium, then the system (2.72) has a T-periodic solution [21], so (2.77) may be interpreted as the condition that the $O(\varepsilon)$ correction in

$$U = U_0 + \varepsilon U_1 + O(\varepsilon^2), \tag{2.98}$$

is periodic (bounded), where U_0 is the T-periodic solution to the unperturbed problem.

Parameter Classification

The parameter classification of models with one-slow variable has been studied extensively; in terms of bifurcation parameters [29], [30], and in the context of pancreatic β-cell models [3] and more importantly a complete classification of the (FS) parameters in our model [42], [14]. We are interested in knowing how to choose parameters to guarantee type I bursting solutions (fold/homoclinic) with a (FS) structure like that in Figure 4. Furthermore, we would like to know how to choose parameters to yield equilibria, of a predetermined stability, on $\mathcal{S}_L$.

Fast parameters

We define parameters to be *fast parameters* if they occur in (FS) but not (SS)

and in a similar fashion refer to *slow parameters* as parameters which occur in (SS) but not (FS). In our two-slow variable model the fast parameters are those that appear solely in (2.8)-(2.9), in particular, (a, η, μ). The parameter γ may appear to be a fast parameter due to its appearance in (FS). However, γ also appears in the (SS) so is neither a fast or a slow parameter by our definition.

By keeping the form of the (FS) in our two-slow variable model the same as in the one-slow variable model (2.1)-(2.3) we are able to take advantage of all the prior analysis and (FS) parameter classification done on this system [42], [14]. By varying the (FS) parameter values square-wave bursting, "parabolic-amplitude" bursting, beating, tapered bursting and other oscillations may be observed. In our analysis, we will choose (FS) parameters to yield square wave bursts. This choice of parameters $(a, \eta, \mu) = \left(\frac{1}{4}, \frac{3}{4}, \frac{3}{2}\right)$ is made with the aid of Figure 6 in Pernarowski 94 [42], reproduced here in Figure 6. For the remainder of this thesis we fix (a, η, μ) at these values.

This choice of parameters yields a bifurcation structure in z that is the same as that of the one-slow variable model (2.1)-(2.3), as shown in Figure 4. It is worth mentioning, that the location of equilibria of (FS) do not depend on any of the fast parameters. With these parameters fixed, we will explore the dependence of bursting solutions on the (SS) parameters (and γ).

Slow parameters

We mentioned the large body of work done classifying the (FS) parameters. A similar body of work organizing the (SS) parameters, with regard to equilibria location and stability (in two slow variable models), does not yet exist. One of our goals in this work is to begin organizing the (SS) parameter space as to possible qualitative features. In the analysis of our two-slow variable model, the (FS) parameters

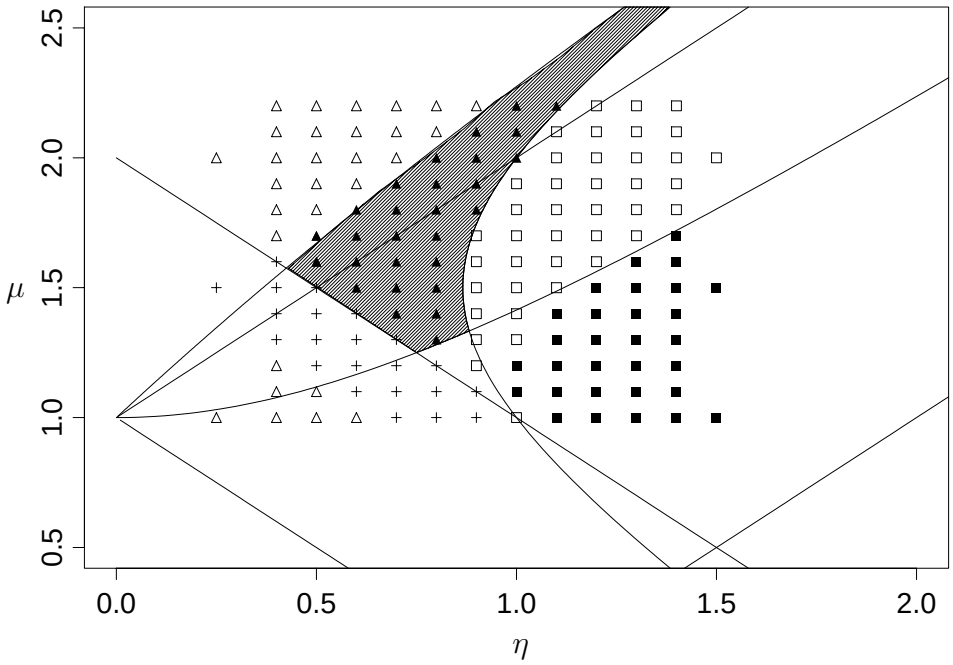


Figure 6: FS parameter selection diagram. FS parameter space projected onto (η, μ)-plane. For parameter values inside the shaded region the model exhibits square-wave bursting. With the parameter $a = 1/4$ fixed, the various shapes indicate different behaviors of the model solution: square-wave bursting (solid triangles), tapered bursting (triangles), nearly parabolic bursting (solid squares), beating (squares) and parabolic-amplitude bursting (crosses). (Reproduced from [42])

remain fixed and we vary just the (SS) parameters $(\beta_i, \alpha_i, \tau_i, \gamma;\ i = 1, 2)$. Before discussing the manner in which we select (SS) parameters, we will describe the possible variations of our model (FULL). We will also address some of our goals in the context of the particular organization we have chosen for our model variations.

In Chapter 1, the physiological concepts of activation and inactivation and their relation to the (SS) parameters (β_i) were introduced. In this chapter we will use the notation $(+,+)$ to refer to the case where both slow variables x and y are activation variables; in other words $\beta_i > 0$, $i = 1, 2$. Analogous definitions hold for the cases $(-,-)$ and $(+,-)$.

Activation/ Inactivation

Variation	Slow variables are
$(+,+)$	Both activation
$(-,-)$	Both inactivation
$(+,-)$	Mixed activation/inactivation

Time Constants

$\tau_1 = \tau_2$	Degenerate case reduces to the One-Slow variable model.
$\tau_1 \neq \tau_2$	Non-degenerate case here $(+,-)$ is different from $(-,+)$.

Table 1: Possible variations in the form of the two-slow variable model. The activation/inactivation variation refers to the signs of the parameters (β_1, β_2).

Recall, from (2.10)-(2.11)

$$\frac{dx}{dt} = \varepsilon \frac{h_1(u) - x}{\tau_1} \quad \text{with} \quad h_1(u) = \beta_1(u - \alpha_1) \ ,$$
$$\frac{dy}{dt} = \varepsilon \frac{h_2(u) - y}{\tau_2} \quad \text{with} \quad h_2(u) = \beta_2(u - \alpha_2) \ .$$

In Table 1 we outline the model variations we will consider. The organization of the table is not meant to indicate that the variation of the activation/inactivation (β_i) is mutually exclusive from the variation of the time constants (τ_i). We will consider all combinations of these two parameter variations. This particular choice of organization, specifically our $(+,-)$ notation in reference to activation/inactivation, is in part for consistency with how a physiologist would speak of these variables. A $(-,-)$ case has already been considered in a different model by Smolen *et al* [56] and later by Bertram *et al* [4].

The time constants categorization scheme will aid in the development of portions of the map in Chapter 3. Subsequent analysis of singular constructions of bursting solutions will be organized with respect to the two time constant conditions indicated in Table 1. We begin by considering the case where $\tau_1 = \tau_2$. We

will refer to this as the degenerate case since later we show this case reduces to the one-slow variable model (2.1)-(2.3). We will next consider some numerical results in the $\tau_1 \neq \tau_2$ case.

Equilibria

Since we are interested in bursting solutions, the number, location and type of equilibria are of necessary interest to us. For example, in the single slow variable model, a single equilibrium on the middle branch with $z \in (z_-, z_{\rm HC})$ guarantees bursting solutions (Terman [58]). Information of this type will be used in Chapter 3, and again in Chapter 5 where we explore several dynamically interesting examples. As mentioned in the prior section, the fast parameter space has been well organized. Thus we will concentrate on the slow parameters while we are looking at factors effecting equilibria.

Location

As in the one-slow variable model, we need to know what parameter sets yield bursting solutions and what the stability of equilibria are when they occur on $\mathcal{S}_L$. In the case of the two-slow variable model, there are many more parameters than the one-slow variable model so the selection of parameter sets is more cumbersome. A system to assist in (SS) parameter selection is developed below.

Equilibria of (FULL) have u values which are roots of

$$\Delta(u) = g(u) + h_1(u) + \gamma h_2(u) - f(u). \tag{2.99}$$

Given the definitions of f, g, h_1, h_2 this can be written as

$$\Delta(u) = u^3 + au + b, \tag{2.100}$$

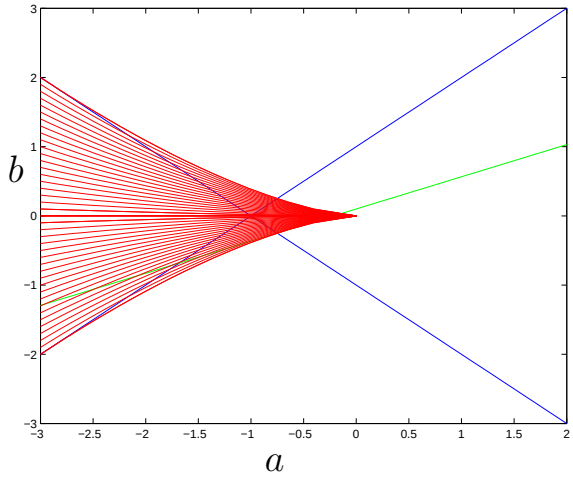


Figure 7: Region of SS parameter diagram where there exist three equilibria of (FULL). The axes are the introduced parameters (a, b) in (2.101)-(2.102).

where we introduce the parameters a and b to simplify this organization scheme:

$$a = \beta_1 + \gamma\beta_2 - 3, \tag{2.101}$$

$$b = -(\alpha_1\beta_1 + \gamma\alpha_2\beta_2 + 3). \tag{2.102}$$

The cubic $\Delta(u)$ in (2.100) will have a single real root only if the discriminant

$$D_\Delta = \frac{b^2}{4} + \frac{a^3}{27}, \tag{2.103}$$

is positive. Solving $D_\Delta = 0$ we obtain the two curves

$$b^\pm = \pm 2\left(\frac{|a|^3}{27}\right)^{1/2}, \quad a < 0,$$

which divide the (a, b)-space into two regions where (FULL) possesses one or three equilibria. The region where three equilibria exist is delineated in Figure 7.

Continuing toward our goal of locating equilibria, we would like to further identify where on the Z shaped manifold, in Figure 4, equilibria are located. Earlier we defined $\mathcal{S}_U$, $\mathcal{S}_M$ and $\mathcal{S}_L$ with reference to upper branch ($u > u_+ = 1$), middle

branch ($u_- < u < u_+$) and lower branch ($u < u_- = -1$) equilibria, respectively. In our (a, b)-space these regions are separated by the straight lines which are the loci $\Delta(u) = 0$ with $u = u_-, u_+$. Each is plotted as $b = -ua - u^3$, linear in a with slope $-u$.

In Figure 8 we illustrate the separation of these regions, as upper, middle and lower branches in terms of the parameters (a, b). In Figure 8A several lines $b = -ua - u^3$ with u values chosen $u < u_-$ are plotted to indicate lower branch equilibria. For each (a, b) pair on these lines (FULL) has at least one equilibrium located on $\mathcal{S}_L$. In Figure 8C analogous lines for several u values chosen in (u_-, u_+) indicate where (FULL) has at least one equilibrium on $\mathcal{S}_M$, the middle branch. In a similar fashion, upper branch equilibria, on $\mathcal{S}_U$, are indicated in Figure 8B. We add one more straight line as above with $u = u_{\text{HC}}$, effectively separating the middle branch into two regions, because of the different dynamics possible in these two regions. We have indicated that portion of $\mathcal{S}_M$ where $u < u_{\text{HC}}$ in Figure 8D. For $u_- < u < u_{\text{HC}}$ we know that equilibrium will be unstable and bursting solutions will persist in the one-slow variable model. But at $u = u_{\text{HC}}$, Terman [58] has proved that chaotic dynamics are possible, hence our separation of the middle branch.

In the left portion of all the graphs in Figure 8 it appears that the various branch regions overlap. That overlap is precisely the region illustrated in Figure 7, where three equilibria exist.

It is worth mentioning again, that the location of equilibria on $\mathcal{S}_L$ in (SS) is the same as in (FULL). Furthermore, the location of equilibria does not depend on τ_1 or τ_2; these time constants only effect the stability.

Using the results of Figure 7 and 8 together, we create the (SS) parameter diagram shown as Figure 9. Superimposed on this figure are letters that reference the ordered triples (U, M, L). Each number in the ordered triple represents the number

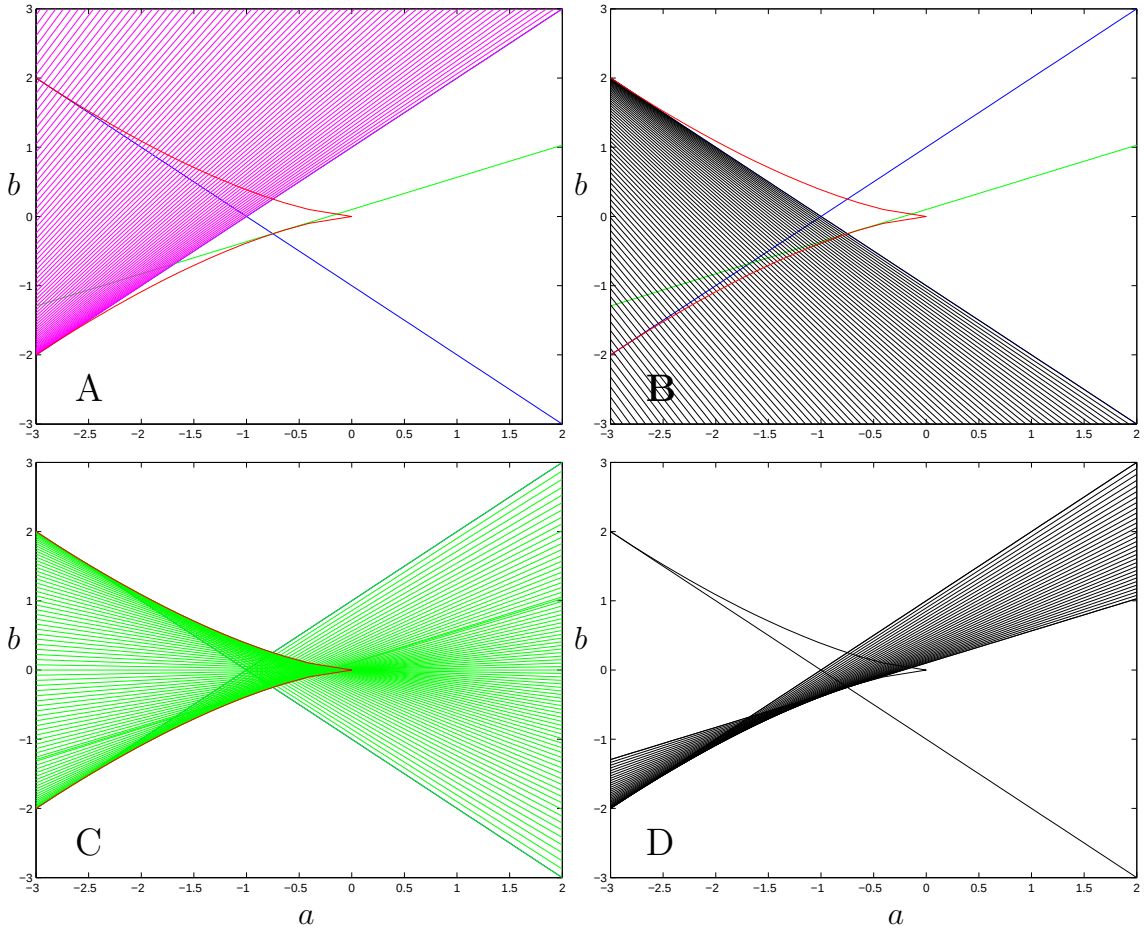


Figure 8: The region of SS parameter diagram where: (A) at least one equilibrium of (FULL) occur on $\mathcal{S}_L$; (B) at least one equilibrium of (FULL) occur on $\mathcal{S}_U$; (C) at least one equilibrium of (FULL) occur on $\mathcal{S}_M$; (D) equilibria occur on $\mathcal{S}_M$ and $u_- < u < u_{\rm HC}$.

of equilibria on the Upper branch, Middle branch and Lower branch, respectively. For example, $\mathcal{A} : (0, 0, 1)$ indicates that the sole equilibrium is lower branch.

In the one-slow variable model when equilibrium occurred on the lower branch and $h'(u) > 0$, in (2.3) they were necessarily stable [43]. But in the two-slow variable model, we will see in the next section that equilibria on $\mathcal{S}_L$ yield a wider range of stabilities not observed in the single slow variable model.

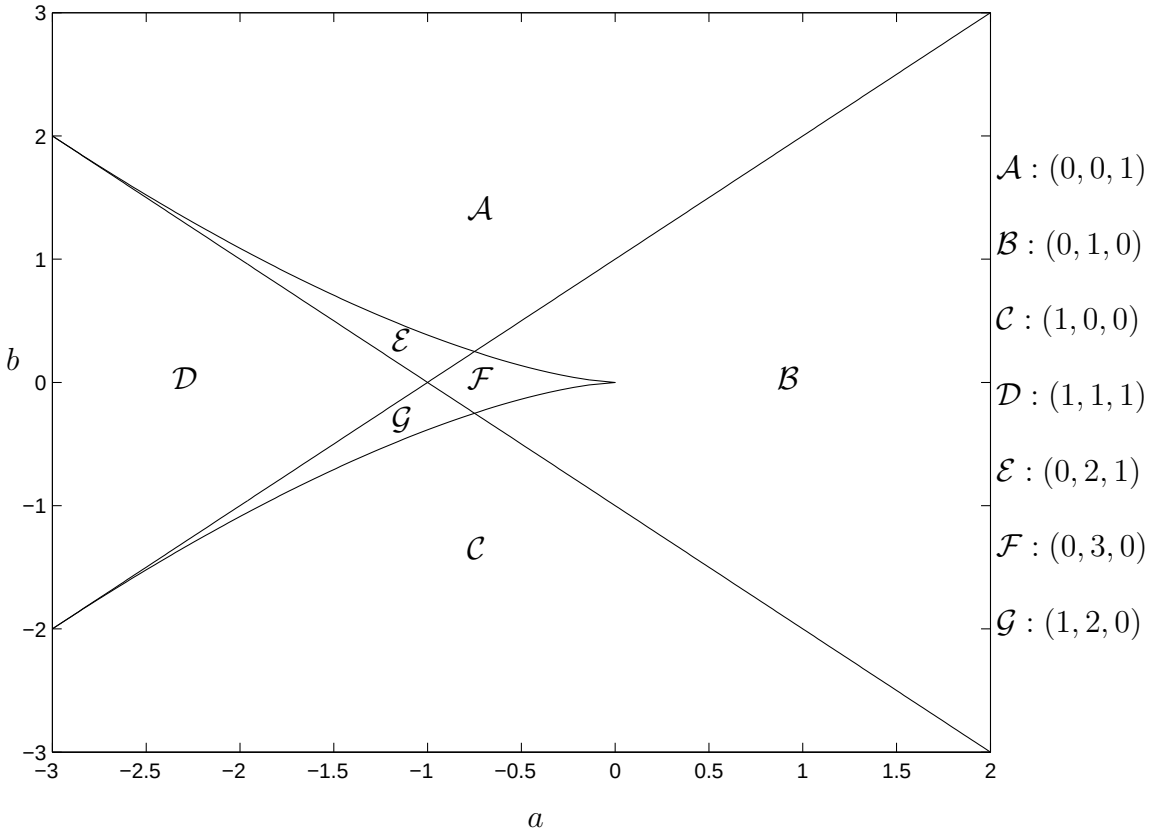


Figure 9: SS parameter diagram. Equilibrium of (FULL) are the roots of $\Delta(u) = g(u) + h_1(u) + \gamma h_2(u) - f(u)$ which can be written as $\Delta(u) = u^3 + au + b$. The constants a and b are defined in terms of SS parameters as follows: $a = \beta_1 + \gamma\beta_2 - 3$ and $b = -(\alpha_1\beta_1 + \gamma\alpha_2\beta_2 + 3)$. The legend at right is described in the text.

Stability

Our goal in this stability analysis is not the complete characterization of the six dimensional (SS) parameter space, but several more modest goals. We wish to organize the parameter space in such a way as to facilitate (SS) parameter selection to yield bursting solutions in the degenerate case. Furthermore, we are interested in showing the existence of bistability between an equilibrium on $\mathcal{S}_L$ and bursting solutions of (FULL), and a process to assist in the determination of (SS) parameters which yield such bistability. We would also like to know what other types of qualita-

tive features are possible, some of which shall be explored in Chapter 5. Lastly, we wish to lay the ground work for a future complete characterization of the parameter space.

To begin addressing stability issues, (FULL) can be written:

$$\frac{d\vec{\mathbf{x}}}{dt} = \vec{\mathbf{F}}(\vec{\mathbf{x}}) = \begin{pmatrix} f(u) - w - x - \gamma y \\ g(u) - w \\ \varepsilon \frac{h_1(u) - x}{\tau_1} \\ \varepsilon \frac{h_2(u) - y}{\tau_2} \end{pmatrix}, \quad \vec{\mathbf{x}} = \begin{pmatrix} u \\ w \\ x \\ y \end{pmatrix}. \tag{2.104}$$

An equilibrium, $\vec{\mathbf{x}}_e$, of (FULL) must satisfy,

$$\vec{\mathbf{F}}(\vec{\mathbf{x}}_e) = 0 \quad \Longleftrightarrow \quad \vec{\mathbf{x}}_e = (\bar{u}, \bar{w}, \bar{x}, \bar{y}) = (\bar{u}, g(\bar{u}), h_1(\bar{u}), h_2(\bar{u})),$$

where $\bar{u}$ is a root of $\Delta(u)$ defined in (2.99). Here we present a leading order argument regarding the stability of equilibria located on the (SS) manifold. We know that the (SS) manifold is stable with respect to the fast dynamics, as such, two of the eigenvalues λ will have $\Re e(\lambda) < 0$. These two eigenvalues are $O(1)$ in ε and are associated with the (FS). The other two eigenvalues are 'small' relative to the (FS) eigenvalues and are associated with the (SS).

The Jacobian of (FULL)

$$D\vec{\mathbf{F}} = \begin{bmatrix} f'(u) & -1 & -1 & -\gamma \\ g'(u) & -1 & 0 & 0 \\ \varepsilon \frac{h_1'(u)}{\tau_1} & 0 & -\frac{\varepsilon}{\tau_1} & 0 \\ \varepsilon \frac{h_2'(u)}{\tau_2} & 0 & 0 & -\frac{\varepsilon}{\tau_2} \end{bmatrix}, \tag{2.105}$$

has the characteristic polynomial

$$P(\lambda) = det\left(D\vec{\mathbf{F}} - \lambda I\right).$$

The associated characteristic polynomial of (FS) is

$$P_0(\lambda) = det\left(D\vec{\mathbf{F}}_0 - \lambda I\right),$$

where

$$\vec{\mathbf{F}}_0(\vec{\mathbf{x}}) = \begin{pmatrix} f(u) - w - z \\ g(u) - w \end{pmatrix}.$$

Using the expansion

$$\lambda = \lambda_0 + \varepsilon\lambda_1 + \varepsilon^2\lambda_2 + \dots,$$

in $P(\lambda)$, one finds

$$P(\lambda) = \lambda_0^2 P_0(\lambda_0) + \varepsilon P_1(\lambda_0, \lambda_1) + \varepsilon^2 P_2(\lambda_0, \lambda_1, \lambda_2) + O(\varepsilon^3), \tag{2.106}$$

where for the moment we do not explicitly state P_0, P_1, P_2. Considering first the case $\lambda_0 \neq 0$, lower branch equilibria have $\Re e(\lambda_0) < 0$ since such λ_0 are the same eigenvalues as (FS). For the $\lambda_0 = 0$ case, it is easily verified that

$$P_1(0, \lambda_1) = 0, \qquad \forall \lambda_1.$$

So the 'small' eigenvalues for the (SS) require examining the $O(\varepsilon^2)$ term in (2.106). Explicit calculations reveal

$$P_2(0, \lambda_1, \lambda_2) = Q(\lambda_1) \equiv q_2\lambda_1^2 + q_1\lambda_1 + q_0, \tag{2.107}$$

where the coefficients of Q in (2.107) are given by

$$q_2 = -G'(\bar{u}), \tag{2.108}$$

$$q_1 = \frac{\beta_1\tau_2 + \gamma\beta_2\tau_1 - G'(\bar{u})(\tau_1 + \tau_2)}{\tau_1\tau_2}, \tag{2.109}$$

$$q_0 = \frac{\beta_1 + \gamma\beta_2 - G'(\bar{u})}{\tau_1\tau_2}. \tag{2.110}$$

Notice that there is no dependence on λ_2 in $P_2(0, \lambda_1, \lambda_2)$, and that Q is quadratic in λ_1. For the remainder of this section we drop the overbar notation on u.

With the goal of determining the stability of equilibria on $\mathcal{S}_L$, we are interested in the sign of the real parts of the roots of (2.107). Moreover, we are interested in the

dependence of the said stability on the parameters (β_1, β_2), and the identification of Hopf bifurcations. We choose (β_1, β_2) as key parameters to vary since they relate to the activation/inactivation definitions of Chapter 1 as described earlier in this chapter.

We reiterate, that an equilibrium located on $\mathcal{S}_L$ implies that two of the eigenvalues satisfy $\Re e(\lambda) < 0$. Thus, the stability of such an equilibrium is determined by the remaining small eigenvalues. Also if the eigenvalues of $D\vec{\mathbf{F}}(\vec{\mathbf{x}}_e)$, transversely crossed the imaginary axis as a parameter is varied, then $\vec{\mathbf{x}}_e$ would be a Hopf point. Our interest in Hopf bifurcations is in the location, within our (SS) parameter space, of interesting dynamics of solutions.

For the $\lambda_0 = 0$ case, from (2.107),

$$\lambda_1^{\pm} = \frac{-q_1 \pm \sqrt{q_1^2 - 4q_2q_0}}{2q_2}. \tag{2.111}$$

We observe that $u < -1$ on $\mathcal{S}_L$, which means the quantity $G'(u) = -3u^2 + 3$ is negative on $\mathcal{S}_L$ so that

$$\vec{\mathbf{x}}_e \in \mathcal{S}_L \Rightarrow q_2 > 0.$$

This result and the signs of the coefficients (q_1, q_0), based on the signs of (β_1, β_2), are organized in Table 2, for $\tau_1 > 0$ and $\tau_2 > 0$. Given the signs of the coefficients q_i we are able to then say something about the stability of $\mathcal{S}_L$ equilibria.

Recall that $0 < \gamma,\ 0 < \tau_i,\ i = 1, 2$ and that for equilibria on $\mathcal{S}_L$ the quantity q_2 is positive. When $(\beta_1, \beta_2) = (+, +)$, ie., both positive, one sees immediately that $q_1 > 0$ and $q_0 > 0$ as well. As such, any $\mathcal{S}_L$ equilibria in this case will be stable as noted in Table 2.

When $(\beta_1, \beta_2) = (-, -)$ then it is possible for q_0 to be positive or negative. We

Case	sign(q_2)	sign(q_1)	sign(q_0)	Equilibria
$(+,+)$	$+$	$+$	$+$	stable
$(-,-)$	$+$	$+$	$+$	stable
		$+/-$	$-$	saddle
$(+,-)$	$+$	$+/-$	$+/-$	HB possible
$(-,+)$	$+$	$+/-$	$+/-$	HB possible

Table 2: Dependence of (SS) equilibria $\vec{\mathbf{x}}_e \in \mathcal{S}_L$ on the parameters (β_1, β_2), where (q_2, q_1, q_0) are the coefficients of the $O(\varepsilon^2)$ term in the characteristic polynomial of (FULL) with $\lambda_0 = 0$. In the table $+/-$ indicates that both signs are possible.

introduce the following definition to assist in understanding this case:

$$\begin{aligned} H(u) &= G(u) - h_1(u) - \gamma h_2(u), \\ H'(u) &= G'(u) - (\beta_1 + \gamma\beta_2). \end{aligned} \tag{2.112}$$

If $q_0 > 0$ then $G'(u) < \beta_1 + \gamma\beta_2$, so we may conclude that the quantity $H'(u) < 0$. Rewriting q_1 in terms of $H(u)$, we find

$$q_1 = -\left(\frac{H'(u)}{\tau_1} + \frac{H'(u)}{\tau_2} + \frac{\gamma\beta_2}{\tau_1} + \frac{\beta_1}{\tau_2}\right). \tag{2.113}$$

We now see that in the $(\beta_1, \beta_2) = (-,-)$ case if $q_0 > 0$ then $q_1 > 0$ as well and such $\vec{\mathbf{x}}_e \in \mathcal{S}_L$ are stable.

When $(\beta_1, \beta_2) = (-,-)$ and $q_0 < 0$ it is possible that q_1 is positive or negative. But in any case, these equilibria are saddles. This is because the discriminant $\sqrt{q_1^2 - 4q_2q_0} > |q_1|$ due to $4q_2q_0 < 0$. Thus, even in the $q_1 = 0$ case, equilibria must be saddles, as summarized in Table 2.

Finally, we consider the $(\beta_1, \beta_2) = (+,-)$ and $(\beta_1, \beta_2) = (-,+)$ cases together. Calculations reveal that restrictions on the sign of q_0 do not place similar restrictions on the sign of q_1; any sign is possible. Thus, we now find that Hopf bifurcations are possible.

In order to show the existence of Hopf bifurcations for equilibria on $\mathcal{S}_L$, we still consider the $\lambda_0 = 0$ case, and rescale our λ expansion as:

$$\Lambda(\varepsilon, \mu) = \lambda_1(\mu) + \varepsilon\lambda_2(\mu) + \varepsilon^2\lambda_3(\mu) + \dots ,$$

where μ is one of the slow parameters $\{\beta_1, \beta_2, \alpha_1, \alpha_2, \tau_1, \tau_2\}$. Furthermore, we define:

$$R(\varepsilon, \mu) = \Re e(\Lambda(\varepsilon, \mu)). \tag{2.114}$$

One necessary condition for an equilibrium on $\mathcal{S}_L$ to be a Hopf point is that the small eigenvalues Λ are purely imaginary. To show this we appeal to the implicit function theorem below. Another necessary condition is that the eigenvalues cross the imaginary axis transversely, or equivalently, $\frac{\partial R}{\partial \mu}(\varepsilon, \mu^*(\varepsilon)) \neq 0$ at the Hopf point μ^*.

We rely on the implicit function theorem to show the existence of a smooth function $\bar{\mu}(\varepsilon)$ such that $R(\varepsilon, \bar{\mu}(\varepsilon)) = 0 \ \forall \varepsilon \in N_r(0)$ where $N_r(0) = \{\varepsilon : |\varepsilon| < r\}$. Such a function exists provided there is a μ_0 that satisfies:

$$R(0, \mu_0) = 0, \tag{2.115}$$

$$R_\mu(0, \mu_0) \neq 0. \tag{2.116}$$

The condition in (2.115) in terms of the coefficients of Q is $R(0, \mu) = q_1 = 0$, which we can write as:

$$q_1 = 0 \iff \beta_1\tau_2 + \gamma\beta_2\tau_1 = G'(u)(\tau_1 + \tau_2).$$

To illustrate that the conditions of the implicit function theorem are satisfied we now select a particular slow parameter. For ease in calculations we begin by letting $\mu = \tau_1$ and fix the remainder of the parameters

$$(\beta_1, \beta_2, \alpha_1, \alpha_2, \tau_2) = (4, -3, -1, -0.5, 0.3), \tag{2.117}$$

and $\gamma = 1$. As such, we may rewrite the condition:

$$q_1 = 0 \iff \tau_1^*(u) = \frac{-0.1(3u^2+1)}{u^2-2},$$

for $u \in (-\sqrt{2}, -1)$, which yields a range $\tau_1^* > 0.4$. So, for instance, if $u = -1.267$ at the Hopf point then $\tau_1^* = 1.473$. Thus, the condition (2.115) is satisfied in this particular instance.

Continuing, we note that $R_{\tau_1}(0, \tau_1) = \frac{\partial q_1}{\partial \tau_1}$. Using (2.113) we see that the condition in (2.116) in this instance, with the slow parameters as indicated in (2.117), is equivalent to:

$$\frac{\partial q_1}{\partial \tau_1} = \frac{H'(u) + \gamma\beta_2}{\tau_1^2} \neq 0, \tag{2.118}$$

which is satisfied provided $\beta_1 \neq 3 - 3u^2$. For equilibria on $\mathcal{S}_L$, this is true if $\beta_1 > 0$. Thus, the implicit function theorem guarantees a smooth function $\tau_1(\varepsilon)$, with $\varepsilon \in N_r(0)$, such that $\Lambda(\varepsilon, \tau_1(\varepsilon)) = i\omega$. It remains to be shown that $\omega \neq 0$ and the transversality condition in τ_1 is satisfied.

Since we have previously established that q_2 is positive, showing that $q_0 > 0$ will show $\omega \neq 0$. In terms of $G'(u)$:

$$q_0 > 0 \iff G'(u) < \beta_1 + \gamma\beta_2.$$

Since $G'(u) = 3 - 3u^2$ and $u < -1$ for $\vec{\mathbf{x}}_e \in \mathcal{S}_L$, this condition is satisfied when $0 < \beta_1 + \gamma\beta_2$, specifically with our parameters as indicated in (2.117) the quantity $\beta_1 + \gamma\beta_2 = 1$, thus establishing $q_0 > 0$ and $\omega \neq 0$.

To show the eigenvalues cross the imaginary axis transversely, we must show that

$$\frac{\partial R}{\partial \mu}(\varepsilon, \mu)\bigg|_{\mu=\bar{\mu}(\varepsilon)} \neq 0,$$

for $\varepsilon \in N_r(0)$. Since $\bar{\mu}(\varepsilon)$ is smooth, it suffices to show that:

$$\frac{\partial R}{\partial \mu}(0, \mu_0) \neq 0.$$

In our current example with $\mu = \tau_1$ this last condition is equivalent to showing $\frac{\partial q_1}{\partial \tau_1} \neq 0$, as was done in (2.118). Thus, in this particular instance we have shown the existence of a Hopf bifurcation in the parameter τ_1 at $\tau_1 = \tau_1^*(u)$, and ε sufficiently small.

Similar, but more complicated, computations reveal Hopf bifurcations in other parameters such as β_1 and β_2. Numerical verification of the existence of these Hopf bifurcations is shown in Figure 10, a bifurcation diagram of (FULL) in the parameter τ_1 with the slow parameter set $(\beta_1, \beta_2, \alpha_1, \alpha_2, \tau_2) = (4, -3, -1, -0.5, 0.3)$ and $\gamma = 1$. Earlier we stated that the location of equilibria is not dependent on the time constants. This figure clearly shows that the u value of the equilibrium ($u = -1.267$ in this example) does not change as the parameter τ_1 is varied. We also note the numerically computed subcritical Hopf bifurcation at $\tau_1 \approx 1.474$ supports the analytic computations above where we calculated a Hopf bifurcation at $\tau_1 \approx 1.473$.

Now that we have shown the existence of Hopf points on $\mathcal{S}_L$ we would like to expedite the location (in our (SS) parameter space) of such points, again with the goal of assisting in the determination of interesting dynamics of solutions.

To summarize, in terms of $G'(u)$ and the other parameters, the conditions for such a Hopf point are:

$$q_0 > 0 \iff G'(u) < \beta_1 + \gamma\beta_2, \tag{2.119}$$

$$q_1 = 0 \iff \beta_1\tau_2 + \gamma\beta_2\tau_1 = G'(u)(\tau_1 + \tau_2), \tag{2.120}$$

$$\Delta(u) = u^3 + au + b = 0. \tag{2.121}$$

The last condition is the requirement (2.100) that u be an equilibrium.

We would like to use these requirements to generate a Hopf bifurcation curve, and then overlay this Hopf curve on our (SS) parameter diagram (Figure 9). Toward

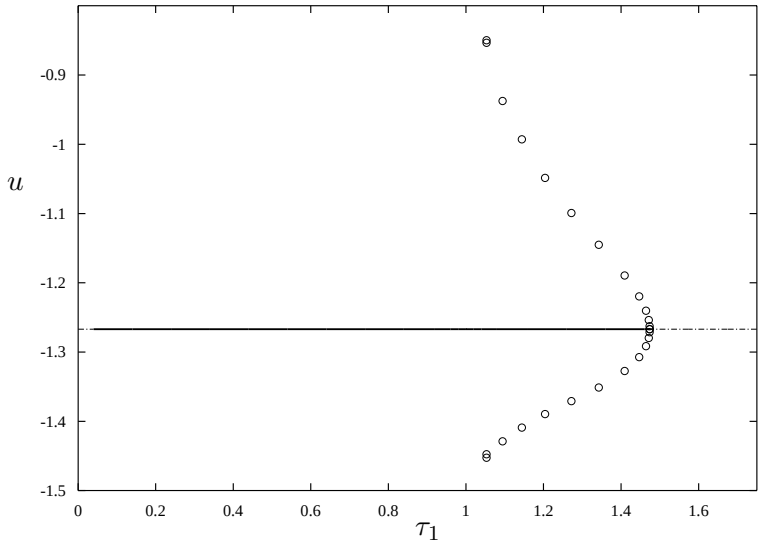


Figure 10: Bifurcation diagram in the bifurcation parameter τ_1 for the (SS) parameter set $(\beta_1, \beta_2, \alpha_1, \alpha_2, \tau_2) = (4, -3, -1, -0.5, 0.3)$ and $\gamma = 1$. Shows a subcritical Hopf bifurcation with unstable periodic orbits emanating from a Hopf point at $\tau_1 \approx 1.474$.

this end, we begin with our (a, b) parameter definitions (2.101)-(2.102), and solve for (β_1, β_2):

$$\beta_1 = \frac{b + 3 + \alpha_2(a + 3)}{\alpha_2 - \alpha_1}, \tag{2.122}$$

$$\beta_2 = \frac{b + 3 + \alpha_1(a + 3)}{\gamma(\alpha_1 - \alpha_2)}. \tag{2.123}$$

In principle, substituting these (β_1, β_2) values into our requirement for a Hopf point (2.120), we get our Hopf condition as a function $b = b(a, u^*)$ where u^* is the value of u where this Hopf point occurs. One gains no insight seeing this rather messy function written out, so it is omitted here. Instead, we parameterize the Hopf curve in (a, b)-space in u by solving the conditions (2.120)-(2.121) and using (2.122)-(2.123). This solution is the Hopf bifurcation curve we set out to find, parameterized in u, as the

ordered pairs $(a,b) = (a_{\text{HB}}(u), b_{\text{HB}}(u))$:

$$a_{\text{HB}}(u) = \zeta_5 u^3 + 3\zeta_3 u^2 - 3\zeta_4, \tag{2.124}$$

$$b_{\text{HB}}(u) = -(2\zeta_3 + \zeta_4 - \zeta_5)u^3 + 3\zeta_4 u, \tag{2.125}$$

and note that u must be in a range so that (2.119) is satisfied and $u < -1$ so that equilibria are on the lower branch $\mathcal{S}_L$. In (2.124)-(2.125), ζ_i are the following functions of u:

$$\begin{aligned}
\zeta_3(u) &= \frac{\tau_1\alpha_1 - \tau_1\alpha_2 + \tau_2\alpha_1 - \tau_2\alpha_2}{(\tau_1 - \tau_2)u + \tau_2\alpha_2 - \tau_1\alpha_1}, \\
\zeta_4(u) &= \frac{\tau_2 - \tau_1 + \tau_2\alpha_1 - \tau_1\alpha_2}{(\tau_1 - \tau_2)u + \tau_2\alpha_2 - \tau_1\alpha_1}, \\
\zeta_5(u) &= \frac{\tau_2 - \tau_1}{(\tau_1 - \tau_2)u + \tau_2\alpha_2 - \tau_1\alpha_1}.
\end{aligned}$$

Thus far in our derivation of the Hopf bifurcation curve we have not used the condition (2.119). Since $G'(u) = 3 - 3u^2$, then (2.119) is satisfied automatically for all $u < -1$ when $\beta_1 + \gamma\beta_2 > 0$. Moreover, we may rewrite this condition in the form $-3u^2 < \beta_1 + \gamma\beta_2 - 3$, then using our definition of the parameter a in (2.101) we have $-3u^2 < a$. On $\mathcal{S}_L$, $u < -1$, thus (2.119) is satisfied for all $a > -3$ in Figure 11. In practice, when our code generates a Hopf bifurcation curve the condition (2.119) is rechecked for each u value.

As a verification of this process for the location of a Hopf point we offer the following example. For a fixed set of slow parameters $(\alpha_1, \alpha_2, \tau_1, \tau_2) = (-1, -0.5, 1, 0.3)$ and $\gamma = 1$, we plot the Hopf bifurcation curve over a range of u values in Figure 11. The curve is plotted as 'x' marks representing the ordered pairs $(a,b) = (a_{\text{HB}}(u), b_{\text{HB}}(u))$, superimposed on the SS parameter diagram (Figure 9). The circled x, marks a Hopf Bifurcation having $u_{\text{HB}} = -1.16$ in terms of our parameters (a,b). Notice this intersection is at $(a,b) = (-0.824, 0.606)$ and corresponds to

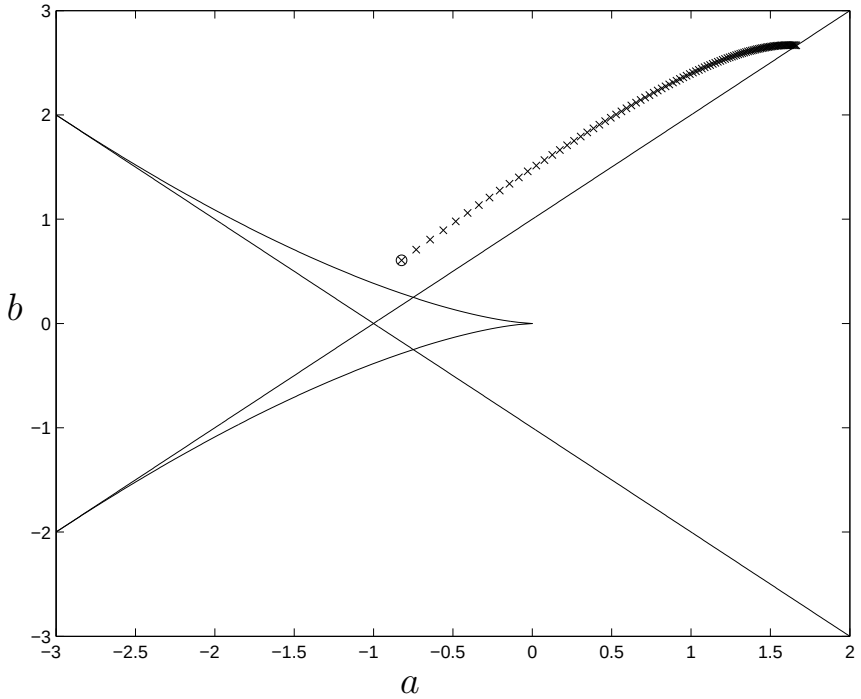


Figure 11: SS parameter diagram with superimposed Hopf bifurcation curve over a range of u values $u \in (-1.16, -1)$ (plotted as x's). For the (SS) parameters $(\alpha_1, \alpha_2, \tau_1, \tau_2, \gamma) = (-1, -0.5, 1, 0.3, 1)$. The circled x indicates a leading order Hopf bifurcation in terms of (a, b) for $u = -1.16$.

$(\beta_1, \beta_2) = (5.0348, -2.8583)$ with our other slow parameters fixed. Furthermore, notice the intersection occurs in the region where the sole equilibrium is on $\mathcal{S}_L$.

Next we compare this approximation of the Hopf bifurcation to one numerically computed using xppaut [19] on (FULL) with the same set of slow parameters as in Figure 11 and choosing $(\beta_1, \beta_2) = (5.035, -2.858)$ associated with the Hopf point found above for $u = -1.16$. In the numerical results shown in Figure 12, we see the projection of trajectories into the (x, y)-plane with the parameter values stated above. There is an unstable equilibrium located inside of what appears to be the limit cycle. The equilibrium is at $(\bar{u}, \bar{w}, \bar{x}, \bar{y}) = (-1.16, -1.12, -0.806, 1.89)$ with eigenvalues $(-0.819 \pm 0.607i,\ 0.000034 \pm 0.0080i)$. The inner trajectory is close

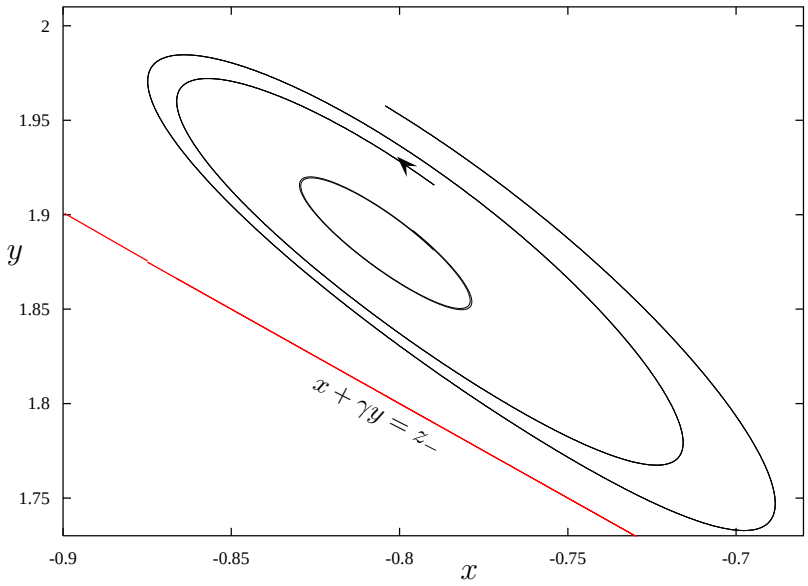


Figure 12: Slow flow near the numerically approximated Hopf point. Trajectories of (FULL) with parameter values $(\beta_1, \alpha_1, \beta_2\alpha_2, \tau_1, \tau_2) = (5.0348, -1, -2.8583, -0.5, 1, 0.3)$.

enough to the equilibrium that it looks like a limit cycle, even after five cycles. With the initial values (x_0, y_0) pushed out slightly, we observe weak outward spiraling.

Results of the type indicated in Figure 12 are promising, but to better verify the Hopf bifurcation we generated a bifurcation diagram in the parameter β_2 which is shown in Figure 13. The numerical value of the Hopf bifurcation arrived at in these calculations is $\beta_2 = -2.85899$, which compares favorably with our calculated approximation obtained above ($\beta_2 = -2.85827$). The process for Hopf point determination as described in this section is valuable in determining parameter sets such that qualitative features of solutions not possible with the one-slow variable model are more easily located. We will examine two such examples in Chapter 5.

Lastly, we make some remarks about the role of the time constants τ_1, τ_2 with respect to the stability of equilibria on $\mathcal{S}_L$. Specifically, we can show that the

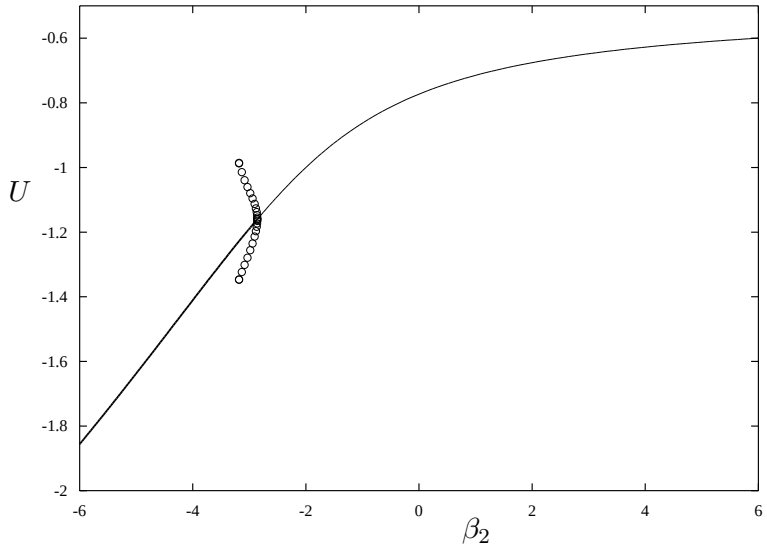


Figure 13: Bifurcation diagram in the bifurcation parameter β_2 for the (SS) parameter set $(\beta_1, \alpha_1, \alpha_2, \tau_1, \tau_2) = (4, -1, -0.5, 1, 0.3)$ and $\gamma = 1$.

stability of equilibria of (FULL) depends only on the ratio

$$\rho = \frac{\tau_1}{\tau_2},$$

to leading order in ε. The eigenvalues associated with (FS) clearly do not depend on τ_1 or τ_2 since $P_0(\lambda)$ does not. Moreover, it can be shown that the sign of $\mathbb{R}e(\lambda_1)$ determined from the condition $Q(\lambda_1) = 0$ only depends on the ratio ρ. To see this, note that the transformations:

$$\begin{aligned} \tau_2 &= \rho\tau_1, \\ \bar{\lambda} &= \frac{\lambda_1}{\tau_1}, \quad \tau_1 > 0, \end{aligned} \tag{2.126}$$

used in $Q(\lambda_1) = 0$ is equivalent to:

$$\bar{Q}(\bar{\lambda}) = \bar{q}_2\bar{\lambda}^2 + \bar{q}_1\bar{\lambda} + \bar{q}_0 = 0,$$

where

$$\begin{aligned}
\bar{q}_2 &= -G'(\bar{u}), \\
\bar{q}_1 &= \frac{\beta_1\rho + \gamma\beta_2 - G'(\bar{u})(1+\rho)}{\rho}, \\
\bar{q}_0 &= \frac{\beta_1 + \gamma\beta_2 - G'(\bar{u})}{\rho}.
\end{aligned}$$

One only need note that $\bar{q}_0, \bar{q}_1, \bar{q}_2$ depend solely on ρ to make the final conclusion that the stability of equilibria of (FULL) depends only on the ratio ρ (to leading order in ε) and not on τ_1 and τ_2 independently.

In this chapter we derived the various model subsystems, and discussed the associated subsystem dynamics. We next organized our model parameters to aid in parameter selection to yield bursting solutions and predict equilibria location and stability. We are now ready to define the return map we will use to characterize singular bursting solutions.

CHAPTER 3

THE RETURN MAP

Overview

We begin this chapter summarizing our definitions of the slow subsystem (SS) and the averaged fast subsystem (AFS) of Chapter 2. Using these definitions we construct the return map ϕ as the composition of two composite maps, one for the active phase, $\widehat{\phi}$, and one for the silent phase, $\widetilde{\phi}$. We identify singular bursting solutions with fixed points $\bar{x}$ of ϕ. In the last section we carefully examine a special case in which the time constants of (FULL) are equal, ie, $\tau_1 = \tau_2$. One result of this examination is the reduction of (FULL), in this special case, to a one-slow variable model.

Overview of the fast, slow and averaged fast subsystems

In the next sections we define the map $\phi : \mathbb{R} \to \mathbb{R}$, used to construct singular approximations to bursting solutions. To define this map we needed to define the slow and averaged fast subsystems, in Chapter 2. These subsystem definitions were made based on the model (FULL). This subsystem decomposition reduces the system, to leading order, from a four dimensional system to two dimensions in our study of the slow evolution of x and y. For convenience we briefly review some of the relevant results from Chapter 2. Also, for both (SS) and (AFS) the slow time was the same, i.e. $\tilde{t} = \varepsilon t$. For notational simplicity we will use $\tau = \varepsilon t$ to denote this slow time henceforth.

Recall that the lower branch equilibria of (FS) form a stable manifold $\mathcal{S}_L$ for the

fast dynamics, and that the projection of $\mathcal{S}_L$ onto the (x, y)-plane is:

$$S_L = \{(x, y) : x + \gamma y = G(u), u < u_-\}.$$

The slow subsystem (SS) is defined by the differential algebraic system:

$$x + \gamma y = G(u)\,, \tag{3.1}$$

$$\frac{dx}{d\tau} = F_1(x, y) = \frac{h_1(u_{\text{LB}}(x + \gamma y)) - x}{\tau_1}\,, \tag{3.2}$$

$$\frac{dy}{d\tau} = F_2(x, y) = \frac{h_2(u_{\text{LB}}(x + \gamma y)) - y}{\tau_2}, \tag{3.3}$$

where u_{LB} in (3.1)-(3.3) is given by (2.33) and (2.34) as discussed on page 22. The slow flow in (3.1)-(3.3) is defined only for those τ such that $(x(\tau), y(\tau)) \in S_L$. For the purpose of this overview we will assume that parameters are chosen so the dynamics described below are true. In particular we assume that parameters are chosen so that the system has a sole equilibrium on $\mathcal{S}_M$ (see Chapter 2 for details).

For initial conditions on $\mathcal{S}_L$, solutions of (SS) are close to solutions of (FULL) for slow times $\tau = O(1)$, or until $z(\tau) = z_-$. Similarly, for initial conditions near $\mathcal{S}_L$ solutions of (SS) are close to true solutions, since the fast dynamics drive trajectories toward the manifold $\mathcal{S}_L$. Thus (SS) solutions serve as a good approximation to true solutions of (FULL) in this region. In either case, $z \equiv x + \gamma y$ values will decrease until $z(\tau) = z_-$. At this point the bistability is lost and a transition to the active phase must occur.

However, in the active phase it is harder to approximate solutions. We applied multiple scales averaging in Chapter 2 to approximate such solutions in our definition of the (AFS). Here a brief overview is presented. Recall our definition of the set

$$S_A = \{(x, y) : z_{HB} < x + \gamma y < z_{\text{HC}}\},$$

and that the slow flow in the (AFS) is defined so long as $(x(\tau), y(\tau)) \in S_A$. In the singular limit, when $z(\tau) = z_{\text{HC}}$, bistability of (FS) is again lost and a transition

to the silent phase must occur. The leading order (AFS) is defined, with slow time $\tau = \varepsilon t$:

$$\frac{dx}{d\tau} = \widehat{G}_1(x,y) = \frac{h_1(\hat{u}(x+\gamma y)) - x}{\tau_1}, \tag{3.4}$$

$$\frac{dy}{d\tau} = \widehat{G}_2(x,y) = \frac{h_2(\hat{u}(x+\gamma y)) - y}{\tau_2}, \tag{3.5}$$

where $\hat{u}$ defined in (2.68) is the average value of u on the limit cycles of (FS).

An overview of the return map

The return map we will construct, is actually the composition of two maps as illustrated in Figure 14. One map accounts for the silent phase (approximated by (SS)) and the other the active phase (approximated by (AFS)). The active phase portion of the singular solution is constructed from a trajectory $\hat{\gamma}_X$ of (AFS) which starts at $\mathbf{X} = (x,y)$ on the curve

$$\Gamma_- = \{(x,y) : x + \gamma y = z_-\} \subset \overline{S}_A, \tag{3.6}$$

and terminates at $\widehat{\mathbf{X}}$ on

$$\Gamma_{\text{HC}} = \{(x,y) : x + \gamma y = z_{\text{HC}}\} \subset \overline{S}_A. \tag{3.7}$$

When such transitions occur this defines a map $\widehat{\Phi} : \mathbb{R}^2 \to \mathbb{R}^2$, such that $\widehat{\mathbf{X}} = \widehat{\Phi}(\mathbf{X})$.

Similarly, the silent phase portion is constructed from a trajectory $\widetilde{\gamma}_X$ of the (SS) which starts at $\widehat{\mathbf{X}}$ on the curve Γ_{HC} and terminates at $\widetilde{\mathbf{X}}$ on the limit point curve Γ_-, which forms a boundary of S_L. This transition defines a map $\widetilde{\Phi} : \mathbb{R}^2 \to \mathbb{R}^2$, such that $\widetilde{\mathbf{X}} = \widetilde{\Phi}(\widehat{\mathbf{X}})$.

The composition of these two maps may be written as $\Phi : \mathbb{R}^2 \to \mathbb{R}^2$, $\mathbf{X} = (x,y)$,

$$\Phi(\mathbf{X}) = \left(\widetilde{\Phi} \circ \widehat{\Phi}\right)(\mathbf{X}). \tag{3.8}$$

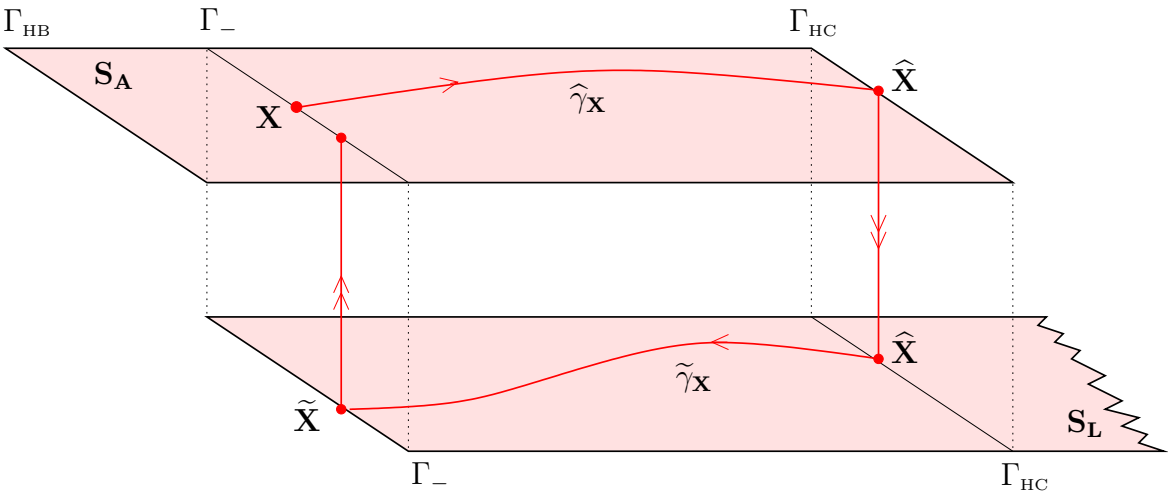


Figure 14: Caricature of the return map definition for Singular Bursting Solutions. Shows S_A on top with a trajectory of the (AFS) $\widehat{\gamma}_{\mathbf{X}}$ beginning at $\mathbf{X} = (x_0, y_0) \in \Gamma_-$. Then the fast transition to S_L on the bottom and the associated trajectory $\widetilde{\gamma}_{\mathbf{X}}$.

Notice that if $\mathbf{X}$ is a fixed point of the map Φ then there exists a singular bursting solution of (FULL). This, in essence is our definition of a singular bursting solution as such a cycle is the leading order approximation of a solution which is both periodic and traverses the active and silent phases once each period.

Construction of the Map

Given the precise definitions of the (SS) and (AFS) in earlier sections we can now construct singular approximations to bursting solutions. Figure 14, presents a graphical caricature of the definitions presented below for the two dimensional map Φ. In Figure 15 we illustrate a dimensionality reduction for this map. A singular approximation of a bursting solution is a periodic solution comprised of two parts. We first consider the active phase portion and exploit some of the special characteristics particular to this system.

For the active phase portion, let $\mathbf{X} = (x_0, y_0) \in \Gamma_-$ and $\widehat{\gamma}_{\mathbf{X}}(\tau) = (\hat{x}(\tau), \hat{y}(\tau))$

be the trajectory of the (AFS) (2.70)-(2.71) with the initial condition $(\hat{x}(0), \hat{y}(0)) = (x_0, y_0)$. For some choices of $\mathbf{X}$, the trajectory $\widehat{\gamma}_{\mathbf{X}}(\tau)$ will reach Γ_{HC} in a finite time T_A. In general, this active phase duration T_A depends on $\mathbf{X}$. Trajectories meeting this criteria define a map $\widehat{\Phi} : \mathbb{R}^2 \to \mathbb{R}^2$, where $\widehat{\Phi}(x_0, y_0) = (\hat{x}(T_A), \hat{y}(T_A))$. Notice we have restricted ourselves to the set of $\mathbf{X}$ such that every trajectory $\widehat{\gamma}_{\mathbf{X}}$ originating on the limit point curve Γ_- reaches the homoclinic curve Γ_{HC} and thus defines the domain of $\widehat{\Phi}$. These trajectories all begin on Γ_- and end on Γ_{HC}.

A feature we may use nicely to our advantage is that y is a function of x on both Γ_- and Γ_{HC}, specifically, on Γ_-: $y = \frac{z_- - x}{\gamma}$ and on Γ_{HC}: $y = \frac{z_{\text{HC}} - x}{\gamma}$. As such, $\widehat{\Phi}$ reduces to a one dimensional map $\widehat{\phi} : \mathbb{R} \to \mathbb{R}$, $\widehat{\phi}(x_0) = \hat{x}(T_A)$. Here $\widehat{x}_0 = \widehat{\phi}(x_0)$ is the x-coordinate of an (AFS) trajectory where bistability is lost and transition to the silent phase is made; in other words the trajectory exits the active phase at Γ_{HC} (via a homoclinic bifurcation). Although, in the more general setting (i.e., other two slow variable models: Bertram [5]; Smolen, Terman [56]; Bertram,*et al* [4]) $\widehat{\gamma}$ depends on $\mathbf{X}$, the aforementioned dimensionality reduction allows us to instead use the notation $\widehat{\gamma}_x(\tau)$ (instead of $\widehat{\gamma}_{\mathbf{X}}(\tau)$) since we no longer have dependence on y. Adopting this convention, the domain of the map $\widehat{\phi}$ can be written:

$$D(\widehat{\phi}) = \{x \in \mathbb{R} \mid \exists T_A < \infty \ni \widehat{\gamma}_x(T_A) \cap \Gamma_{\text{HC}} \neq \phi\},$$

where ϕ is the empty set. Domain issues associated with the map are complicated, and we will see in the next section that the domain of the map ϕ can be nontrivial.

An analogous map for (SS) $\widetilde{\phi} : \mathbb{R} \to \mathbb{R}$ may be defined. As above, let $\widehat{\mathbf{X}} = (\widehat{x}_0, \widehat{y}_0) \in \Gamma_{\text{HC}}$ and $\widetilde{\gamma}_{\mathbf{X}}(\tau) = (\widetilde{x}(\tau), \widetilde{y}(\tau))$ be the trajectory of (3.1)-(3.3) with the initial conditions $(\widetilde{x}(0), \widetilde{y}(0)) = (\widehat{x}_0, \widehat{y}_0)$. Furthermore, we restrict ourselves to the set $\widehat{\mathbf{X}}$ such that $\widetilde{\gamma}_{\mathbf{X}}(\tau)$ reaches Γ_- in a finite time T_S, the silent phase duration. For all such $\widehat{\mathbf{X}}$, and again exploiting the functional relationship of x and y on Γ_{HC} and

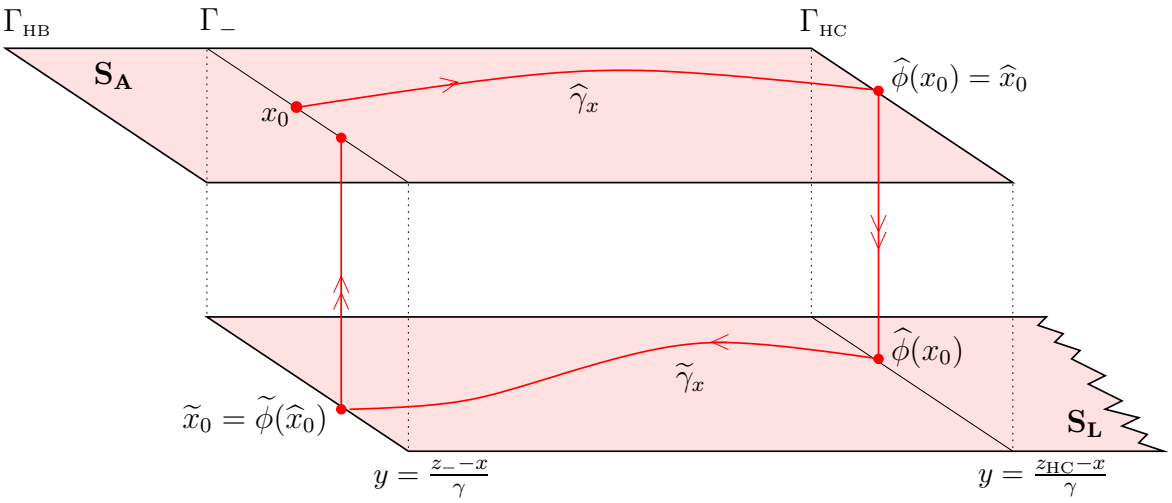


Figure 15: Caricature of the one dimensional return map, showing just the x coordinate of transition points (the y coordinate may be calculated on Γ_- and Γ_{HC} as indicated). Shows S_A on top and S_L on the bottom and the associated trajectories.

Γ_-, we define the map $\widetilde{\phi} : \mathbb{R} \to \mathbb{R}$, $\widetilde{\phi}(\widehat{x}_0) = \tilde{x}(T_s)$. In this case, $\widetilde{x}_0 = \widetilde{\phi}(\widehat{x}_0)$ is the x-coordinate of a (SS) trajectory where bistability is lost and transition to the active phase is made. Again, adopting the convention delineated above, the domain of the map $\widetilde{\phi}$ can be written:

$$D(\widetilde{\phi}) = \{x \in \mathbb{R} \,|\, \exists T_s < \infty \ni \widetilde{\gamma}_x(T_s) \cap \Gamma_- \neq \phi\},$$

Thus, we have defined two 1-dimensional maps, $\widetilde{\phi}$ for the silent portion and $\widehat{\phi}$ for the active portion. We will now use the composition of these two maps to construct a singular solution that starts on the limit point curve Γ_-, traverses the active phase portion until bistability is lost at the homoclinic curve Γ_{HC} and then traverses the slow subsystem manifold to return to Γ_- as per Figure 15.

At this point we acknowledge certain domain issues associated with the composition map $\phi = \widetilde{\phi} \circ \widehat{\phi}$. The domain of ϕ can be written:

$$D(\phi) = \{x \in \mathbb{R} \,|\, x \in D(\widehat{\phi}) \,,\, \widehat{\phi}(x) \in D(\widetilde{\phi})\}.$$

If $R(\widehat{\phi})$ is the range of $\widehat{\phi}$ then, given our previous definitions, the set

$$W \equiv R(\widehat{\phi}) \cap D(\widetilde{\phi}),$$

could be empty, equal to $D(\widetilde{\phi})$ or a (nonempty) strict subset of $D(\widetilde{\phi})$.

In the next section we show that for a subset of slow parameter space, singular bursting solutions exist and W is nonempty. The case where W is a strict subset of $D(\widetilde{\phi})$ relates to bistability between bursting solutions and stable equilibria on $\mathcal{S}_L$. This will be discussed in Chapter 5.

To better describe this composition of these one dimensional maps, if the x-coordinate of initial condition $(x_n(0), y_n(0)) \in \Gamma_-$ is x_n, then the x-coordinate upon return to Γ_-, after one complete cycle, will be

$$x_{n+1} = (\widetilde{\phi} \circ \widehat{\phi})(x_n) \equiv \phi(x_n), \tag{3.9}$$

with an associated y-coordinate

$$y_{n+1} = \frac{z_- - x_{n+1}}{\gamma}.$$

Consequently, if $x_{n+1} = x_n$, the singular solution is periodic. This important observation now allows us to identify singular bursting solutions with fixed points of the composite map ϕ. Moreover, if $\bar{x}$ is a fixed point of the map ϕ (i.e., $\bar{x} = \phi(\bar{x})$) and $|\phi'(\bar{x})| < 1$, then the singular bursting solution is stable.

In all of our analysis the degenerate, $\tau_1 = \tau_2$, case is the starting point. In the next section it will be shown that the map ϕ for the model (FULL) is linear in the degenerate case, thereby rendering stability information on inspection. The linearity of ϕ will be shown as the composition of two linear maps, the details of which are presented at the end of the next section.

Degenerate Case

The degenerate case in our two-slow variable model, is defined to be the case when the two time constants τ_1 and τ_2 are equal. In Chapter 2 we remarked that this case reduces to the one-slow variable model (2.1)-(2.3). The proof of this claim is given below, where we will show that by a simple linear transformation one of the variables is decoupled from the system. As a direct consequence of this proof we will further show that there is a three dimensional invariant subspace (in $\mathbb{R}^4$) that is globally stable.

We consider a linear transformation of (FULL), $(u, w, x, y) \mapsto (u, w, z, p)$ where

$$\vec{\mathbf{Z}} = A\vec{\mathbf{x}} + \vec{\mathbf{b}}, \quad \vec{\mathbf{x}} = (x, y)^T, \quad \vec{\mathbf{Z}} = (p, z)^T, \tag{3.10}$$

$$\frac{d\vec{\mathbf{x}}}{dt} = B\vec{\mathbf{x}} + u\vec{\mathbf{h}} + \vec{\mathbf{k}}\,, \tag{3.11}$$

and (3.10)-(3.11) have the form

$$\begin{pmatrix} p \\ z \end{pmatrix} = \begin{bmatrix} a_{11} & a_{12} \\ 1 & \gamma \end{bmatrix} \begin{pmatrix} x \\ y \end{pmatrix} + \begin{pmatrix} b_1 \\ 0 \end{pmatrix}\,, \tag{3.12}$$

$$\begin{pmatrix} \frac{dx}{dt} \\ \frac{dy}{dt} \end{pmatrix} = \begin{bmatrix} \frac{-1}{\tau_1} & 0 \\ 0 & \frac{-1}{\tau_2} \end{bmatrix} \begin{pmatrix} x \\ y \end{pmatrix} + u \begin{pmatrix} \frac{\beta_1}{\tau_1} \\ \frac{\beta_2}{\tau_2} \end{pmatrix} + \begin{pmatrix} \frac{-\beta_1\alpha_1}{\tau_1} \\ \frac{-\beta_2\alpha_2}{\tau_2} \end{pmatrix}\,, \tag{3.13}$$

and we get to choose a_{11}, a_{12}, and b_1 above.

Assuming $a_{11}\gamma - a_{12} \neq 0$ so that A is invertible, (3.10)-(3.11) imply

$$\frac{d\vec{\mathbf{Z}}}{dt} = ABA^{-1}\vec{\mathbf{Z}} + A\vec{\mathbf{h}}u + (A\vec{\mathbf{k}} - ABA^{-1}\vec{\mathbf{b}}). \tag{3.14}$$

Equivalently,

$$\frac{d\vec{\mathbf{Z}}}{dt} = \begin{bmatrix} \eta_{11} & \eta_{12} & \eta_{13} \\ \eta_{21} & \eta_{22} & \eta_{23} \end{bmatrix} \begin{pmatrix} u \\ z \\ p \end{pmatrix} + \begin{pmatrix} \zeta_1 \\ \zeta_2 \end{pmatrix}, \tag{3.15}$$

for appropriate definitions of η_{ij}, ζ_i. Letting

$$a_{11} = 1 , \tag{3.16}$$

$$a_{12} = -\frac{\beta_1 \tau_2}{\beta_2 \tau_1} , \tag{3.17}$$

$$b_1 = \beta_1(\alpha_1 - \alpha_2) + 1 , \tag{3.18}$$

yields a value $\eta_{11} = \eta_{12} = 0$ effectively decoupling p from the rest of the system. In the degenerate $\tau_1 = \tau_2$ case, with the choice of constants in (3.16)-(3.18) the vector $\vec{\zeta}$ simplifies to:

$$\begin{pmatrix} \zeta_1 \\ \zeta_2 \end{pmatrix} = \frac{1}{\tau_1} \begin{pmatrix} 1 \\ -\beta_1\alpha_1 - \gamma\beta_2\alpha_2 \end{pmatrix},$$

thus system (FULL) becomes:

$$\frac{du}{dt} = f(u) - w - z , \tag{3.19}$$

$$\frac{dw}{dt} = g(u) - w , \tag{3.20}$$

$$\frac{dz}{dt} = \varepsilon \frac{H(u) - z}{\tau_1} , \tag{3.21}$$

$$\frac{dp}{dt} = \varepsilon \frac{1 - p}{\tau_1} , \tag{3.22}$$

where

$$H(u) = \beta^*(u - \alpha^*) , \tag{3.23}$$

$$\beta^* = \beta_1 + \gamma\beta_2 , \tag{3.24}$$

$$\alpha^* = \frac{\beta_1\alpha_1 + \gamma\beta_2\alpha_2}{\beta_1 + \gamma\beta_2} . \tag{3.25}$$

Lastly, we note that the invertibility of $\mathbf{A}$ in (3.10) given (3.16)-(3.17) and $\tau_1 = \tau_2$, is equivalent to the denominator of (3.25) not vanishing.

As claimed, we see that the variable p is decoupled from the rest of the system (3.19)-(3.21), showing the reduction of (FULL) to a one-slow variable model (3.19)-(3.21). This realization reduces the number of the model variations we need to consider.

As shown in Chapter 2, in regard to the one-slow variable model, the inactivation case is not interesting with our goal of finding bursting solutions. As such, in the degenerate case we need only consider the $(+,+)$ and $(+,-)$ cases, since in the $(-,-)$ case β^* in (3.24) is negative and will not yield bursting solutions.

The transformation above gives us another important piece of information. We see in (3.22) that as $t \to \infty$, $p \to 1$, thus we have a three dimensional invariant subspace in $\mathbb{R}^4$ which is globally stable. In other words, trajectories (projected onto the (z,p)-plane) are globally attracted toward the line $p = 1$. This is equivalent to attraction in the (x,y)-plane, for the system (FULL), to the line:

$$y = \frac{\beta_2}{\beta_1}x + \beta_2(\alpha_1 - \alpha_2). \tag{3.26}$$

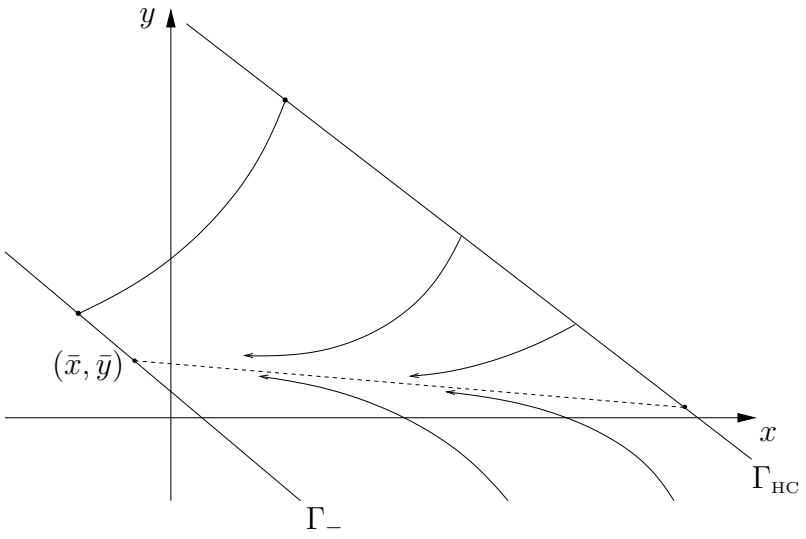


Figure 16: Projection of the invariant subspace onto the (x,y)-plane, in the degenerate, $\tau_1 = \tau_2$, case, illustrating the global attraction of trajectories to the line $y = \frac{\beta_2}{\beta_1}x + \beta_2(\alpha_1 - \alpha_2)$.

This global attraction assures us, in this degenerate case, that for some (β^*, α^*)

with $\beta^* > 0$ there must exist a fixed point $\bar{x}$ for the return map $\phi(x)$; $(\bar{x}, \bar{y})$ as shown in Figure 16. With our identification of map fixed points with bursting solutions, we are assured that singular bursting solutions must exist for some parameters.

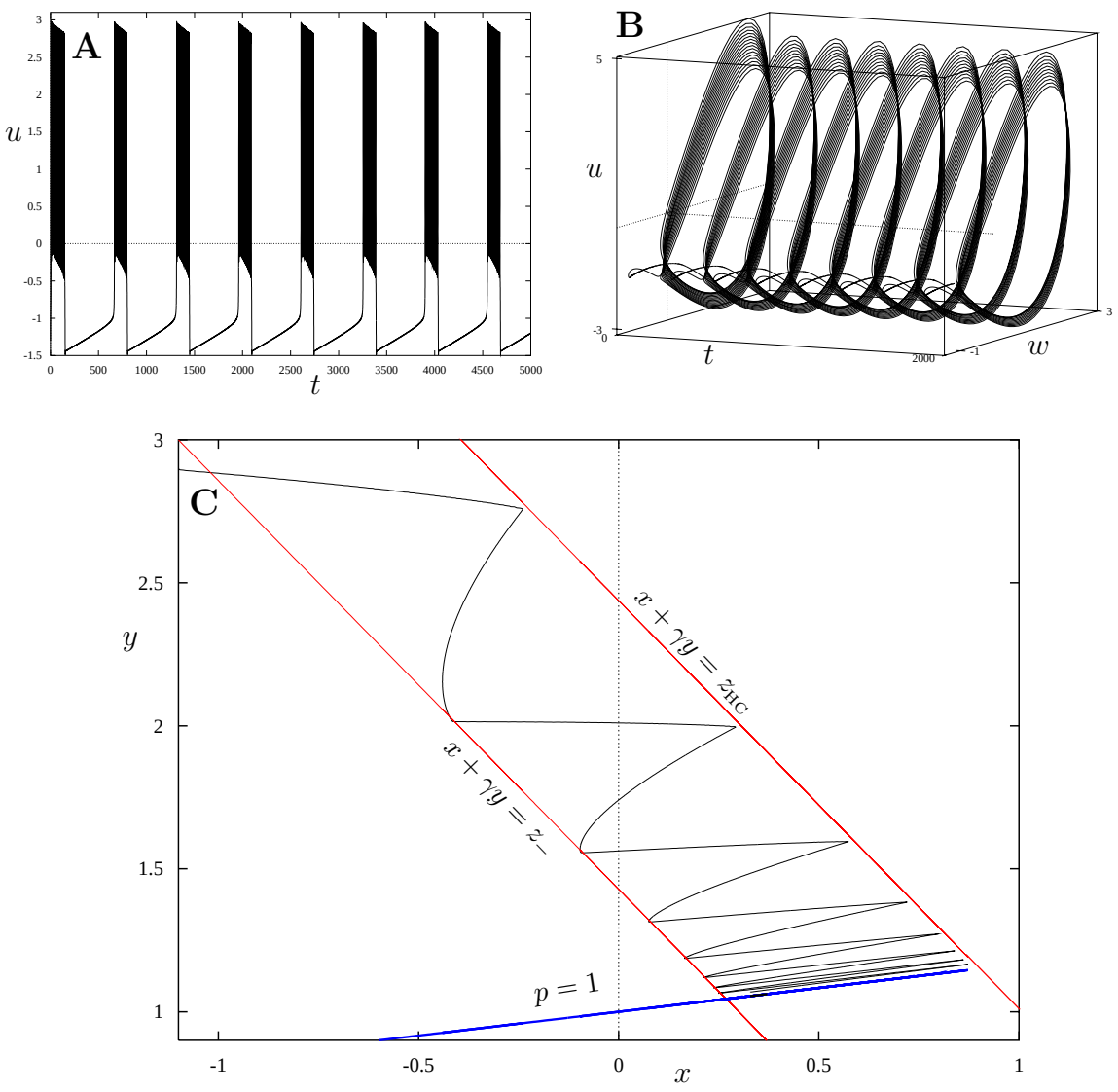


Figure 17: Illustration of the global attraction of projected trajectories in the degenerate case. A shows u vs t for this run. B shows a u and w vs t plot. In C we see the convergence of trajectories projected onto the (x, y)-plane to the line $y = \frac{\beta_2}{\beta_1}x + \beta_2(\alpha_1 - \alpha_2)$.

This finding is fairly important since in all of our discussion of the construction the map ϕ we did not know if the domain of ϕ was empty. But in the degenerate case, when $\beta^* > 0$ and α^* chosen so that $\vec{\mathbf{x}}_e \in \mathcal{S}_L$ and $u_e < u_{\text{HC}}$, the domain is nontrivial, as illustrated in Figure 16.

We further illustrate this global attraction in Figure 17 using xppaut, with parameters $(\beta_1, \alpha_1, \beta_2, \alpha_2, \gamma) = (3, -1, 0.5, -3, 0.7)$, for the degenerate case. In Figure 17A we see square-wave bursting in the u vs t time trace for this run. Figure 17B is a three dimensional look at the same bursting which helps visualize the cycles in a u, w vs t plot. In Figure 17C we see the projection of this trajectory onto the (x, y)-plane. The projected trajectory begins in the upper left corner and clearly illustrates the attraction toward the line $y = \frac{\beta_2}{\beta_1}x + \beta_2(\alpha_1 - \alpha_2)$, indicated as $p = 1$. Also superimposed in Figure 17C are the two curves Γ_- and Γ_{HC}, indicated as $x + \gamma y = z_-$ and $x + \gamma y = z_{\text{HC}}$, respectively.

In the degenerate case we may compute the functions $\widehat{\phi}$, $\widetilde{\phi}$ and then the composition $\phi = \widehat{\phi} \circ \widetilde{\phi}$.

Construction of $\widetilde{\phi}$ in the degenerate case

In this section we will construct $\widetilde{\Phi}$ where, according to Figure 18,

$$\mathbf{X}_{n+1} = \widetilde{\Phi} \begin{pmatrix} x_n \\ y_n \end{pmatrix} = \begin{pmatrix} \widetilde{\phi}(x_n) \\ \frac{z_- - \widetilde{\phi}(x_n)}{\gamma} \end{pmatrix}. \tag{3.27}$$

In terms of the transformation variables (z, p), introduced in (3.12), the slow subsystem is:

$$z = f(u) - g(u) \equiv G(u) \ , \tag{3.28}$$

$$\frac{dz}{d\tau} = \frac{H(u) - z}{\tau_1} \ , \tag{3.29}$$

$$\frac{dp}{d\tau} = \frac{1 - p}{\tau_1} \ , \tag{3.30}$$

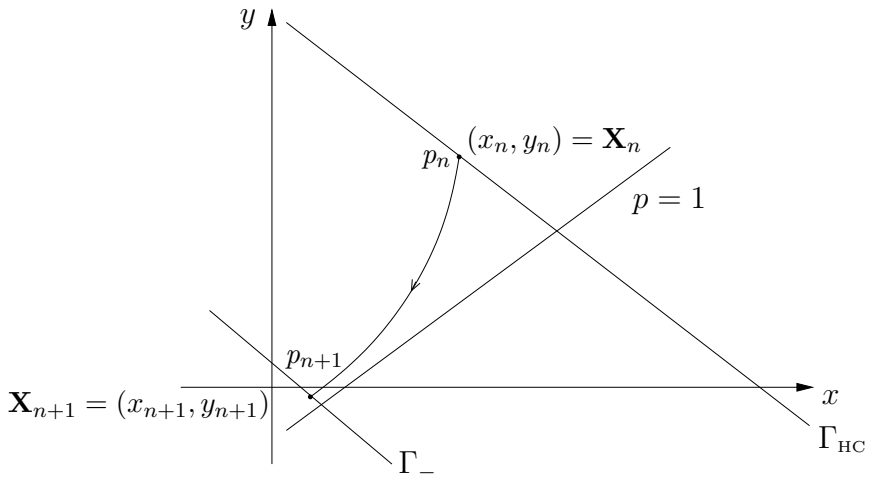


Figure 18: Projected trajectories on S_L associated with the singular map in the degenerate $\tau_1 = \tau_2$ case.

where

$$H(u) = \beta^*(u - \alpha^*) \ , \tag{3.31}$$

$$\beta^* = \beta_1 + \gamma\beta_2 \ , \tag{3.32}$$

$$\alpha^* = \frac{\beta_1\alpha_1 + \gamma\beta_2\alpha_2}{\beta_1 + \gamma\beta_2} \ . \tag{3.33}$$

The transformation variable p was defined in (3.12) as

$$p = x - \frac{\beta_1\tau_2}{\beta_2\tau_1}y + \beta_1(\alpha_1 - \alpha_2) + 1,$$

which simplifies in the degenerate case to

$$p = x - \frac{\beta_1}{\beta_2}y + \beta_1(\alpha_1 - \alpha_2) + 1.$$

Notice that for fixed p we may plot these curves as lines in the (x, y)-plane. We have the $p = 1$ line plotted in Figure 18, which is the line to which the projection of bursting solutions converge. We have also indicated the coordinates p_n and p_{n+1} corresponding to $\mathbf{X}_n$ and $\mathbf{X}_{n+1}$, respectively.

In order to compute the silent phase duration T_s, we differentiate (3.28) and use (3.29),

$$\frac{dz}{d\tau} = G'(u)\frac{du}{d\tau} = \frac{H(u) - G(u)}{\tau_1}.$$

Integrating

$$\int_{u_{\mathrm{HC}}}^{u_-} \frac{G'(u)}{H(u) - G(u)}\, du = \int_0^{T_s} \frac{1}{\tau_1}\, d\tau,$$

and then solving for T_s,

$$T_s = \tau_1 \int_{u_{\mathrm{HC}}}^{u_-} \frac{G'(u)}{H(u) - G(u)}\, du. \tag{3.34}$$

We observe that T_s is the same constant in the definition of the domain $D(\widetilde{\phi})$ and an explicit formula is derivable in principle but not of practical value. However, with the computed value of T_s we now integrate (3.30)

$$\int_{p_n}^{p_{n+1}} \frac{1}{1-p}\, dp = \int_0^{T_s} \frac{1}{\tau_1}\, d\tau,$$

and find that

$$\ln\left|\frac{1-p_n}{1-p_{n+1}}\right| = \frac{T_s}{\tau_1}. \tag{3.35}$$

Referring to Figure 18 and using the previously shown global attraction, we see that if $p_n > 1$ then $p_{n+1} > 1$. Similarly, if $p_n < 1$ then $p_{n+1} < 1$. This allows us to drop the absolute value:

$$\frac{1-p_n}{1-p_{n+1}} = e^{\frac{T_s}{\tau_1}},$$

and solve for p_{n+1}

$$p_{n+1} = 1 - (1-p_n)\, e^{\frac{-T_s}{\tau_1}}, \tag{3.36}$$

where

$$p_{n+1} = x_{n+1} - \frac{\beta_1}{\beta_2}\left(\frac{z_- - x_{n+1}}{\gamma}\right) + \beta_1(\alpha_1 - \alpha_2) + 1, \tag{3.37}$$

$$p_n = x_n - \frac{\beta_1}{\beta_2}\left(\frac{z_{\mathrm{HC}} - x_n}{\gamma}\right) + \beta_1(\alpha_1 - \alpha_2) + 1. \tag{3.38}$$

Using (3.37)-(3.38) in (3.36) we may solve for x_{n+1} to find $\widetilde{\phi}$ as:

$$x_{n+1} = \widetilde{\phi}(x_n) = e^{\frac{-T_s}{\tau_1}} x_n + b_s, \tag{3.39}$$

where

$$b_s = \frac{\left(1 - e^{\frac{-T_s}{\tau_1}}\right)\beta_1\beta_2\gamma(\alpha_2 - \alpha_1) + \beta_1\left(z_- - z_{\rm HC}e^{\frac{-T_s}{\tau_1}}\right)}{\beta_1 + \gamma\beta_2}. \tag{3.40}$$

We point out that $\widetilde{\Phi}$ is completely defined by:

$$x_{n+1} = \widetilde{\phi}(x_n), \tag{3.41}$$

$$y_{n+1} = \frac{z_- - \widetilde{\phi}(x_n)}{\gamma}. \tag{3.42}$$

Construction of $\widehat{\phi}$ in the degenerate case

In this section we will construct $\widehat{\Phi}$, in an analogous fashion to our construction of $\widetilde{\Phi}$ in the previous section, where, according to Figure 19,

$$\mathbf{X}_{n+1} = \widehat{\Phi}\begin{pmatrix} x_n \\ y_n \end{pmatrix} = \begin{pmatrix} \widehat{\phi}(x_n) \\ \frac{z_{\rm HC} - \widehat{\phi}(x_n)}{\gamma} \end{pmatrix}. \tag{3.43}$$

In terms of the variables (z, p), (FULL) can be written:

$$\frac{du}{dt} = f(u) - w - z\ , \tag{3.44}$$

$$\frac{dw}{dt} = g(u) - w\ , \tag{3.45}$$

$$\frac{dz}{dt} = \varepsilon\frac{H(u) - z}{\tau_1}\ , \tag{3.46}$$

$$\frac{dp}{dt} = \varepsilon\frac{1 - p}{\tau_1}\ , \tag{3.47}$$

where $H(u), \beta^*, \alpha^*$ are given in (3.31)-(3.33).

Averaging $H(u)$ over limit cycles $\Omega(t, z)$, we get

$$\langle H(u)\rangle = \frac{1}{T(z)}\int_0^{T(z)} \beta^*(\Omega(t, z) - \alpha^*)dt,$$

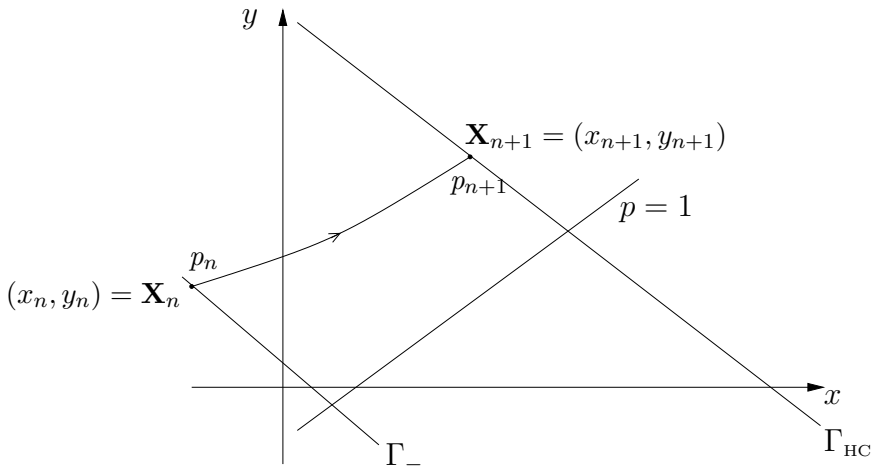


Figure 19: Projected active phase trajectories associated with the singular map in the degenerate $\tau_1 = \tau_2$ case.

where in (2.68) we defined

$$\hat{u}(z) \equiv \frac{1}{T(z)} \int_0^{T(z)} \Omega(\eta, z) d\eta \,.$$

Thus,

$$\widehat{H}(z) = \beta^*(\hat{u}(z) - \alpha^*).$$

We may now write the averaged fast subsystem associated with (3.44)-(3.47) as:

$$\frac{dz}{d\tau} = \frac{\langle H(u) \rangle - z}{\tau_1} = \frac{\widehat{H}(z) - z}{\tau_1}, \tag{3.48}$$

$$\frac{dp}{d\tau} = \frac{1-p}{\tau_1}, \tag{3.49}$$

where again $\tau = \varepsilon t$ is a slow time.

In order to compute the active phase duration T_A, we integrate (3.48) as follows:

$$\int_{z_{\rm HC}}^{z_-} \frac{dz}{\widehat{H}(z) - z} = \int_0^{T_A} \frac{1}{\tau_1} \, d\tau,$$

and then solve for T_A to find:

$$T_A = \tau_1 \int_{z_{\rm HC}}^{z_-} \frac{dz}{\widehat{H}(z) - z}. \tag{3.50}$$

We observe that T_A is the same constant needed to define $D(\widehat{\phi})$ and that an explicit formula is not possible. However, with the computed value of T_A we now integrate (3.49)

$$\int_{p_n}^{p_{n+1}} \frac{1}{1-p}\,dp = \int_0^{T_A} \frac{1}{\tau_1}\,d\tau,$$

We now proceed exactly as we did in (3.35)-(3.38) using the value of T_A from (3.50) to find:

$$x_{n+1} = \widehat{\phi}(x_n) = e^{\frac{-T_A}{\tau_1}} x_n + b_A, \tag{3.51}$$

where

$$b_A = \frac{\left(1 - e^{\frac{-T_A}{\tau_1}}\right)\beta_1\beta_2\gamma(\alpha_2 - \alpha_1) + \beta_1\left(z_- - z_{\text{HC}}e^{\frac{-T_A}{\tau_1}}\right)}{\beta_1 + \gamma\beta_2}. \tag{3.52}$$

We point out that $\widehat{\Phi}$ is completely defined by:

$$x_{n+1} = \widehat{\phi}(x_n), \tag{3.53}$$

$$y_{n+1} = \frac{z_- - \widehat{\phi}(x_n)}{\gamma}. \tag{3.54}$$

Construction of ϕ in the degenerate case

Summarizing the results of the previous two subsections, in the degenerate case,

$$\widetilde{\phi}(x) = e^{\frac{-T_s}{\tau_1}} x + b_s, \tag{3.55}$$

$$\widehat{\phi}(x) = e^{\frac{-T_A}{\tau_1}} x + b_A, \tag{3.56}$$

where b_s and b_A are as given in (3.40) and (3.52).

Note that both $\widetilde{\phi}$ and $\widehat{\phi}$ are linear. As such, the composition $\phi = \widetilde{\phi} \circ \widehat{\phi}$ will be linear as well. Composing (3.39) and (3.51) we get:

$$\phi(x) = e^{\frac{-(T_s+T_A)}{\tau_1}} x + b_{As}, \tag{3.57}$$

where

$$b_{As} = e^{\frac{-T_s}{\tau_1}} b_A + b_s. \tag{3.58}$$

We do not have an explicit formula for T_s and T_A but could numerically approximate the values in (3.34) and (3.50). Thus, in the degenerate case we can write down a linear formula for our return map and identify map fixed points as:

$$\bar{x} = \frac{b_{As}}{1 - e^{\frac{-(T_s+T_A)}{\tau_1}}}. \tag{3.59}$$

CHAPTER 4

NUMERICAL CONSTRUCTION OF THE RETURN MAP

Overview of Numerical Methods Used

In the various numerical methods utilized, we keep the (FS) parameters fixed and vary just the slow parameters ($\beta_i, \alpha_i, \tau_i;\ i = 1, 2$) and γ. The (FS) parameters are fixed to yield square-wave bursting, as per Pernarowski [42]. In Chapter 2 we simplified the problem of finding singular solutions of the four dimensional system (FULL), to the study of the two-dimensional systems (SS) and (AFS). Initially, Matlab was used to numerically compute ϕ by a shooting method. Later we were able to use the continuation and bifurcation software AUTO [18]. Due to the many advantages of using AUTO, delineated below, the majority of our numerical results refer to AUTO computations. The Matlab computations are offered primarily to corroborate our AUTO results.

Our first goal is to numerically approximate the maps $\widetilde{\phi}$ and $\widehat{\phi}$, for a range of slow parameters. Our next goal will then be to categorize properties of the maps resulting in bursting solutions via the activation/inactivation scheme outlined in Table 1. We will continue to use the notation z_{HC} and z_{-} as defined in (3.7)-(3.6) to refer to the $z = x + \gamma y$ coordinate of the homoclinic and limit point curves, respectively. Due to our earlier identification of fixed points of the map ϕ with singular bursting solutions, we are interested in approximating fixed points of the composition of the two numerically computed maps. We will summarize the results of our numerical computations with plots of initial x_0 against final x_f values for both the silent and active phases $\widetilde{\phi}$ and $\widehat{\phi}$, respectively.

In the various numerical simulations throughout this chapter two (SS) parame-

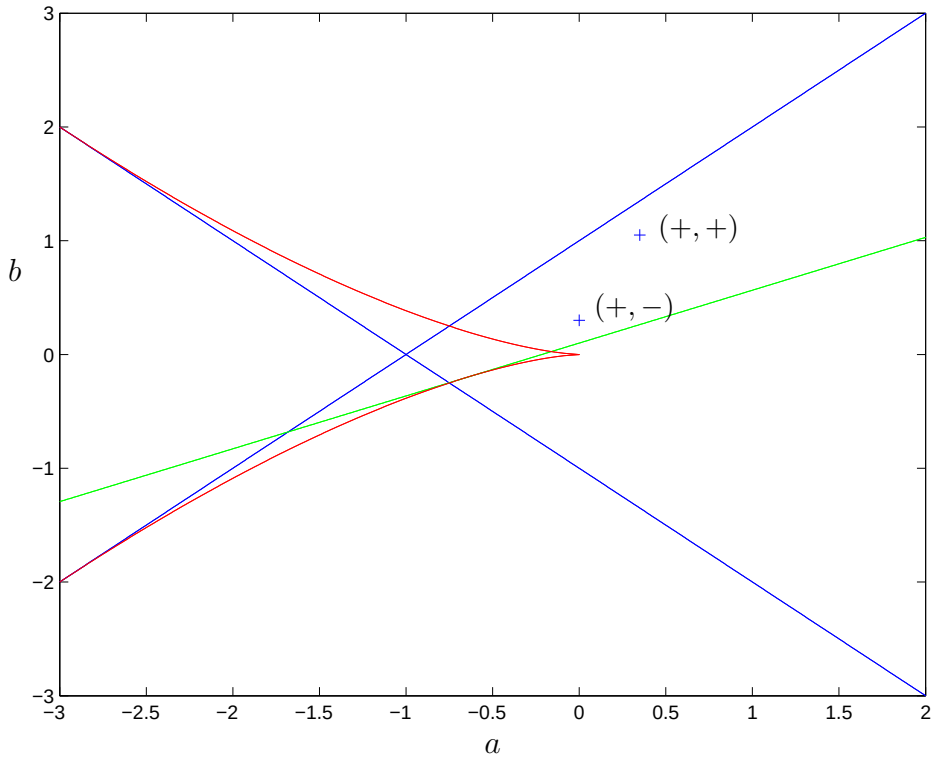


Figure 20: SS parameter diagram indicating the location of equilibria for the two parameter sets used throughout this chapter. Parameter values for $(+,+)$ and $(+,-)$ are tabulated in Table 3. The $(+,+)$ case corresponds to $(a,b) = (0.35, 1.05)$ and $(+,+)$ corresponds to $(a,b) = (0, 0.30)$ and that in both cases the sole equilibrium is on the middle branch $\mathcal{S}_M$.

ter sets have been selected to showcase and compare the numerical methods. These two parameter sets are shown in Table 3. In all of the numerical computations we used a value of $\varepsilon = 0.0025$, unless indicated otherwise. Note we have an 'activation/activation' and an 'activation/inactivation' example. We further point out that each of these two parameter sets have a sole equilibrium on $\mathcal{S}_M$ with $u_e < u_{\text{HC}}$ which guarantees bursting solutions of (FULL) in the degenerate case. The determination of equilibrium location was made using our SS parameter diagram, shown in Figure 20, where we reference the two (SS) parameter sets using the notation we will continue to use for the remainder of the chapter.

	β_1	α_1	β_2	α_2	γ	τ_1	τ_2
$(+,+)$	3	-1	0.5	-3	0.7	0.9	1
$(+,-)$	4	-1	-1	-0.7	1	1	0.3

Table 3: (SS) Parameter sets

Matlab

For our initial investigation of (FULL), in particular, the dependence of bursting solutions on the various parameters, we used a shooting method to compute $\widetilde{\phi}$ and $\widehat{\phi}$ where (FULL) was numerically integrated in Matlab.

As in our map construction, the (SS) numerical approximation was much more straight forward. In order to approximate $\widetilde{\phi}$, we first wrote Matlab code to numerically integrate (FULL) with initial conditions (x_0, y_0) on Γ_{HC} and $(u_0, w_0, x_0, y_0) \in \mathcal{S}_L$. Note that, since the slow manifold is the only stable object of (FS) for $(x, y) \in \Gamma_{\text{HC}}$ trajectories are attracted to $\mathcal{S}_L$ for $t \sim O(1)$. We allowed the trajectory of (FULL) to traverse the slow manifold and terminate on Γ_-. In order to numerically approximate the map $\widetilde{\phi}$, for the silent phase, our code ran over a range of initial x_0 values and the terminal points x_f on Γ_- were recorded.

In a similar fashion Matlab code was written for the active phase. In this case, trajectories projected onto the (x, y)-plane, were started at Γ_- and terminated at Γ_{HC}. The initial (u_0, w_0) values were chosen near the maximum value of u on the limit cycle associated with $z = x + \gamma y = z_{\text{LP}}$. Again, we numerically integrated (FULL) with $\varepsilon \ll 1$ for a range of initial x_0 values. Shown later in the chapter, in Figure 26, is a comparison of Matlab and AUTO results with the same parameter sets, plotted as x_f vs x_0.

There are many disadvantages of this particular Matlab code when compared with using AUTO. The runs are typically very slow, especially for the numerical construction of $\widehat{\phi}$. And we must rerun the simulation for every parameter change. The 'slowness' of runs was in large part due to our use of (FULL) to generate the two composite maps, necessitating the use of a very small value of ε. For these reasons we used the Matlab numerical constructions just for the purpose of verifying the results obtained with AUTO. However, this use of (FULL) by Matlab served as a verification of the numerical map constructions and the asymptotics in our (AFS) definition, since we did not use our (AFS) derivation from Chapter 2.

Auto

Our, by now familiar, caricature of the (SS) is shown in Figure 21. The map $\widetilde{\phi}$ for the slow flow on $\mathcal{S}_L$ is computed as a solution of the following boundary value problem

$$\begin{aligned}
\frac{dx}{d\tau} &= T\left(-(1-\lambda)x + \lambda F_1(x,y)\right) \ , && (4.1)\\
\frac{dy}{d\tau} &= T\left(-(1-\lambda)y + \lambda F_2(x,y)\right) \ , && (4.2)\\
x(0) &= x_0 \ , && (4.3)\\
y(0) &= (z_{\text{HC}} - x_0)/\gamma \ , && (4.4)\\
x(1) &= x_f \ , && (4.5)\\
y(1) &= (z_- - x_f)/\gamma, && (4.6)
\end{aligned}$$

where the vector field $\mathbf{F} = (F_1, F_2)$ is that of (SS) defined in (2.35)-(2.36). As before, we exploit the functional dependence $y = y(x)$ on the curves Γ_{HC} and Γ_- when defining the boundary conditions in y. In (4.1)-(4.6) we have included a homotopy parameter λ. When $\lambda = 1$ and $T = T_S$ then $x_f = \widetilde{\phi}(x_0)$, for $x_0 \in D(\widetilde{\phi})$.

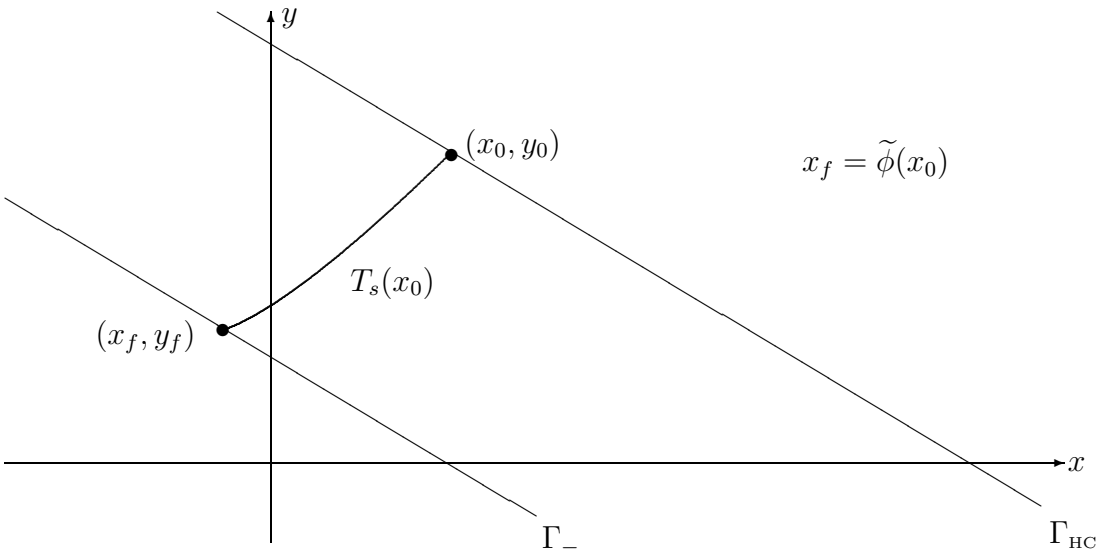


Figure 21: A caricature of $\widetilde{\phi}$ (SS), projected onto the (x, y)-plane.

We use AUTO to continue the solution of (4.1)-(4.6) from the $\lambda = 0$ case to the $\lambda = 1$. The constant T is the transit time in the variable τ, which AUTO requires to be scaled for crossing times of one. We start with a BVP with a known analytic solution. This is the $\lambda = 0$ case:

$$\frac{dx}{d\tau} = -Tx, \tag{4.7}$$

$$\frac{dy}{d\tau} = -Ty, \tag{4.8}$$

with the same boundary conditions as in (4.3)-(4.6), noting that $x_f = x_0 e^{-T}$ in (4.5). For this particular problem, the transit time is computed to be the constant $T = ln\left(\frac{z_{\text{HC}}}{z_-}\right)$ for all x_0. With this initial setup, we run AUTO to homotope from the $\lambda = 0$ known solution to the $\lambda = 1$ case. We allow the three parameters (λ, x_f, T) to vary in this run with x_0 fixed until $\lambda = 1$. At $\lambda = 1$, (4.1)-(4.2) reduces to the

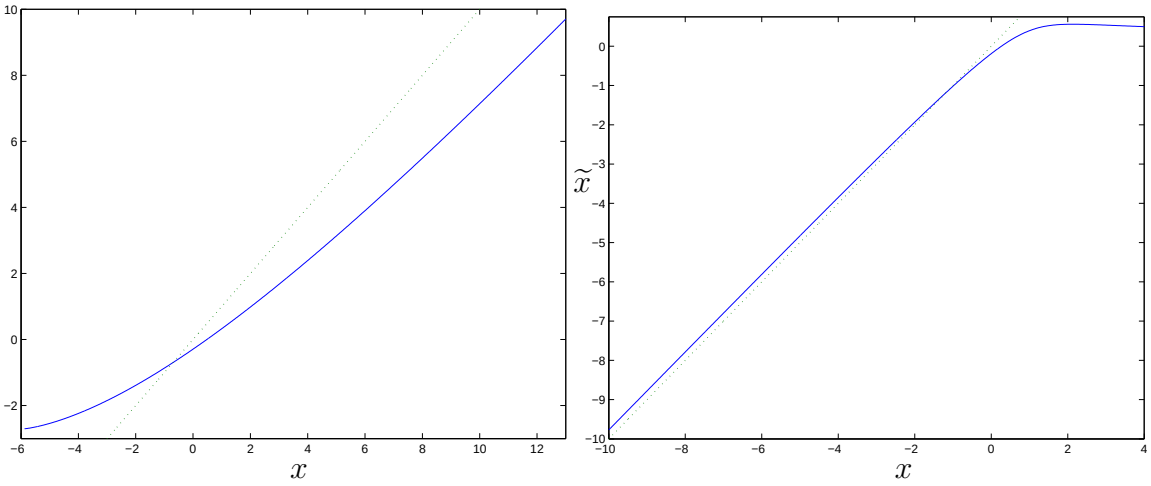


Figure 22: Map $\widetilde{\phi}(x)$ generated numerically using AUTO: the solid line shows $\widetilde{x} = \widetilde{\phi}(x)$ for a range of initial x values; $(+,+)$ case on left, $(+,-)$ case on right. The dotted line is $y = x$, added just for reference. Parameter values for each computation are tabulated in Table 3.

(SS):

$$\frac{dx}{d\tau} = TF_1(x,y) = T\left(\frac{\beta_1(u_{\rm LB}(x+\gamma y)-\alpha_1)-x}{\tau_1}\right), \tag{4.9}$$

$$\frac{dy}{d\tau} = TF_2(x,y) = T\left(\frac{\beta_2(u_{\rm LB}(x+\gamma y)-\alpha_2)-y}{\tau_2}\right), \tag{4.10}$$

where $u_{\rm LB}$, is the variable u restricted to the lower branch, where we use the trigonometric form of the root defined in (2.33).

In our next run, we resume from the point in our initial run where $\lambda = 1$. Throughout this second run we keep λ fixed and allow $(x_0,\ x_f,\ T)$ to vary. This amounts to running the BVP with a range of starting x_0 values. With our interest in fixed points of the map, we have generated graphs of x versus $\widetilde{x} = \widetilde{\phi}(x) = x_f$ in Figure 22. Superimposed on each of these graphs is the dotted line $y = x$, merely as a point of reference, keeping in mind that our interest is really in the fixed point of the composition ϕ.

Generating similar graphs for the slow flow in the (AFS) is more difficult, partly

because we are not able to select a u value from one of the three branches as we did for the (SS). Here one needs to know $\widehat{u}(z)$, that is, u averaged over the limit cycle $\Omega(t,z)$. But one can not simply write down a formula for $\widehat{u}(z)$. We used AUTO to generate $\widehat{u}$ versus z for $z \in (z_{\text{HB}}, z_{\text{HC}})$ for a large number of discrete points. We were then able to use the $\widehat{u}(z)$ relationship in the form of a data file in our BVP formulation, called as a subroutine interpolating its value at any z. More specifically, in our vector field when a $\widehat{u}(z)$ value was needed, the previously described data file was read and a $\widehat{u}$ value interpolated. In that the value of $\widehat{u}(z)$ does not depend on the (SS) parameters, the generation of the data defining $\widehat{u}(z)$ in this manner need only be performed once.

As we did for the (SS), we began our investigation of the (AFS) with a BVP with known analytic solution:

$$\frac{dx}{d\tau} = T\left(x(1-\lambda) + \lambda \widehat{G}_1(x,y)\right) , \tag{4.11}$$

$$\frac{dy}{d\tau} = T\left(\lambda \widehat{G}_2(x,y)\right) , \tag{4.12}$$

$$x(0) = x_0 , \tag{4.13}$$

$$y(0) = (z_- - x_0)/\gamma , \tag{4.14}$$

$$x(1) = x_f , \tag{4.15}$$

$$y(1) = (z_{\text{HC}} - x_f)/\gamma , \tag{4.16}$$

where the vector field $\widehat{\mathbf{G}} = (\widehat{G}_1, \widehat{G}_2)$ is that defined in (2.70)-(2.71). Again, T is the scaled transit time, and $\lambda = 0$ corresponds to the BVP with known analytic solution,

$$\frac{dx}{d\tau} = Tx, \tag{4.17}$$

$$\frac{dy}{d\tau} = 0, \tag{4.18}$$

with the same boundary conditions as in (4.13)-(4.16), noting that $x_f = x_0 e^{Tx}$ in (4.15). For this particular problem, the transit time is the constant $T = ln\left(\frac{z_{\rm HC} - z_- + x_0}{x_0}\right)$.

You may note that we have changed the $\lambda = 0$ BVP in (4.17)-(4.18) from that used in our (SS) runs (4.7)-(4.8). In choosing a BVP with known solution it was necessary to have a vector field with similar qualitative features in order for the homotopy in λ to work. The vector field used in the (SS) formulation would not work in the (AFS) since, in particular, x increases in the active phase (for the slow parameters chosen). We were more clever in this second attempt, and choose a simpler vector field that allowed us to cover the range of initial x_0 values in one AUTO run. We emphasize that the choice of the initial, $\lambda = 0$, vector field is not unique.

Continuing, we ran AUTO to homotope from the $\lambda = 0$ known solution to the $\lambda = 1$ case. We then allowed the three parameters (λ, x_f, T) to vary in this run, with x_0 fixed. The slow flow in the (AFS) corresponds to the $\lambda = 1$ case:

$$\frac{dx}{d\tau} = T\widehat{G}_1(x,y) = T\left(\frac{\beta_1(\widehat{u}(x+\gamma y) - \alpha_1) - x}{\tau_1}\right), \tag{4.19}$$

$$\frac{dy}{d\tau} = T\widehat{G}_2(x,y) = T\left(\frac{\beta_2(\widehat{u}(x+\gamma y) - \alpha_2) - y}{\tau_2}\right). \tag{4.20}$$

As before, in our second run we continue from the $\lambda = 1$ point, keeping λ fixed and allowing (x_0, x_f, T) to vary. It is in this run that we make use of the $\widehat{u}(z)$ data file generated previously.

One drawback of computing $\widehat{u}(z)$ from the data file format is the numerous file reads required in a single AUTO run. In order to greatly speed up our runs we decided to fit a function to the $\widehat{u}(z)$ data. We first tried to fit a polynomial to the data. But even up through an eleventh degree polynomial, the fit was not very good.

Recognizing that the plotted data, shown as *'s in Figure 23, had the form of a

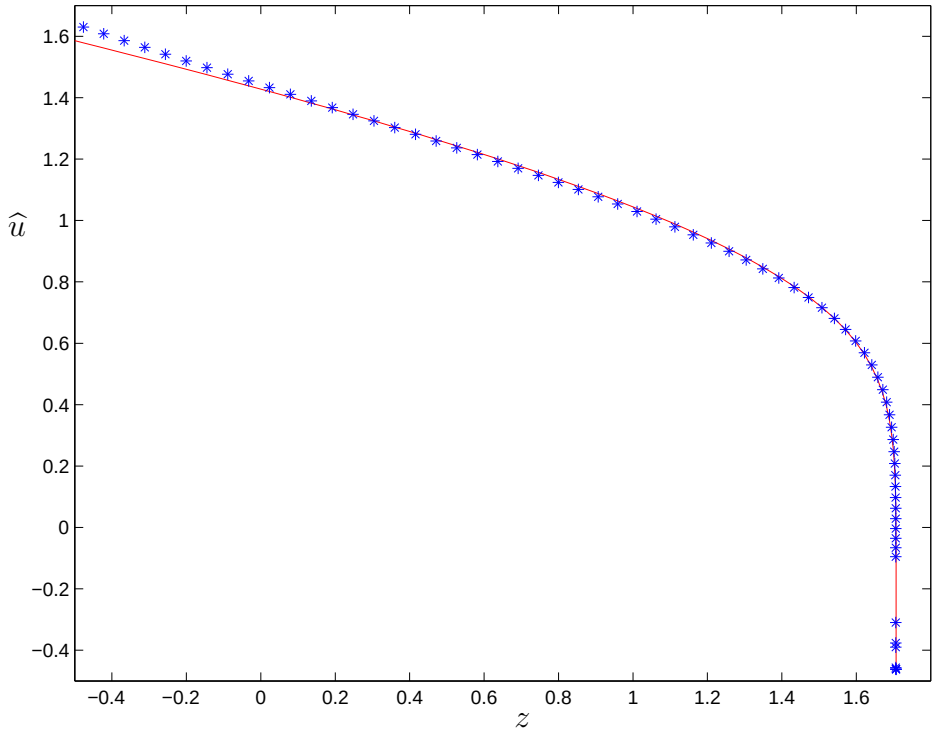


Figure 23: $\widehat{u}(z)$ plotted as AUTO generated data along with our fitted function. $\widehat{u}(z)$ is u averaged over the limit cycles $\Omega(t,z)$. The AUTO generated data is plotted as *'s, the superimposed curve is the function $\widehat{u}(z) = u_{\text{HC}} + \left(\frac{z_{\text{HC}}-z}{0.077}\right)^{\frac{1}{8}} + 0.26(z_{\text{HC}} - z)$ we fit to the data.

square root function we were able to nicely fit the following function to the data:

$$\widehat{u}(z) = u_{\text{HC}} + \left(\frac{z_{\text{HC}} - z}{0.077}\right)^{\frac{1}{8}} + 0.26(z_{\text{HC}} - z), \tag{4.21}$$

where we are using the following approximate values, $u_{\text{HC}} = -0.46466$ and $z_{\text{HC}} = 1.70633$. Our fit function in (4.21) is plotted as the solid line, along with the data, in Figure 23. The $\widehat{u}(z)$ data was generated for $z \in (z_{\text{HB}}, z_{\text{HC}})$, but for our purposes we are primarily interested in the region $z \in (1, z_{\text{HC}})$; the region of bistability. To better understand this figure, if we were to superimpose the plotted $\widehat{u}(z)$ data on a (FS) bifurcation diagram (such as Figure 4), the curve would begin at $(z,u) = (z_{\text{HB}}, u_{\text{HB}})$ and terminate at the point $(z,u) = (z_{\text{HC}}, u_{\text{HC}})$.

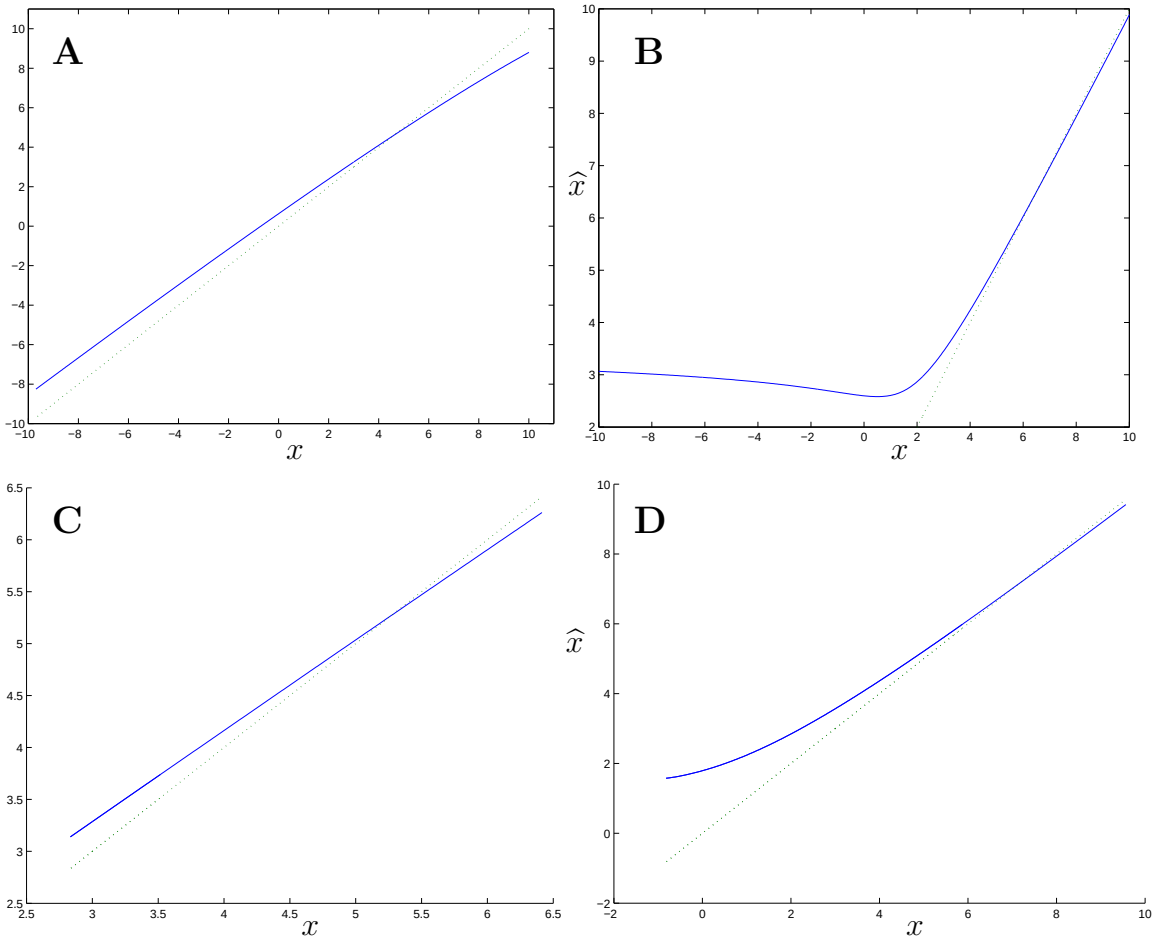


Figure 24: Map $\widehat{\phi}(x)$ generated numerically using AUTO: shows $\widehat{x} = \widehat{\phi}(x)$ for a range of initial x values. The two figures on the left are the $(+,+)$ case; the difference being that in **A** the $\widehat{u}(z)$ values were computed using the function in (4.21), whereas, in **C** $\widehat{u}(z)$ values were interpolated using the data file. The two figures on the right illustrate the $(+,-)$ case, in a similar fashion, with **B** generated using (4.21) and **D** using the interpolated data. We present **C** and **D** for comparison purposes. Parameter values for each computation are tabulated in Table 3.

Using (4.21) to approximate $\widehat{u}(z)$, we were then able to replace the slow data file read/interpolation technique with a function evaluation in subsequent AUTO runs. This greatly decreased the run times and for several comparison test runs our results were indistinguishable. In the next section to further substantiate this claim, we

superimpose trajectories of (FULL) with our fit function $\widehat{u}(z)$ in Figure 28 and 29.

For the same two parameter sets used in Figure 22, and in a similar fashion we generated numerical results for the (AFS), graphs of x versus $\widehat{x} = \widehat{\phi}(x)$ are shown in Figure 24. Furthermore, for each of these parameter sets we generated two figures, one figure was generated using computed $\widehat{u}(z)$ values from the function in (4.21) and the other used the file read feature of AUTO and interpolated the $\widehat{u}(z)$ values from the data file. We present both figures together for the purpose of comparison of the two methods. The generation of data using the fit function in (4.21) as opposed to the aforementioned file read/interpolation was faster by an order of about one thousand.

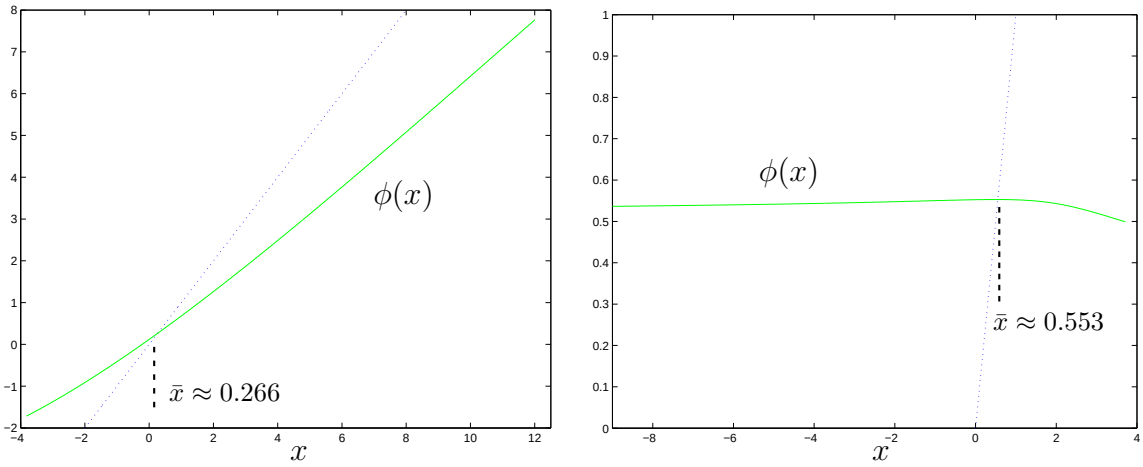


Figure 25: The composition $\phi = \widetilde{\phi}(\widehat{\phi}(x))$ represented here as the composition of the data that generated Figures 22 and 24. The figure on the left is the $(+,+)$ case, and the right is the $(+,-)$ case. Parameter values for each computation are tabulated in Table 3.

In Figures 22 and 24 we have shown some numerically generated representations of $\widetilde{\phi}(x)$ and $\widehat{\phi}(x)$, respectively. But for our needs what is really important is the composition of these two maps, recall that ϕ is the composition $\phi = \widetilde{\phi} \circ \widehat{\phi}$. As such, a fixed point $\bar{x}$ of $\phi(x)$ could be illustrated as the intersection of this composition

with the $y = x$ line. In Figure 25 we have generated the composition by composing the data which generated the figures shown in Figures 22, 24. In each figure we see $\phi(x_0) = \widetilde{\phi}(\widehat{\phi}(x_0))$ for a range of initial x values x_0.

Superimposed in each figure is the $y = x$ line, indicating fixed points of $\bar{x} \approx 0.266$ and $\bar{x} \approx 0.553$ for the $(+,+)$ and $(+,-)$ cases, respectively. Verification of these values is given in the next section.

Evaluation of the numerical methods

Thus far in the chapter all the numerical results and the associated figures have been generated using AUTO. As a first step toward verifying these results we compare the results obtained using Matlab to those obtained using AUTO in Figure 26 in the computation of $\widehat{\phi}$. We choose to show the comparison of the results for $\widehat{\phi}$ because this was the more difficult numerical simulation for both Matlab and AUTO. Since we have previously shown the consistency in the generation of $\widehat{\phi}$ regardless of the form of $\widehat{u}$, our AUTO results in Figure 26 are using (4.21).

In Figure 26A we compare the numerical results obtained in the $(+,+)$ case, with the Matlab results indicated by the 'x' marks. In Figure 26B we make the same comparison but in the $(+,-)$ case. As the figures show, the Matlab results corroborate the results we obtained using the BVP method in AUTO. In a similar fashion, for several other different (SS) parameter sets the two methods continued to reinforce each other (not shown here).

Another way of verifying the numerical results of the previous section is the verification of the fixed points $\bar{x}$ so obtained. We used xppaut to numerically integrate (FULL) and produce the figures shown in Figure 27. Shown on the left are two trajectories of (FULL) projected onto the (x, y)-plane for the $(+,+)$ case.

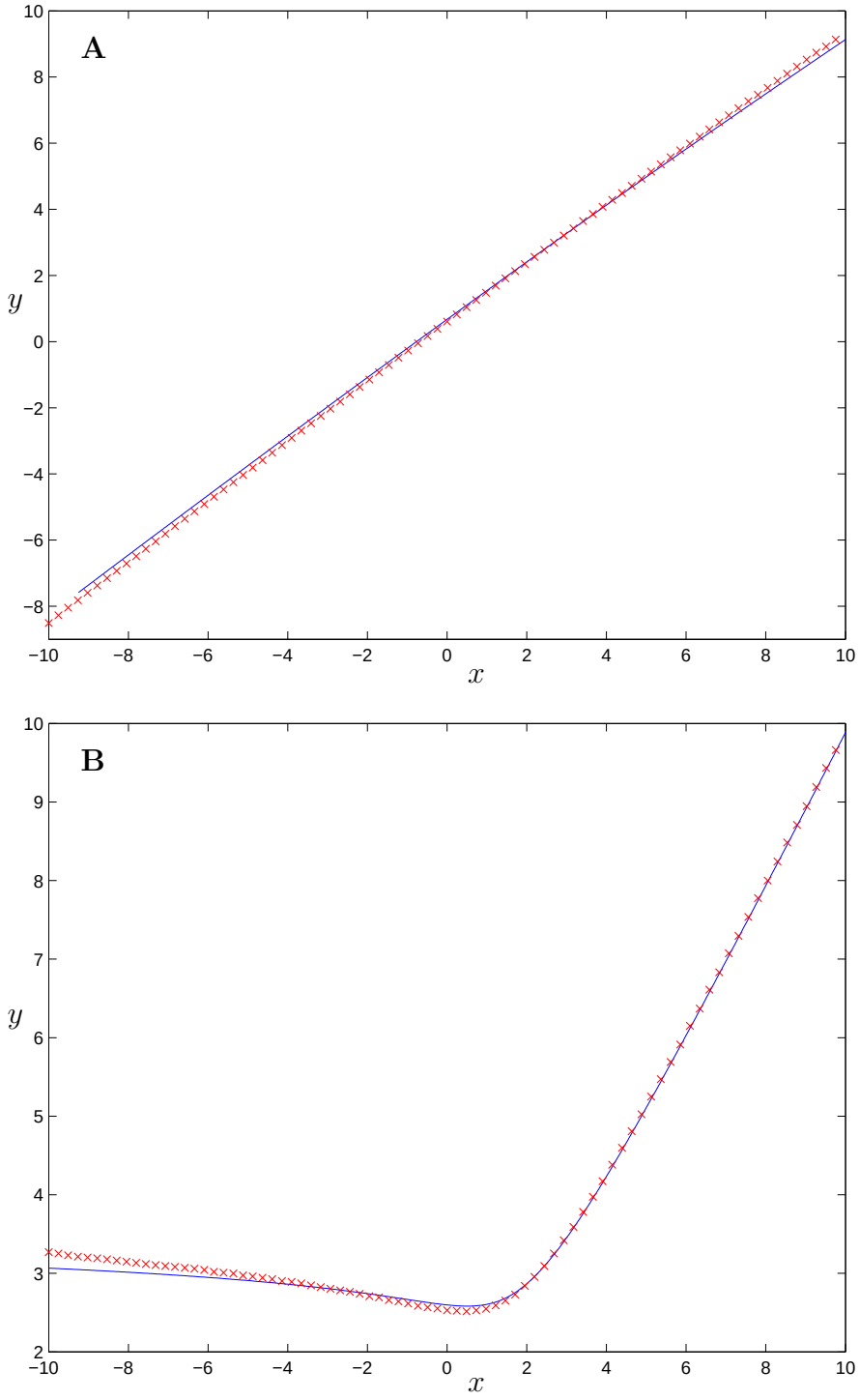


Figure 26: Comparison of the numerical computations of $\widehat{\phi}(x)$. In both figures we compare the numerical results obtained with AUTO to those obtained using Matlab (shown as the 'x' marks). Figure **A** compares the $(+,+)$ results, whereas, **B** compares the $(+,-)$ results. Parameter values for each computation are tabulated in Table 3.

As can be seen in Figure 27A the projected trajectories appear to converge toward the superimposed line and generally appear to remain between Γ_- and Γ_{HC}. In Figure 27C we have enlarged the region of interest to better show the map fixed point of $\bar{x} \approx 0.266$. The value of $\bar{x}$ was obtained from the xppaut data file for the run and was selected from the file when $u = u_- = -1$. We see good agreement between the xppaut and AUTO values for the fixed point. More as a curiosity, since this case is "nearly degenerate", we have added the $p = 1$ line. Using (3.26) we compute the approximate value of the fixed point at $\bar{x} \approx 0.269$, which give good agreement with the value we obtained above.

As a verification of the map fixed points in the $(+,-)$ case we have similar xppaut generated figures on the right in Figure 27 . We note immediately that projected trajectories do not remain between Γ_- and Γ_{HC}. And furthermore, we do not see the attraction of projected trajectories toward the $p = 1$ line as we did in the "nearly degenerate" $(+,+)$ case, but rather we see the two projected trajectories winding onto a cycle in the (x, y)-plane. Finally, in Figure 27D we have enlarged the region containing the fixed point $\bar{x} \approx 0.553$, which verifies our previous results.

Lastly, we conclude the chapter with a numerical verification of how well (AFS) approximates (FULL) in the active phase. In Figure 28, an active phase trajectory of (FULL) projected onto the (x, y)-plane is shown together with a solution of (AFS) with the same initial conditions (here we used $\widehat{u}(z)$ as in (4.21)). The numerical integration shown is the $(+,-)$ case but with $\tau_1 = 2$. The figure on the right in Figure 28 is an enlargement of the region near the homoclinic bifurcation, just prior to the jump to the silent phase. Notice how well (AFS) using (4.21) approximates solutions of (FULL). We numerically generated these figures using the same value of $\varepsilon = 0.0025$ as we did in our other simulations. Figure 29 offers another comparison of (AFS) and (FULL) where we have considered reducing the value of ε.

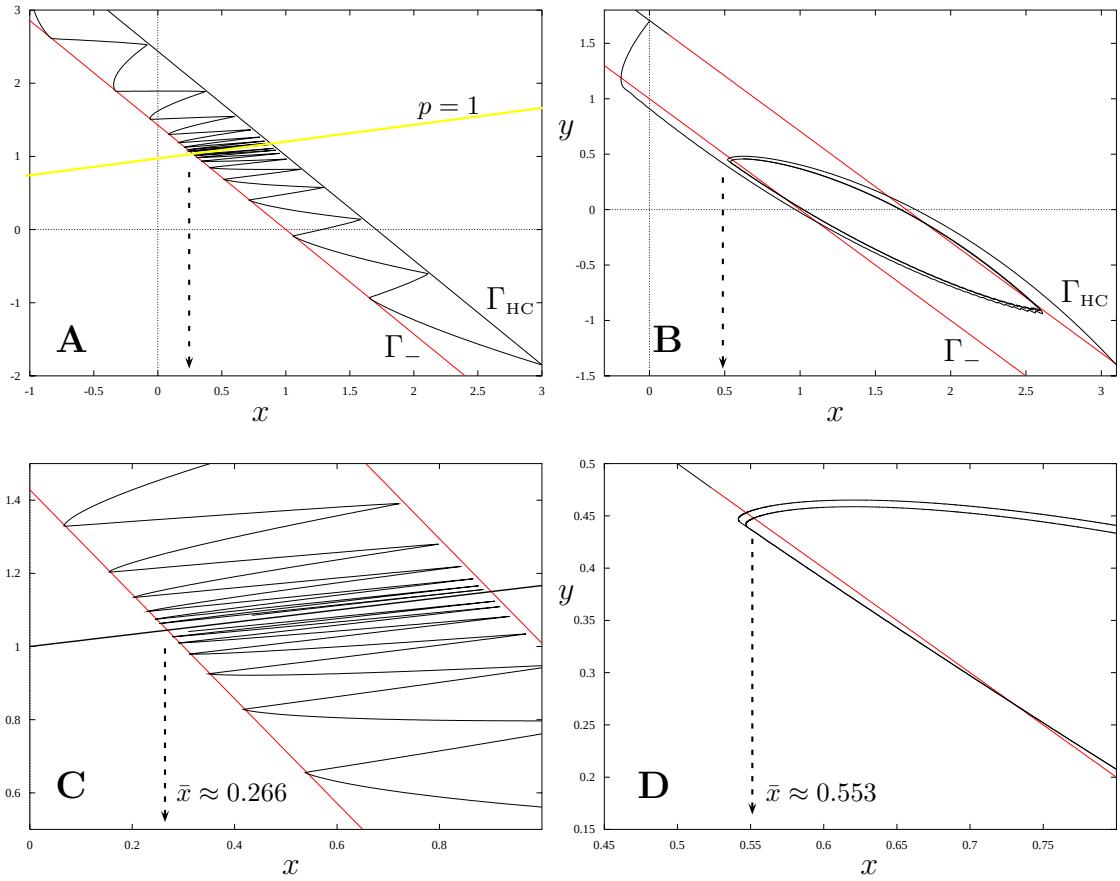


Figure 27: Verification of the fixed point $\bar{x} = \phi(\bar{x})$ obtained in the map composition, illustrated in Figure 25. The two figures on the left are the $(+,+)$ case and the two on the right are the $(+,-)$ case. In **A** we see the projection of two trajectories of (FULL) onto the (x,y)-plane appearing to converge toward the superimposed line $p = 1$. In **C** we have enlarged the region of interest, about the map fixed point $\bar{x} \approx 0.266$. Also shown in both of these figures are the curves Γ_- and $\Gamma_{\rm HC}$. In **B** we also see the projection of two trajectories of (FULL) onto the (x,y)-plane but in the $(+,-)$ case. The two projected trajectories wind onto a cycle in the (x,y)-plane. In **D** we are able to discern the map fixed point of $\bar{x} \approx 0.553$.

We wish to emphasize that the results presented in this chapter (along with other parameter sets) were numerically verified using Matlab. In the next chapter, in our discussion of domain and range issues, we will offer further examples using the AUTO construction of the map.

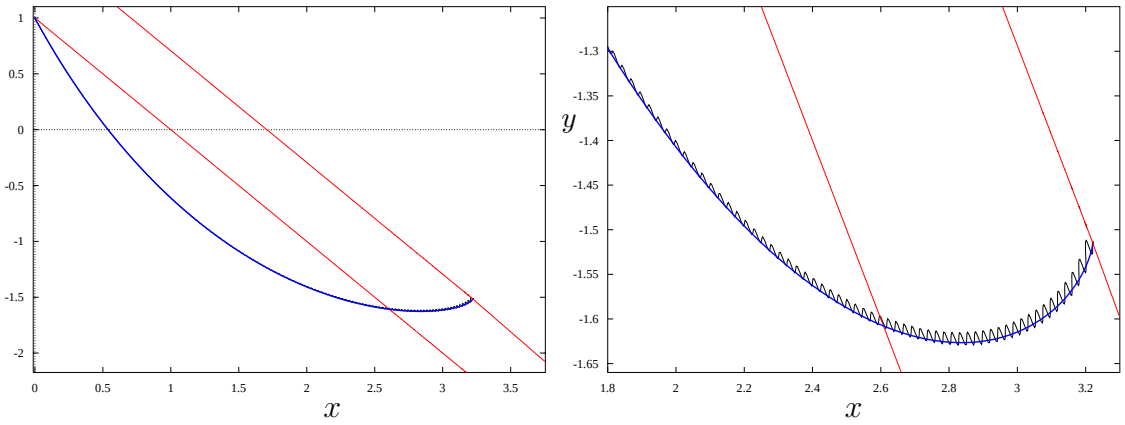


Figure 28: Both figures show an active phase trajectory of (FULL) projected onto the (x, y)-plane along with the (AFS) approximation using (4.21) and a typical value $\varepsilon = 0.0025$. The figure on the left shows the entire active phase and on the right we have enlarged the region near the jump to the silent phase (at the homoclinic bifurcation). The oscillating trajectory is (FULL) and the smooth curve is the (AFS). The parameter values used to generate these figures are those for the $(+,-)$ case listed in Table 3, but with $\tau_1 = 2$.

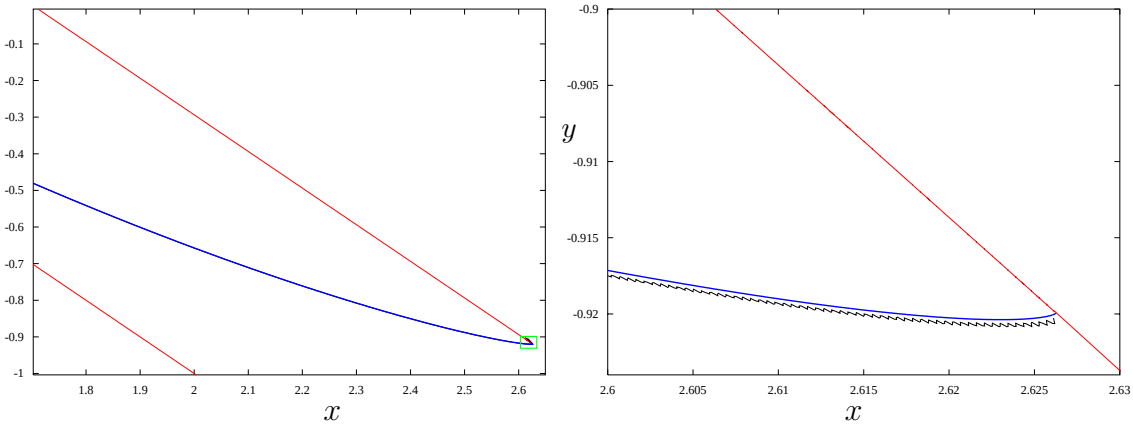


Figure 29: Another (AFS)-(FULL) comparison, to illustrate using a smaller ε value. Both figures show an active phase trajectory of (FULL) projected onto the (x, y)-plane along with the (AFS) approximation using (4.21) and the $(+,-)$ parameter set. The figure on the left ($\varepsilon = 2.5e$-4) shows a small portion of the trajectory near Γ_{HC}. The small rectangle in the lower right corner indicates the region we enlarge in the figure on the right ($\varepsilon = 2.5e$-5). The oscillating trajectory is (FULL) and the smooth curve is the (AFS).

CHAPTER 5

ISSUES AND APPLICATION OF THE RETURN MAP

Several important factors relating to our return map construction and the use of the map to establish the existence of a fixed point have been neglected in our development thus far. We will address those omissions here. Also, in Chapter 3 we investigated the special case where the time constants τ_1 and τ_2 were equal (the degenerate case), and presented some modest numerical results in the case that the time constants were similar in value. We will no longer consider special cases, but allow the parameters to vary over their respective ranges. The removal of these restrictions allows many additional qualitative features for the solutions of the model. One such feature not possible with our model in the degenerate case, is bistability between stable bursting solutions and a stable equilibrium. This will be discussed in a later section after some preliminary development.

We begin this chapter briefly revisiting our return map definition and looking at a possible alternate definition. Next we examine the issues and some of the complications involved in determining the domain and range of our map composite functions. As a part of this examination we determine the domain and range of both $\widetilde{\phi}$ and $\widehat{\phi}$ in the $(+,-)$ case. This discussion leads us directly to an examination of a bistability example. We close the chapter looking at a few interesting examples, one of which is the aforementioned bistability, and describe how we utilized some of the tools we developed in earlier chapters. We also examine the numerical map construction for these examples.

Lastly, in this chapter we will continue to refer to points in the (x, y)-plane, such as in Figure 30, by just the x coordinate for notational simplicity. The y coordinate is just $y = \frac{z_- - x}{\gamma}$ on the line Γ_- or $y = \frac{z_{\text{HC}} - x}{\gamma}$ for y on Γ_{HC}.

Map composition issues

In Chapter 3 we defined the map ϕ as the composition $\phi = \widetilde{\phi} \circ \widehat{\phi}$; in this section we look at an alternate definition $\phi_a = \widehat{\phi} \circ \widetilde{\phi}$ (here the order of $\widetilde{\phi}$ and $\widehat{\phi}$ have been interchanged). A bursting cycle of (FULL) projected onto the (x, y)-plane is shown in Figure 30 to illustrate the relationship between the map ϕ and the alternative map definition ϕ_a.

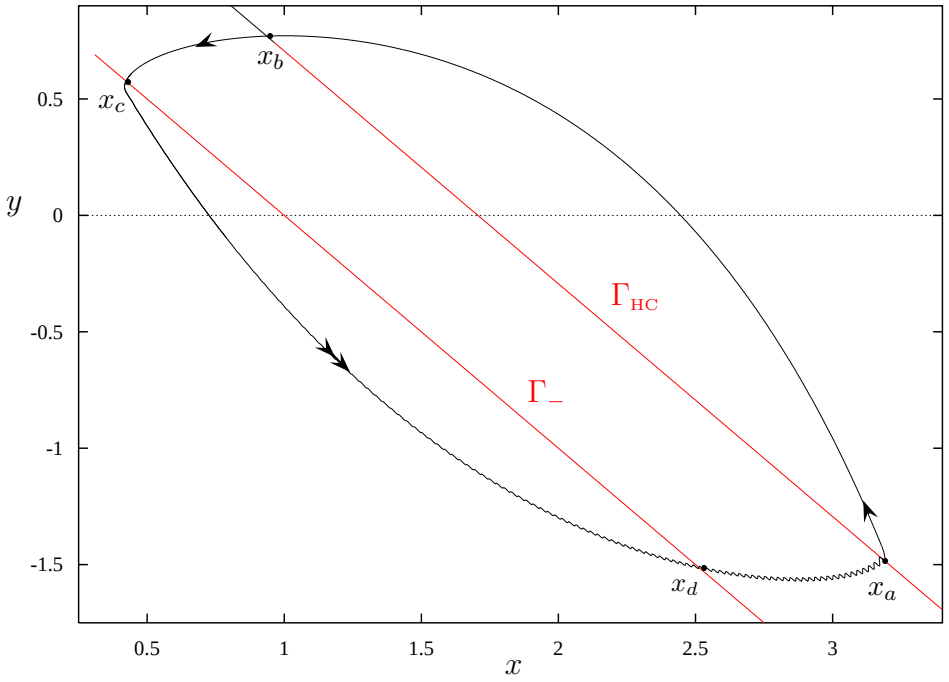


Figure 30: A bursting cycle of (FULL) projected onto the (x, y)-plane illustrating an alternate definition of the map ϕ: $\phi_a = \widehat{\phi} \circ \widetilde{\phi}$. Here $\widetilde{\phi}$ would map x_a to the point x_c as indicated by the single arrows on the trajectory. In turn $\widehat{\phi}$ would map x_c back to x_a as indicated by the double arrows. We remark that even though x_b is on the bursting cycle, specifically on Γ_{HC}, it is not a fixed point of the map ϕ_a since $x_b \neq \widehat{\phi}\left(\widetilde{\phi}(x_b)\right)$.

To describe the alternate map $\phi_a = \widehat{\phi} \circ \widetilde{\phi}$, consider the point marked x_a on Γ_{HC}. Note that $\widetilde{\phi}$ would map x_a to the point x_c on Γ_- as indicated by the single arrow on the trajectory. In turn $\widehat{\phi}$ would map x_c back to x_a, indicated by the double arrows. Thus x_a is a fixed point for this map, corresponding to a singular bursting solution of (FULL).

We describe the preceding example to show that we could have defined our map ϕ using this alternate definition. With the definition of ϕ in Chapter 3, $\bar{x} = x_c = \phi(x_c)$. Furthermore, any fixed points $\bar{x}$ of ϕ may be transformed to fixed points of the alternate map ϕ_a. In the example illustrated, the fixed point $\bar{x} = x_c$ of ϕ is related to the fixed point x_a of ϕ_a via $x_a = \widehat{\phi}(\bar{x})$.

Some caution must be exercised when working with figures such as Figure 30 and determining a fixed point for the bursting solution shown. For example, we illustrate that x_b is not a fixed point of ϕ_a. Given the alternate definition ϕ_a, $\widetilde{\phi}$ would map x_b to the point marked x_c (the x value as the trajectory exits the silent phase crossing Γ_-), and then $\widehat{\phi}$ would map x_c to the point x_a as $x_a = \widehat{\phi}\left(\widetilde{\phi}(x_b)\right)$. However, $x_b \neq \widehat{\phi}\left(\widetilde{\phi}(x_b)\right)$ so x_b is not a fixed point of ϕ_a, even though we are on a bursting cycle. And in a similar fashion x_d is not a fixed point of ϕ, though it is on the bursting cycle and on the curve Γ_-.

Domain issues

One of the issues we wish to address is when does there exist a fixed point $\bar{x} \in D(\phi)$. One way to prove the existence of a fixed point, which guarantees a bursting solution, is the use of one of the many fixed point theorems. The following standard theorem [21], [62] could be used to prove that ϕ has a unique fixed point on a closed interval $M \subset D(\phi)$.

THEOREM 5.1 (CONTRACTION MAPPING PRINCIPLE OF BANACH-CACCIOPOLI). *Let $\phi : D(\phi) \to \mathbb{R}$ and assume that there exists $M \subset D(\phi)$ which is closed and nonempty such that*

(i) $\phi : M \to M$ *; and*

(ii) ϕ *is k-contractive, ie, there exists* $k \in [0, 1)$ *such that*
$\|\phi(x) - \phi(y)\| \leq k\|x - y\|$ *for all* $x, y \in M$.

Then the following are true:

(a) Existence and uniqueness. The function ϕ has exactly one fixed point $\bar{x} \in M$.

(b) Convergence of the iteration method. For each $x_0 \in M$, the sequence $\{x_n\}_{n=1}^{\infty}$ constructed by $x_{n+1} = \phi(x_n)$ converges to the unique fixed point $\bar{x}$.

The use of such a theorem requires identifying a closed set $M \subset D(\phi)$, on which ϕ is into M, and then showing that the map ϕ is k-contractive. Toward that goal, we need some way of estimating the domains $D(\widehat{\phi})$, $D(\widetilde{\phi})$ and the ranges $R(\widehat{\phi})$, $R(\widetilde{\phi})$. The determination of these sets all require global information/dynamics of (SS)/(AFS) in most cases. This can be a difficult process which we will discuss below.

In discussing domain and range issues we will only consider the cases where at most one equilibrium occurs on $\mathcal{S}_L$. Specifically, we first carefully examine the $(+,-)$ case, where there is no equilibrium on $\mathcal{S}_L$. We then go on to discuss other cases where one fixed point, either stable or unstable, is on $\mathcal{S}_L$.

No Equilibrium on $\mathcal{S}_L$

We begin with the $(+,-)$ case, with parameter values as tabulated in Table 3 on page 75. It is also important to note that neither (SS) and (AFS) have equilibria

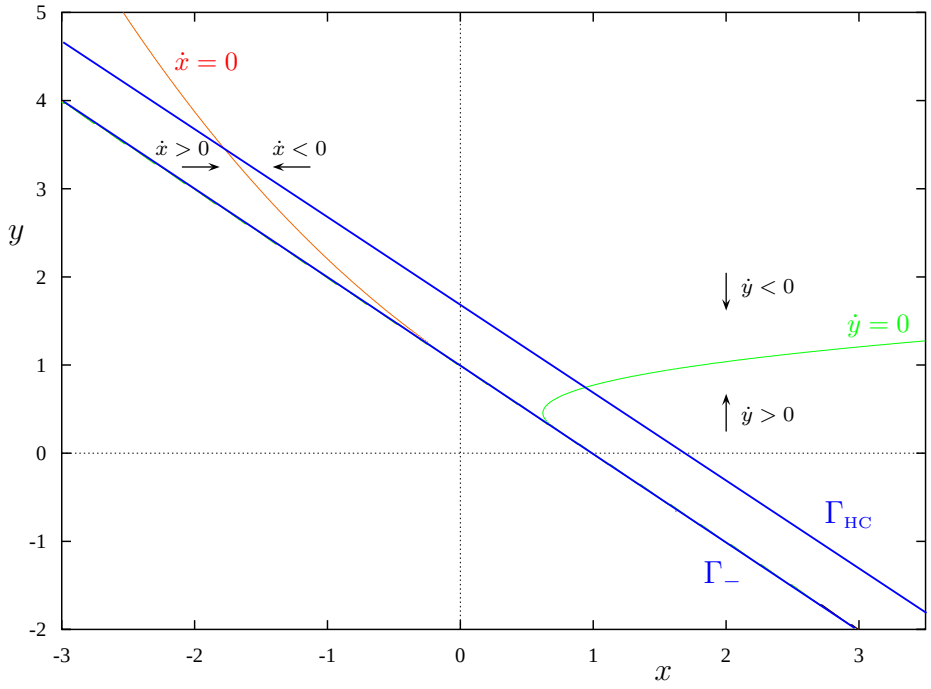


Figure 31: The x and y nullclines of the (SS), in the $(+,-)$ case. We also indicate the regions in which x and y are increasing/decreasing. Trajectories which start on Γ_{HC} must eventually terminate on Γ_-.

(and hence periodic orbits) and both are planar flows. We can get some idea of the domain and range of $\widetilde{\phi}$ and $\widehat{\phi}$ by looking at the nullclines of (SS) and (AFS), respectively.

Figure 31 shows the x and y nullclines for (SS) along with Γ_- and Γ_{HC}. Recall that for x_0 to be in the domain of $\widetilde{\phi}$, a (SS) trajectory originating on Γ_{HC} at $x = x_0$ must reach Γ_- in finite time. From the relative location of the x and y nullclines it is clear that, in this particular case, the domain of $\widetilde{\phi}$, in terms of x, is $D(\widetilde{\phi}) = \mathbb{R}$. However, it is not clear what is the range of $\widetilde{\phi}$.

At this point, we would like to describe a process that is useful for the determination of the range of $\widehat{\phi}$ and $\widetilde{\phi}$ and allow better intuition of the qualitative features of trajectories.

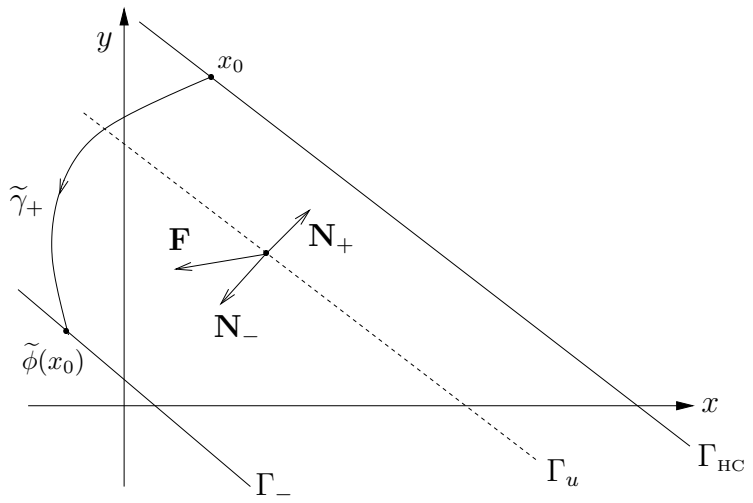


Figure 32: The normal vectors $\mathbf{N}_-$ and $\mathbf{N}_+$, orthogonal to an arbitrary Γ_u. We use these vectors in the computations of $\mathbf{F}\cdot\mathbf{N}_-$, and $\mathbf{G}\cdot\mathbf{N}_+$, respectively. Here $\mathbf{F}$ is the (SS) vector field, as in (5.1)-(5.2) and $\mathbf{G}$ is the (AFS) vector field in (5.12)-(5.13) (not illustrated above).

In Figure 32 an arbitrary Γ_u on $\mathcal{S}_L$ is shown, where Γ_u is the line $y = \frac{z-x}{\gamma}$ for fixed $z > z_-$. On each Γ_u there is a one to one correspondence between z and u (on $\mathcal{S}_L$), which allows us to use the notation Γ_u or Γ_z interchangeably. We have also indicated normal vectors $\mathbf{N}_- = (-1, -\gamma)$ and $\mathbf{N}_+ = (1, \gamma)$, along with our (SS) vector field $\mathbf{F} = (F_1, F_2)$ as defined in (2.35)-(2.36):

$$\frac{dx}{dt} = F_1(x,y) \equiv \frac{h_1(u) - x}{\tau_1}, \tag{5.1}$$

$$\frac{dy}{dt} = F_2(x,y) \equiv \frac{h_2(u) - y}{\tau_2}, \tag{5.2}$$

$$z = G(u) \equiv -u^3 + 3(u+1), \tag{5.3}$$

where as before u is restricted to $\mathcal{S}_L$ ($u < u_-$). The condition that (SS) trajectories cross an arbitrary Γ_u in the direction toward Γ_- is equivalent to the condition:

$$\vec{\mathbf{F}} \cdot \vec{\mathbf{N}}_- \big|_{\Gamma_u} > 0. \tag{5.4}$$

Explicitly, (5.4) is:

$$-\left(\frac{1}{\tau_1}h_1(u)+\frac{\gamma}{\tau_2}h_2(u)\right)+\frac{1}{\tau_2}z+\left(\frac{1}{\tau_1}-\frac{1}{\tau_2}\right)x>0. \tag{5.5}$$

If we define

$$\delta=\frac{1}{\tau_1}-\frac{1}{\tau_2}, \tag{5.6}$$

then (5.5) may be rewritten:

$$-\left(\frac{1}{\tau_1}h_1(u)+\frac{\gamma}{\tau_2}h_2(u)\right)+\frac{1}{\tau_2}G(u)+\delta x>0. \tag{5.7}$$

Letting:

$$\widetilde{T}(u)=\left(\frac{1}{\tau_1}h_1(u)+\frac{\gamma}{\tau_2}h_2(u)\right)-\frac{1}{\tau_2}G(u), \tag{5.8}$$

then the condition in (5.4) is satisfied on $\mathcal{S}_L$ when:

$$x \;<\; \frac{1}{\delta}\widetilde{T}(u) \;\text{ if } \delta<0, \tag{5.9}$$

$$x \;>\; \frac{1}{\delta}\widetilde{T}(u) \;\text{ if } \delta>0. \tag{5.10}$$

Returning to the $(+,-)$ case, we observe that $\delta<0$ and further computations reveal that (5.4) is satisfied in the sense of (5.9). This means that for x values satisfying (5.9) for all $u\in(u_-,u_{\mathrm{HC}})$, trajectories cross each Γ_u toward Γ_- as shown in Figure 32 by the trajectory $\widetilde{\gamma}_+$.

We should remark that the tangency condition $\vec{\mathbf{F}}\cdot\vec{\mathbf{N}}_-\big|_{\Gamma_u}=0$ occurs at a unique $x=\widetilde{X}_{\mathrm{SS}}(u)$ for each u, where

$$\widetilde{X}_{\mathrm{SS}}(u)=\frac{1}{\delta}\widetilde{T}(u). \tag{5.11}$$

We may plot the curve $\widetilde{C}_{\mathrm{SS}}$ parametrized by $\widetilde{R}_{\mathrm{SS}}(u)=\left(\widetilde{X}_{\mathrm{SS}}(u),\widetilde{Y}_{\mathrm{SS}}(u)\right)$ where each tangency occurs for $u<u_-$ and $\widetilde{Y}_{\mathrm{SS}}(u)=\frac{G(u)-\widetilde{X}_{\mathrm{SS}}(u)}{\gamma}$.

In Figure 33 we show several numerically integrated trajectories of (SS) on S_L in the $(+,-)$ case, along with the curve $\widetilde{C}_{\mathrm{SS}}$. It is important to notice, in this

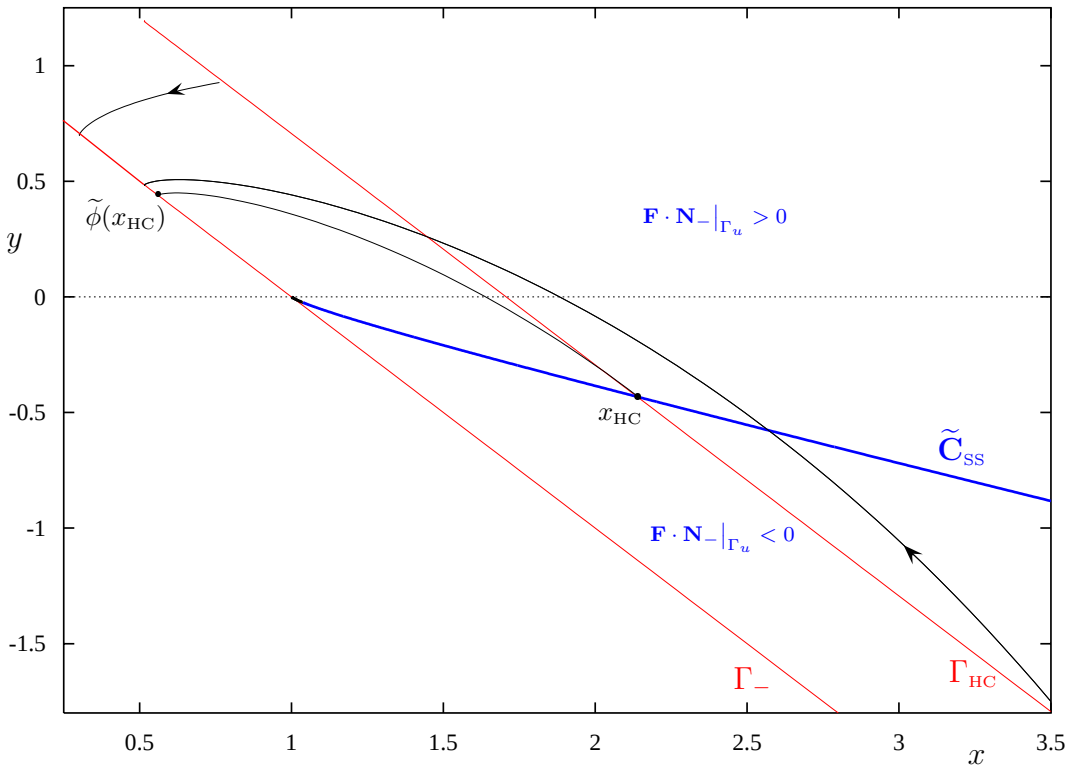


Figure 33: Several (SS) trajectories, in the $(+,-)$ case, along with a plot of the curve $\widetilde{C}_{\rm SS}$ parametrized by $\widetilde{R}_{\rm SS}(u) = (\widetilde{X}_{\rm SS}(u), \widetilde{Y}_{\rm SS}(u))$ for $u < u_-$ where $\widetilde{Y}_{\rm SS}(u) = \frac{G(u)-\widetilde{X}_{\rm SS}(u)}{\gamma}$. The intersection of $\widetilde{C}_{\rm SS}$ with $\Gamma_{\rm HC}$ is indicated by the point $x_{\rm HC}$. The (SS) trajectory originating at that point terminates at the point marked $\widetilde{\phi}(x_{\rm HC})$.

example, that all trajectories above $\widetilde{C}_{\rm SS}$ must cross each Γ_u generally toward Γ_-. We have labeled the point $x_{\rm HC}$, where the curve $\widetilde{C}_{\rm SS}$ intersects $\Gamma_{\rm HC}$. An (SS) trajectory originating at this point starts off tangent to $\Gamma_{\rm HC}$ and then terminates on Γ_- at $\widetilde{\phi}(x_{\rm HC})$, as shown in Figure 33. Note, that trajectories originating at x_0 values on $\Gamma_{\rm HC}$ larger than $x_{\rm HC}$ will proceed to the right and above the trajectory with $x_0 = x_{\rm HC}$, since $\mathbf{F}\cdot\mathbf{N}_-\big|_{\Gamma_u} < 0$ for all trajectories below $\widetilde{C}_{\rm SS}$, as illustrated by the trajectory originating at $x_0 = 3.5$.

With the results of this process, summarized in Figure 33, we are now able to

state that only those $x \leq \widetilde{\phi}(x_{\text{HC}})$ are in the range $R(\widetilde{\phi})$. We explicitly compute the value of $x_{\text{HC}} = \widetilde{X}_{\text{SS}}(u_{\text{HC}})$ using (5.11) as $x_{\text{HC}} = 2.138$ at this intersection. From this we may numerically estimate the value of $\widetilde{\phi}(x_{\text{HC}})$, in this case $\widetilde{\phi}(x_{\text{HC}}) \approx 0.561$. So, for this specific $(+,-)$ case, we have established that the domain and range of $\widetilde{\phi}$, in terms of x, are: $D(\widetilde{\phi}) = \mathbb{R}$ and $R(\widetilde{\phi}) = (-\infty, \widetilde{\phi}(x_{\text{HC}})]$.

To see how this analysis relates back to our $\widetilde{\phi}$ map construction, we observe that in Figure 22 (pg 78) the graph of $\widetilde{\phi}$ reaches a maximum value of about 0.5 for $x \approx 2$. By examining the AUTO generated data file we observe this maximum value is $\widetilde{\phi}(2.13) \approx 0.561$ and for x values larger than $x_{\text{HC}} \approx 2.13$ the $\widetilde{\phi}$ values continue to decrease. Note in particular, the agreement that the maxima occurs very close to $x = \widetilde{X}_{\text{SS}}(u_{\text{HC}})$.

In a similar fashion we can estimate the domain and range of $\widehat{\phi}$. Figure 34 shows the x and y nullclines for (AFS) using the approximation (4.21) for $\widehat{u}(z)$, along with Γ_- and Γ_{HC}. Recall that for x_0 to be in the domain of $\widehat{\phi}$, an (AFS) trajectory in the (x,y)-plane originating on Γ_- at $x = x_0$ must reach Γ_{HC} in finite time.

From Figure 34 it is clear that the domain of $\widehat{\phi}$, in terms of x, is $D(\widehat{\phi}) = \mathbb{R}$. However, it is not clear at this point what is the range of $\widehat{\phi}$.

As we did above for the (SS), we use a normal vector to the constant z lines to assist in this goal. In working with the (AFS) we will use the normal vector $\vec{\mathbf{N}}_+ = (1, \gamma)$ and our (AFS) vector field $\vec{\mathbf{G}} = (\widehat{G}_1, \widehat{G}_2)$ as defined in (2.70)-(2.71):

$$\frac{dx}{dt} = \widehat{G}_1(x,y) \equiv \frac{h_1(\hat{u}(z)) - x}{\tau_1}, \tag{5.12}$$

$$\frac{dy}{dt} = \widehat{G}_2(x,y) \equiv \frac{h_2(\hat{u}(z)) - y}{\tau_2}, \tag{5.13}$$

where $\hat{u}(z)$ was defined in (2.68) as the average value of u on the limit cycles of (FS) and $z = x + \gamma y$. For some calculations, we will use the fit function form given in (4.21).

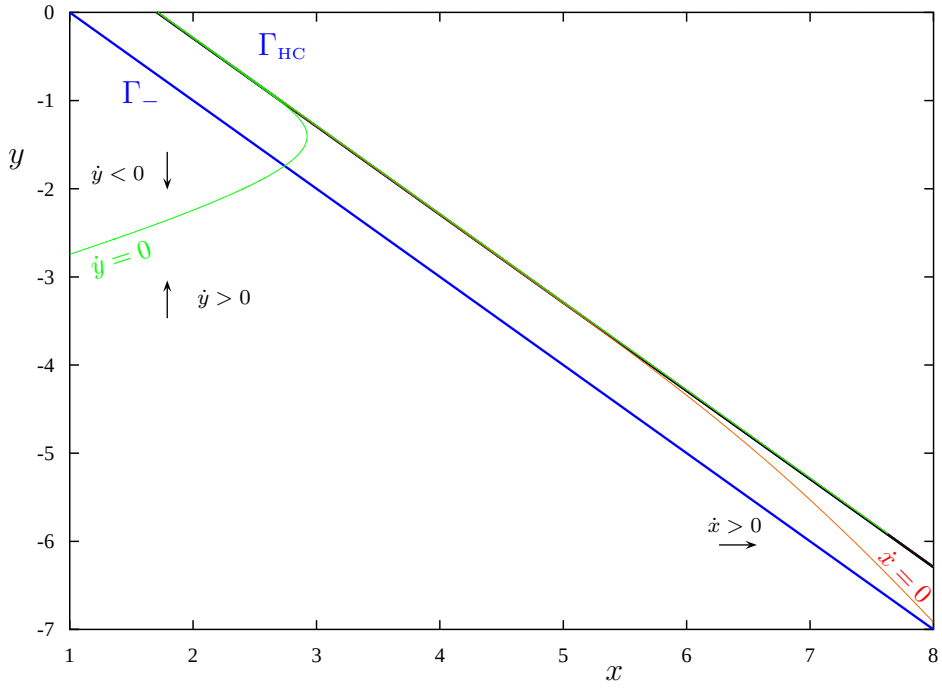


Figure 34: The x and y nullclines of the (AFS) using the approximation (4.21) for $\widehat{u}(z)$, in the $(+,-)$ case. We also indicate the regions in which x and y are increasing/decreasing. The projection of (AFS) trajectories onto the (x,y)-plane which begin on Γ_- must eventually terminate on Γ_{HC}.

The condition that (AFS) trajectories cross an arbitrary Γ_z (constant z line) in the direction toward Γ_{HC} is equivalent to the condition:

$$\mathbf{G} \cdot \mathbf{N}_+\big|_{\Gamma_z} > 0. \tag{5.14}$$

Explicitly, (5.14) is:

$$\left(\frac{1}{\tau_1}h_1(\hat{u}(z)) + \frac{\gamma}{\tau_2}h_2(\hat{u}(z))\right) - \frac{1}{\tau_2}z + \left(\frac{1}{\tau_2} - \frac{1}{\tau_1}\right)x > 0. \tag{5.15}$$

If we define

$$\hat{\delta} = \frac{1}{\tau_2} - \frac{1}{\tau_1}, \tag{5.16}$$

and let:

$$\widehat{T}(z) = -\left(\frac{1}{\tau_1}h_1(\hat{u}(z)) + \frac{\gamma}{\tau_2}h_2(\hat{u}(z))\right) + \frac{1}{\tau_2}z, \tag{5.17}$$

then the condition (5.14) is satisfied when:

$$x < \frac{1}{\hat{\delta}}\widehat{T}(z) \text{ if } \hat{\delta} < 0, \tag{5.18}$$

$$x > \frac{1}{\hat{\delta}}\widehat{T}(z) \text{ if } \hat{\delta} > 0. \tag{5.19}$$

In the $(+,-)$ case, we observe that $\hat{\delta} > 0$ and further computations reveal that (5.4) is satisfied as in (5.19). This means that for x values satisfying (5.19) for all $z < z_{\text{HC}}$, trajectories must cross each Γ_z toward Γ_{HC}.

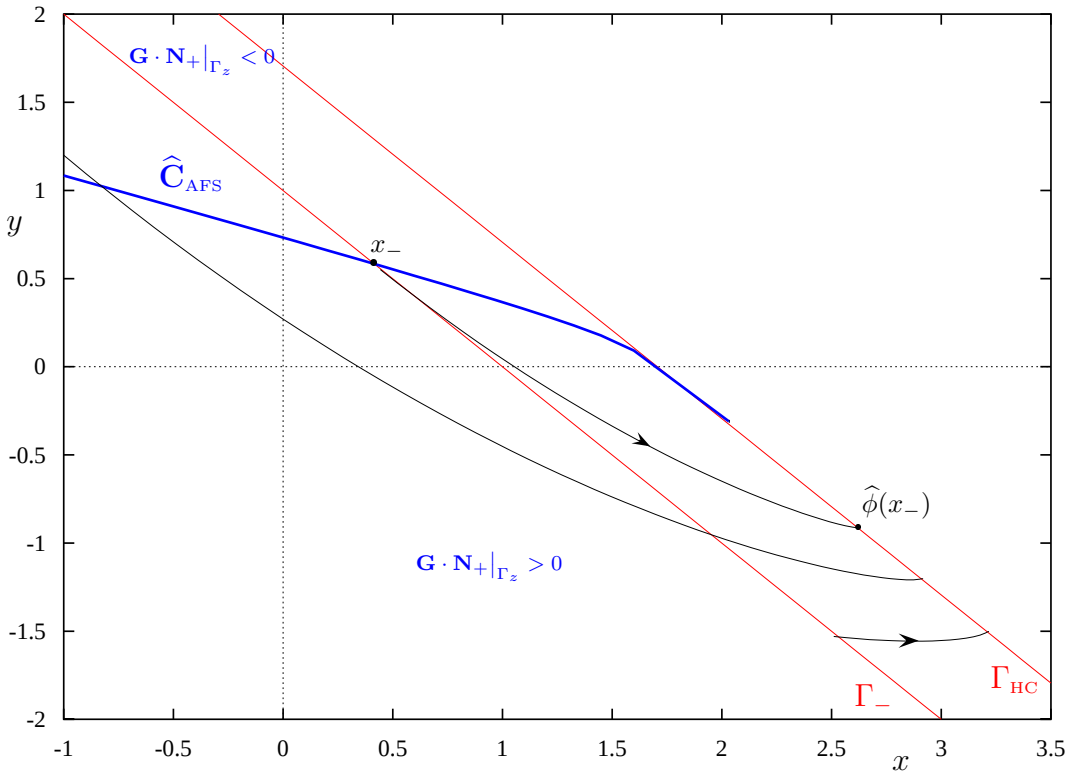


Figure 35: Several projected (AFS) trajectories along with a plot of the curve $\widehat{C}_{\text{AFS}}$ parametrized by $\widehat{R}_{\text{AFS}}(z) = (\widehat{X}_{\text{AFS}}(z), \widehat{Y}_{\text{AFS}}(z))$ for $z < z_{\text{HC}}$ where $\widehat{Y}_{\text{AFS}}(z) = \frac{z - \widehat{X}_{\text{AFS}}(z)}{\gamma}$. The intersection of $\widehat{C}_{\text{AFS}}$ with Γ_- is indicated by the point x_-. The (AFS) trajectory originating at that point terminates at the point marked $\widehat{\phi}(x_-)$.

As was the case with the (SS) analysis, the tangency condition $\mathbf{G} \cdot \mathbf{N}_+\big|_{\Gamma_z} = 0$ occurs at a unique $x = \widehat{X}_{\text{AFS}}(z)$ for each z, where

$$\widehat{X}_{\text{AFS}}(z) = \frac{1}{\hat{\delta}}\,\widehat{T}(z).$$

In Figure 35 we plot the curve $\widehat{C}_{\text{AFS}}$ parametrized by $\widehat{R}_{\text{AFS}}(z) = \left(\widehat{X}_{\text{AFS}}(z), \widehat{Y}_{\text{AFS}}(z)\right)$ where each tangency occurs for $z < z_{\text{HC}}$ and where $\widehat{Y}_{\text{AFS}}(z) = \frac{z - \widehat{X}_{\text{AFS}}(z)}{\gamma}$. Here we have used (4.21) to approximate $\widehat{u}(z)$ and remark that all trajectories below the plotted $\widehat{C}_{\text{AFS}}$ curve must cross each Γ_z generally toward Γ_{HC}.

The intersection of $\widehat{C}_{\text{AFS}}$ with Γ_- is indicated by the point x_-, and is computed here as $x_- \approx 0.416$. An (AFS) trajectory originating at that point starts off tangent to Γ_- and terminates on Γ_{HC} at the point marked $\widehat{\phi}(x_-)$, as shown in Figure 35. In this case, the numerically approximate value is $\widehat{\phi}(x_-) \approx 2.616$. We may now conclude (for $\widehat{u}(z)$ given by (4.21)) that in this particular case the domain and range of $\widehat{\phi}$ are $D(\widehat{\phi}) = \mathbb{R}$ and $R(\widehat{\phi}) = [\widehat{\phi}(x_-), \infty)$. Again, this conclusion supports our numerically generated $\widehat{\phi}$ map as shown in Figure 24 (pg 82), where a minimum value of about $\widehat{\phi} \approx 2.58$ is achieved for $x_- \approx 0.503$. This slight difference in our x_- value is accounted for by the small second derivative of our $\widehat{\phi}$ near the minima and the relatively large Δx used in our AUTO runs.

Thus, we have completely identified the domain and range for $\widetilde{\phi}$ and $\widehat{\phi}$ in this specific $(+,-)$ example, with no equilibrium on $\mathcal{S}_L$. But in order to use Theorem 5.1 we need to identify a closed interval M such that $\phi : M \to M$ and then show that ϕ is contractive on M.

To illustrate how the hypothesis $\phi : M \to M$ of Theorem 5.1 can be verified numerically, we first summarize in Figure 36 points and trajectories needed to identify the ranges $R(\widetilde{\phi})$ and $R(\widehat{\phi})$. Now note that if we choose $M = [0, \widetilde{\phi}(x_{\text{HC}})]$, we would need (global information) to decide how $\widehat{\phi}$ maps M and again to decide how

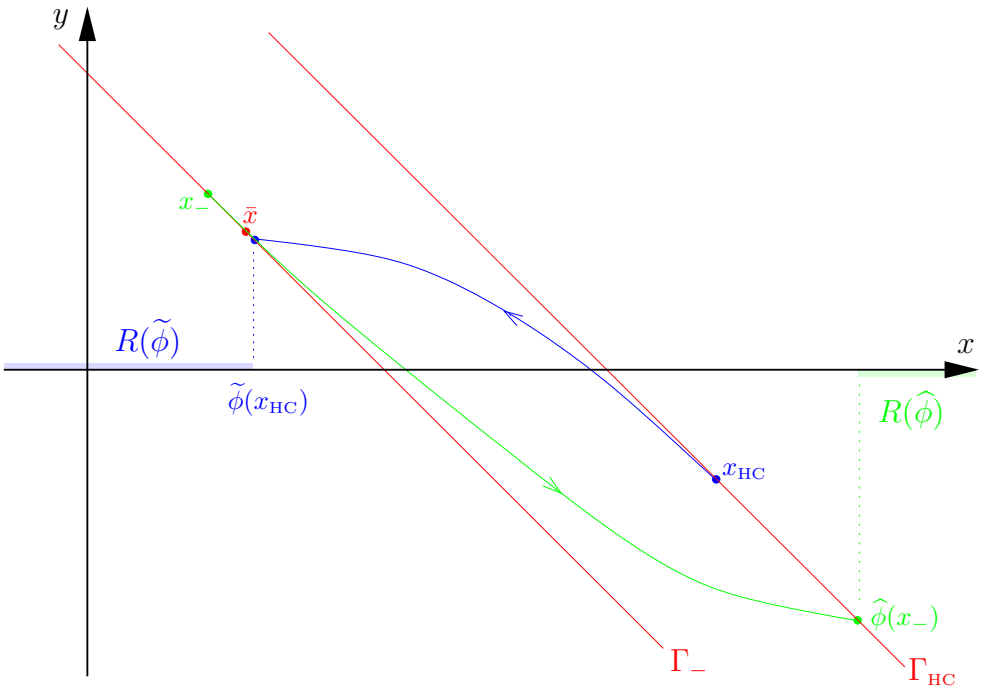


Figure 36: Summary of the range information for the $(+,-)$ example. $\widehat{\phi}$ maps the point x_- as shown, resulting in the range $R(\widehat{\phi})$ as indicated. And $\widetilde{\phi}$ maps the point $x_{\rm HC}$ as shown, with $R(\widetilde{\phi})$ as indicated.

$\widetilde{\phi}$ in turn maps that interval. For the choice $M = [0, \widetilde{\phi}(x_{\rm HC})]$, $\widehat{\phi}(M) \subset D(\widetilde{\phi}) = \mathbb{R}$ so that $\widetilde{\phi}(\widehat{\phi}(M))$ is defined $\forall x \in M$. It is not clear from Figure 36, however, if $\widetilde{\phi}(\widehat{\phi}(M)) \subset M$.

However, utilizing our numerical map construction in Chapter 4, we may determine where $\phi(M)$ gets mapped, with $M = [0, \widetilde{\phi}(x_{\rm HC})]$ as above and noting that $\phi(x_{\rm HC}) \approx 0.56$. First consider the pertinent regions of Figure 24 (AFS) and Figure 22 (SS) shown here in Figure 37. We see that $\widehat{\phi}(M) \subset (2.582, 2.598)$, and then $\widetilde{\phi}(\widehat{\phi}(M)) \subset (0.552, 0.553)$. Thus showing that $\phi(M) \subset M$.

In order to (numerically) verify Theorem 5.1 part (ii) it would be easiest to approximate the value of k in $|\phi(x)-\phi(y)| \leq k|x-y|$ from our numerical computation

of ϕ (Figure 25). Very conservatively we estimate from Figure 25 that $k \approx 0.01$ for pertinent values of x. In this manner one can at least numerically show that ϕ is contractive.

In as much as we have at least numerically verified both hypotheses of Theorem 5.1, we are guaranteed, in this specific case, that there is a unique fixed point of ϕ in M. Our numerical results corroborate this finding with a fixed point $\bar{x}$ of ϕ with $\bar{x} \approx 0.552 \in M$, as shown in Figure 36.

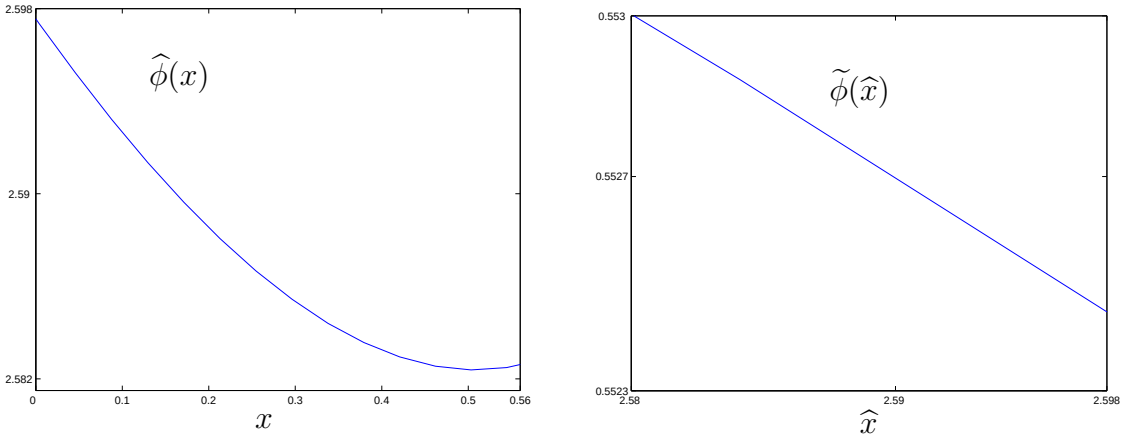


Figure 37: Numerical verification of Theorem 5.1 (i). On the left is shown the interval $M = [0, \widetilde{\phi}(x_{\rm HC})]$ and that $\widehat{\phi}(M) \subset (2.582, 2.598)$. The figure on the right then shows that $\widetilde{\phi}(\widehat{\phi}(M)) \subset (0.552, 0.553)$. Thus, numerically verifying that $\phi(M) \subset M$, ie, $\phi : M \to M$. The parameter values of this $(+,-)$ case are tabulated in Table 3.

To finish this section we will briefly examine the (SS) in our $(+,+)$ case as tabulated in Table 3 (which also has no equilibrium on $\mathcal{S}_L$) to illustrate some issues associated with the AUTO calculations when numerically generating the map.

As with our previous examples, the intersection of $\widetilde{C}_{\rm SS}$ with any of the Γ_u lines may be calculated analytically. With this new $(+,+)$ parameter set, the (SS) curve $\widetilde{C}_{\rm SS}$ approaches Γ_- at a very shallow angle, and intersects at $x = -2.7$. Because

the approach angle is so shallow, the intersection of $\widetilde{C}_{\text{SS}}$ with Γ_{HC} is at the very negative value $x_{\text{HC}} = -24.050$. Interestingly enough, $\widetilde{\phi}(x_{\text{HC}}) \approx 2.70$. Furthermore, in conjunction with the (SS) nullclines (as before) we are able to determine that $D(\widetilde{\phi}) = \mathbb{R}$ and $R(\widetilde{\phi}) = [\widetilde{\phi}(x_{\text{HC}}), \infty)$.

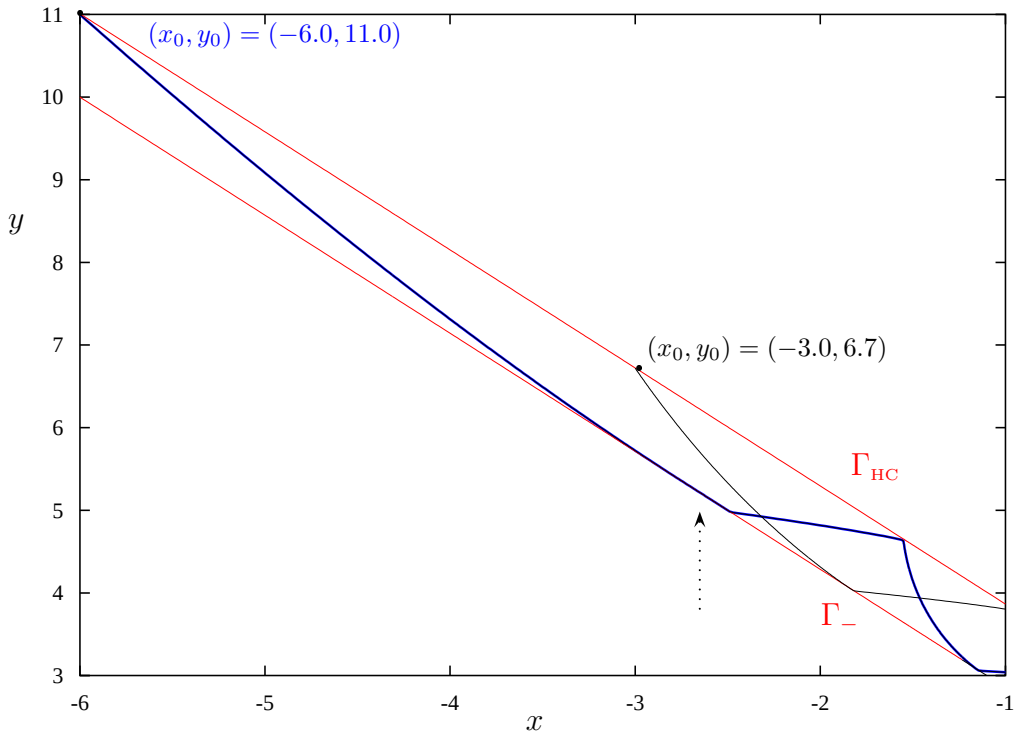


Figure 38: A tangency example in the (SS) of the $(+,+)$ case. (SS) trajectories with $x_0 < -3$ approach Γ_- at a very shallow angle. The arrow indicates this 'near tangency' for the trajectory with initial conditions $(x_0, y_0) = (-6.0, 11.0)$.

We observe that in Figure 22, the graph of the $\widetilde{\phi}$ map construction, begins at $x \approx -6$. As shown in Figure 38, (SS) trajectories with $x_0 < -3$ approach Γ_- at a very shallow angle. The two trajectories shown, with initial conditions (x_0, y_0) as indicated, are actually trajectories of (FULL), since the transition to the active

phase turned out to be helpful in illustrating the end of the (SS) trajectory.

In this case AUTO could not converge to a solution of the boundary value problem when the solutions approached the boundary Γ_- in a tangent fashion. We merely mention the coincidence of this tangency point with the failures in AUTO to solve the boundary value problem (4.1)-(4.6) but as yet have no explanation for this coincidence. In Chapter 4, we did not need to continue solutions past $x_0 = -6$ since the range of x over which $\widetilde{\phi}$ and $\widehat{\phi}$ were calculated were sufficient for the generation of the composition map.

One Equilibrium on $\mathcal{S}_L$

Here we outline some of the similarities and differences in addressing domain and range issues for $\widetilde{\phi}$ when there exists one equilibrium $\mathbf{x}_e$ on $\mathcal{S}_L$. Parameter values for such cases can be determined using results from Chapter 2.

A generic example of a single unstable equilibrium on $\mathcal{S}_L$ in the band between Γ_- and Γ_{HC} is shown in Figure 39. Relating back to Table 2, this is only possible in the $(+,-)$ case. Analysis analogous to that in the previous section would reveal that $D(\widetilde{\phi}) = \mathbb{R}$. Utilizing the Γ_u crossing process of the previous section in the determination of the range, we could now analytically compute the point where the vector field is tangent to Γ_-, as marked $\widetilde{\phi}(x_a)$ in Figure 39. This would allow for an explicit computation of the range boundary, here $R(\widetilde{\phi}) = (-\infty, \widetilde{\phi}(x_a))$. Furthermore, the same methods used in the previous section could be used on a specific example to show the existence of a map fixed point, should one exist. Thus, a single unstable equilibrium on $\mathcal{S}_L$ changes our determination of the domain and range for $\widetilde{\phi}$ very little.

In all of our examples thus far, the domains $D(\widetilde{\phi})$ and $D(\widehat{\phi})$ have been $\mathbb{R}$. This simplifies all discussions involving the composition of the maps $\widetilde{\phi}$ and $\widehat{\phi}$ since then

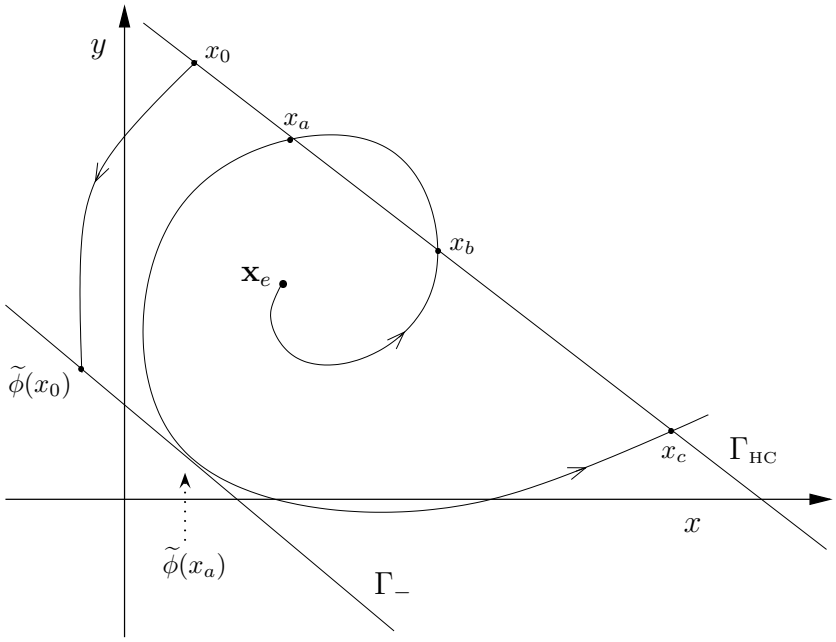


Figure 39: A generic example of a single unstable equilibrium on $\mathcal{S}_L$ in the band between Γ_- and Γ_{HC}. We utilize this figure to to assist in the general discussion of domain and range issues for $\widetilde{\phi}$.

ϕ is defined for at least some x. When the sole equilibrium on $\mathcal{S}_L$ is stable, however, the domain of the map is no longer $D(\widetilde{\phi}) = \mathbb{R}$. Referring to Figure 40, it is clear that x values on Γ_{HC} between the points marked x_a and x_c are not in the domain of $\widetilde{\phi}$, in that (SS) trajectories originating at these points do not reach Γ_- in finite time since they are in the basin of attraction of the fixed point $\mathbf{x}_e$. Other complications include, for example, how $\widehat{\phi}$ maps an interval such as $M = [0, \widetilde{\phi}(x_c)]$. Where $\widehat{\phi}$ maps M determines whether the equilibrium $\mathbf{x}_e$ is globally attracting or whether bursting solutions may persist or both. For example, if M is mapped by $\widehat{\phi}$ to the right of x_c on Γ_{HC} then there exists the possibility of a map fixed point for ϕ.

This last scenario, simultaneous existence of bursting solutions and a stable equilibrium on $\mathcal{S}_L$, warrants further investigation and is the subject of our next section.

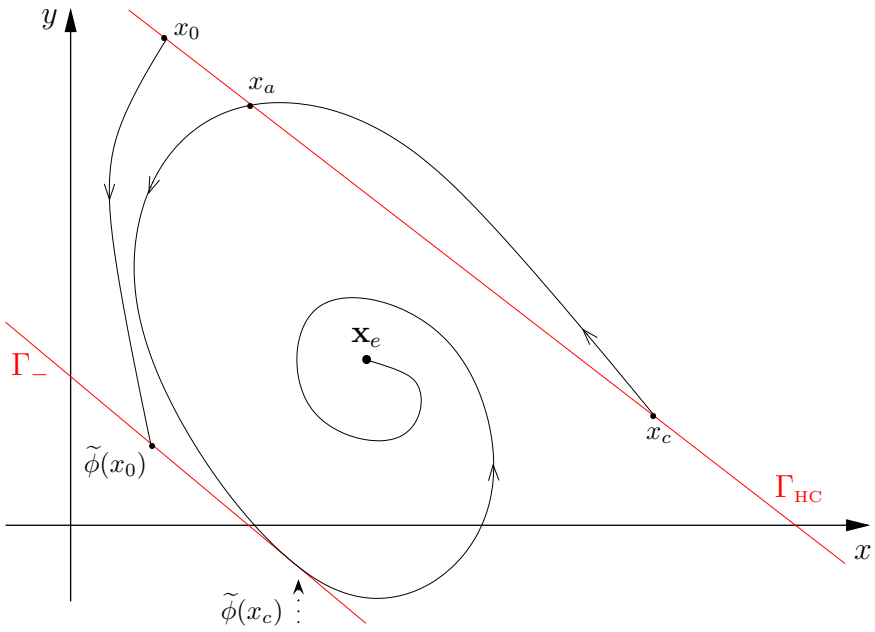


Figure 40: A generic example of a single stable equilibrium on $\mathcal{S}_L$ in the band between Γ_- and Γ_{HC}. We utilize this figure to assist in the general discussion of factors effecting the domain and range of $\widetilde{\phi}$.

Bistability

Bistability refers to the scenario when, for a fixed set of parameters, there exists persistent bursting solutions of (FULL) and at the same time there exists a stable equilibrium on $\mathcal{S}_L$. This bistability is not possible in the degenerate case, which is obvious when one recalls the degenerate case possesses the dynamics equivalent to those of the one slow variable model. Again, we wish to emphasize that when we make reference to a bistable example, we keep all of the parameters fixed and just by changing the initial x and y values we are able to see bursting solutions or attraction toward a stable fixed point for (FULL).

When we began this work, the possibility of bistability was considered but it was

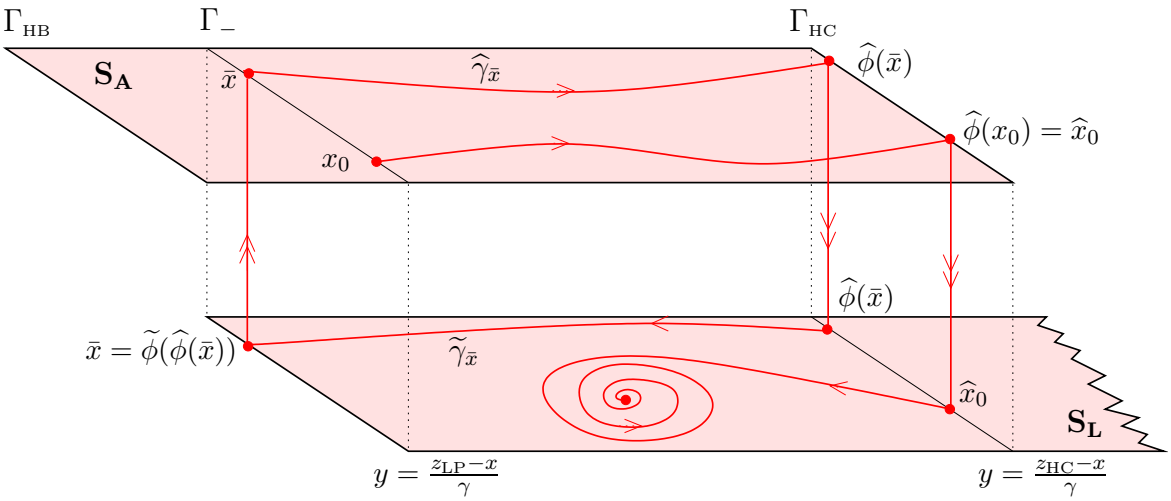


Figure 41: Caricature of a generic bistability example. Shows S_A on top and S_L on the bottom. A bursting cycle is shown originating at $\bar{x}$ (on S_A). Different initial conditions produce solutions attracted to the stable equilibrium on S_L.

not known for some time if it was possible with this model (FULL). Because we had a seven dimensional parameter space (excluding the (FS) parameters) we developed several tools to assist in this process in Chapter 2. The parameter selection for the bistability example of this section was discussed at the end of Chapter 2, as a verification of our process for the location of Hopf points.

In Figure 41 we illustrate a caricature of this bistability, continuing with our convention of referring to points in the (x, y)-plane by the x coordinate. Also, because we are considering the projection of trajectories onto the (x, y)-plane we refer to S_L and S_A in this figure. Beginning on S_A at the point $\bar{x}$, the active phase trajectory ends at the point marked $\widehat{\phi}(\bar{x})$ on Γ_{HC}, followed by a rapid transition to the silent phase. Continuing on S_L, the silent phase trajectory, marked $\widetilde{\gamma}_{\bar{x}}$, ends on Γ_{-} at $\widetilde{\phi}(\widehat{\phi}(\bar{x}))$. Thus, $\bar{x} = \widetilde{\phi}(\widehat{\phi}(\bar{x}))$, so we have a map fixed point corresponding to persistent bursting solutions of (FULL). Had our initial conditions been different, with our initial value at x_0 instead of $\bar{x}$, the active phase would have terminated at $\widehat{x}_0$, which after the transition to S_L would be in the basin of attraction for the

stable equilibrium.

We have determined a number of parameter sets for which this bistability exists. In Figures 42, 43 we show the numerical simulations on (FULL) for one such parameter set. The particular parameter values are:

$$(\beta_1, \alpha_1, \beta_2, \alpha_2, \gamma, \tau_1, \tau_2) = (4, -1, -3, -0.5, 1, 1, 0.3). \tag{5.20}$$

In Figure 42 on the left we see the projection onto the (x, y)-plane of a bursting cycle with $(x_0, y_0) = (-1.34, 2.32)$ on Γ_{HC}. The corresponding u vs t trace is shown on the right illustrating the bursting solution. Thus, for this parameter set, the return map has a fixed point at $\bar{x} = -1.34$.

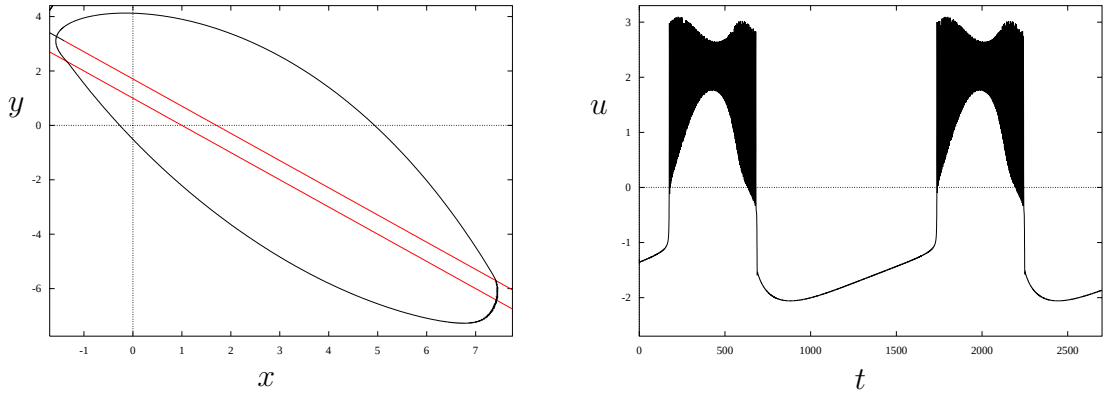


Figure 42: An illustration of bistability. Left: Projection onto (x, y)-plane of a bursting cycle of (FULL); Right: The associated u vs t trace. The slow parameters are as given in (5.20).

In Figure 43 on the left, for the same parameter values, we see the projection onto the (x, y)-plane of a trajectory in the basin of attraction of a stable equilibrium on $\mathcal{S}_L$. As a point of reference, a portion of the bursting solution is shown in the left portion of the figure. Again, the associated u vs t trace is shown on the right.

You may note the similarity between the (SS) parameters we used in this bistability example (5.20) and our $(+, -)$ case, as tabulated in Table 3. With the parameters

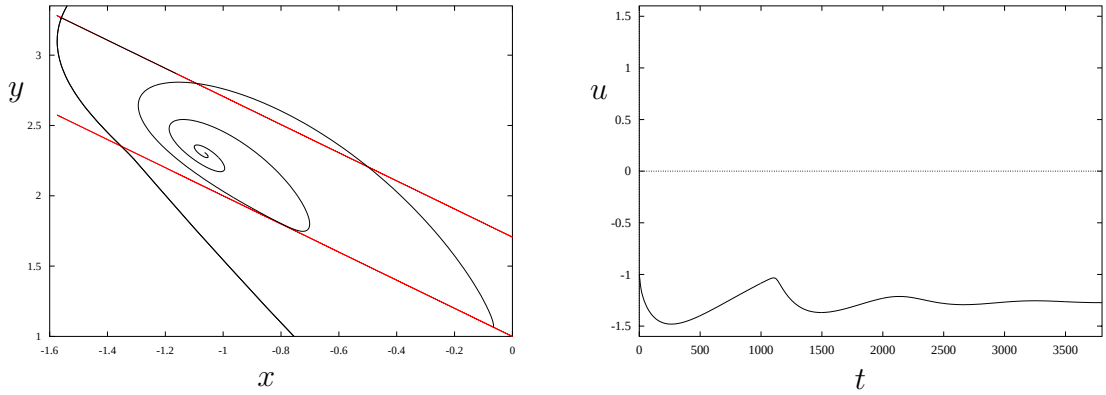


Figure 43: An illustration of bistability. Left: Projection onto (x, y)-plane of a trajectory of (FULL) attracted to the sole stable equilibrium on $\mathcal{S}_L$; Right: The associated u vs t trace. The slow parameters are as given in (5.20).

in the $(+,-)$ case, (FULL) had one equilibrium located on the middle branch (see Figure 20). With the parameters in (5.20) we have three equilibria, one each on the upper, middle and lower branches. The determination of this information was made using some of the tools developed in Chapter 2 and illustrated here in Figure 44 (SS Parameter diagram). The 'A' marked at $(a, b) = (-2.0, -0.5)$ falls in the region where there are three equilibria (see page 41 for more details).

An obvious question at this point, would query the use of the numerical map construction in an example with a stable fixed point on $\mathcal{S}_L$. We did not address this issue in Chapter 4 because we were interested in looking at examples with bursting solutions. The two cases $((+,+),(+,-))$ we have examined were selected because they had a sole equilibrium on $\mathcal{S}_M$, which in the degenerate case guarantees bursting solutions. But now that we have demonstrated one example of bistability we are interested in addressing the use of the map when there is a a stable fixed point on $\mathcal{S}_L$, as in this example.

In Figure 45 we show the numerical map construction of this bistability example. We used AUTO, as we did in Chapter 4, to generate these figures for the parameters

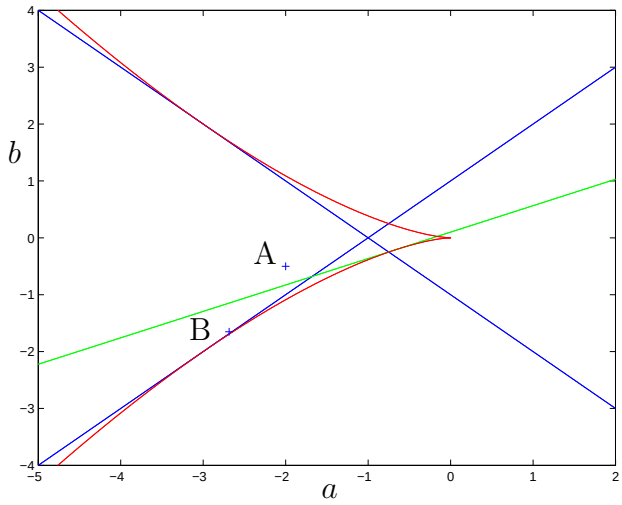


Figure 44: SS Parameter diagram originally as described in Figure 9. The point marked 'A' at $(a, b) = (-2.0, -0.5)$ is computed from the parameters in equation (5.20) for the bistable example discussed in this section. The point marked 'B' at $(a, b) = (-2.7, -1.6)$ is computed from the parameters in equation (5.21) for the example in the next section. Both marks falls in the region where there are three equilibria, one each on the upper branch, middle branch and lower branch.

in (5.20). Figure 45A and Figure 45B show the map construction for $\widehat{\phi}$ and $\widetilde{\phi}$, respectively. We compose the data used to create $\widehat{\phi}$ and $\widetilde{\phi}$ as the composition $\phi = \widetilde{\phi}(\widehat{\phi})$, which is shown in Figure 45C . The dotted line is the line $y = x$, added to facilitate the location of the fixed point $\bar{x}$ of ϕ.

We could again use Theorem 5.1 to numerically verify the existence of a unique fixed point. In keeping with the notation of Figure 40, $x_c \approx -0.519$, $\widetilde{\phi}(x_c) \approx -0.740$ so a choice for M might be $M = [-2, \widetilde{\phi}(x_c)]$. Omitting the details, we find that $\widetilde{\phi}(\widehat{\phi}(M)) \subset [-1.4, -1.3]$ showing $\phi(M) \subset M$ thus verifying the hypothesis $\phi : M \to M$. In order to verify Theorem 5.1(ii) we approximate the contraction k as $k \approx 0.002$. Allowing for the numerical verification of both hypothesis of Theorem 5.1, we guarantee the existence of a unique fixed point of ϕ in M. This numerical construction of the map ϕ yields a fixed point $\bar{x} \approx -1.33 \in M$, which compares

favorably with to our results from Figure 42 for this example, $\bar{x} \approx -1.34$.

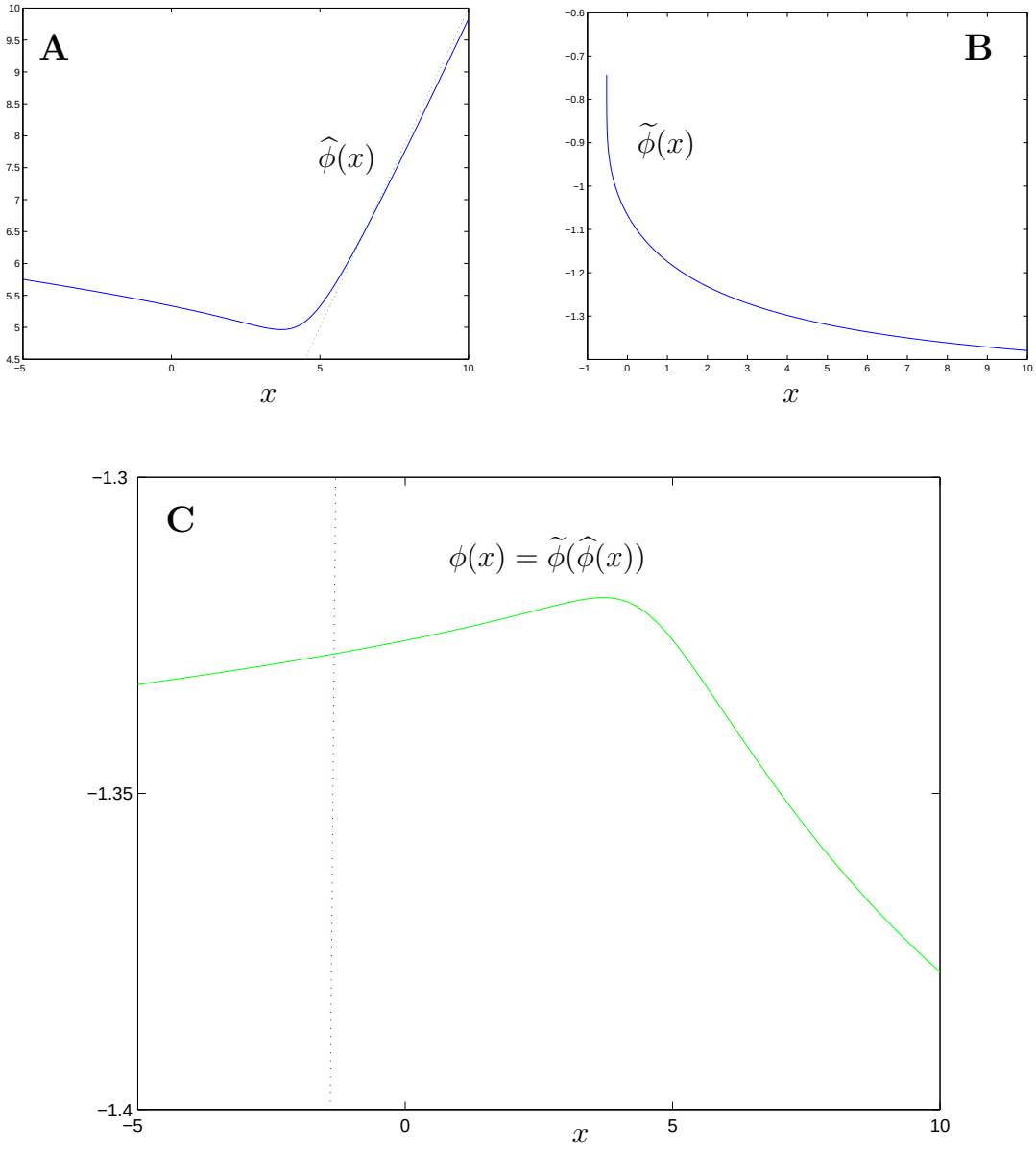


Figure 45: Numerical map construction of this bistability example. As we did in Chapter 4, these figures were generated using AUTO with the parameters in (5.20). A shows the map construction for $\widehat{\phi}$, B shows $\widetilde{\phi}$ and C the composition $\phi = \widetilde{\phi} \circ \widehat{\phi}$. The dotted line in C is the line $y = x$, added to facilitate the location of the numerical approximation of the fixed point $\bar{x}$ of ϕ (here $\bar{x} \approx -1.33$).

Recall that in this bistability example, in addition to the bursting solution we have a stable fixed point on $\mathcal{S}_L$. The fixed point affects $\widetilde{\phi}$ trajectories as illustrated in Figure 40. In this example, we see those effects in Figure 45B, as $x \to x_c^+ \approx -0.52$ then $\widetilde{\phi}(x) \to \widetilde{\phi}(x_c)^- \approx -0.74$. This appears as a vertical asymptote in Figure 45B and is explained by the nearly tangent manner in which trajectories approach Γ_- near $\widetilde{\phi}(x_c)$ (illustrated in the generic example in Figure 40). Furthermore, we know that x values $x \in [x_c, x_a]$ are not in the domain of $\widetilde{\phi}$, which explains why the numerical construction shown in Figure 45B begins at approximately $x \approx -0.5$. This example really has a split domain, there are x values $x < x_a$ in the domain of $\widetilde{\phi}$ as illustrated by the trajectory originating at x_0. However, these x are clearly not relevant to the construction of the map ϕ.

Another Example

With our work in the previous chapters, we should now be able to more easily identify interesting regions in our parameter space. Bistability was covered in the previous section, as it was considered worthy of more detailed discussion. In this section we briefly illustrate one more interesting example.

This example is illustrated in Figure 46 and has parameter values:

$$(\beta_1, \alpha_1, \beta_2, \alpha_2, \gamma, \tau_1, \tau_2) = (1.44, -1.6, -1.25, -0.85, 0.9, 1, 0.2). \tag{5.21}$$

With these parameters (FULL) has three equilibria, as evident in our SS parameter diagram of Figure 44, where these parameters yield a SS parameter diagram pair $(a, b) = (-2.7, -1.6)$ indicated by the marked 'B'. There is a single stable equilibrium on $\mathcal{S}_L$ at $(x, y) = (0.77, 0.27)$, as indicated by the circle in Figure 46A. In addition, (AFS) has a stable equilibrium at $(x, y) = (3.26, -1.89)$ (also shown with a circle), which guarantees continuous spiking solutions [56].

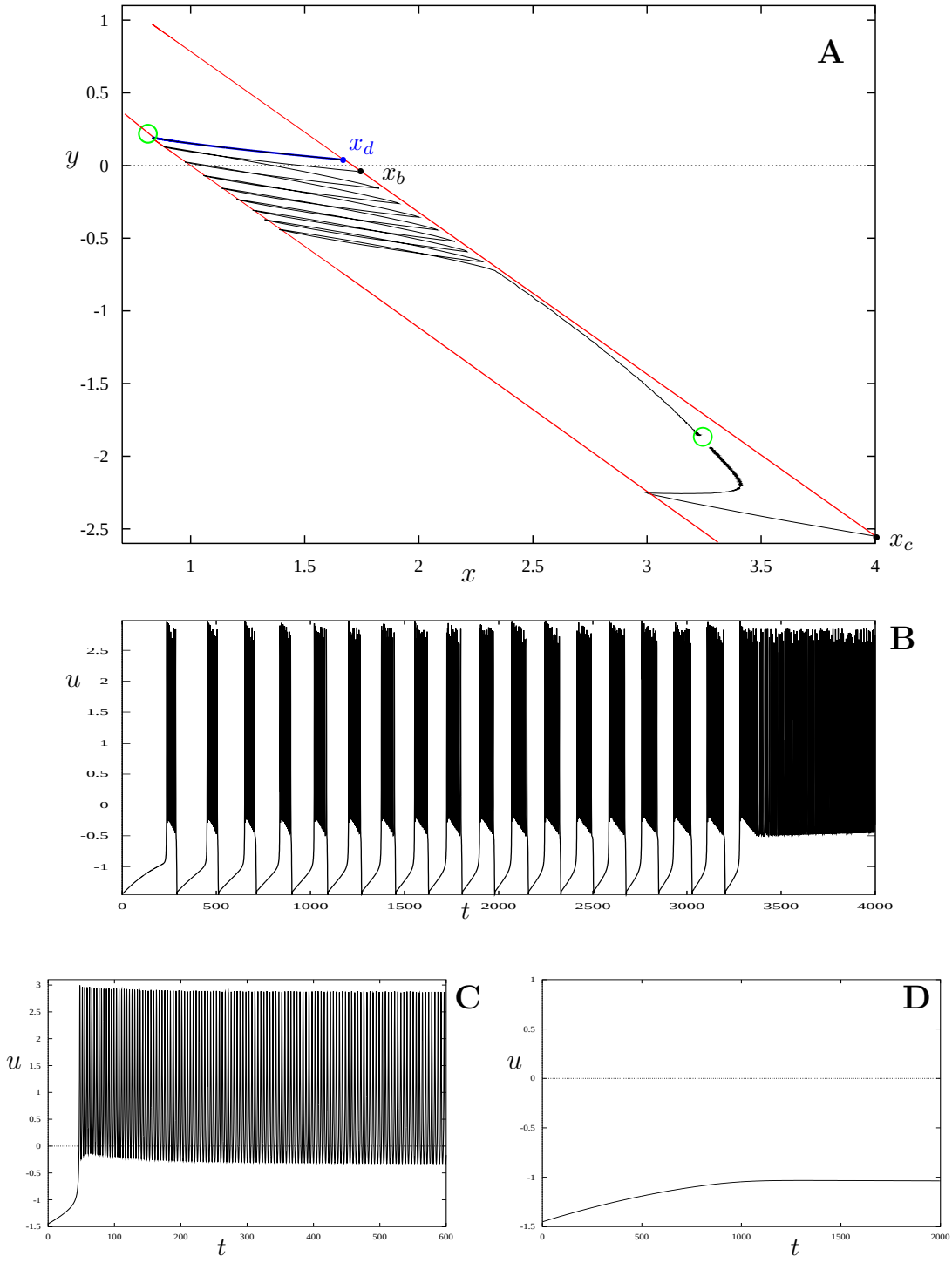


Figure 46: A last example. Figure A shows three trajectories in the (x, y)-plane with initial conditions on $\mathcal{S}_L$ moreover, on the curve Γ_{HC} where x_b, x_c, x_d represents the ordered pairs $(1.74, -0.04)$, $(4, -2.55)$ and $(1.67, 0.04)$, respectively. Parameter values for these simulations are those in (5.21). The u vs t traces for the initial conditions at x_b, x_c and x_d are given in Figures B, C and D, respectively.

For all of the trajectories in this example we indicate the initial values as x_b, x_c and x_d, which all originate on $\mathcal{S}_L$ on the curve Γ_{HC} where x_b, x_c, x_d represents the ordered pairs $(1.74, -0.04)$, $(4, -2.55)$ and $(1.67, 0.04)$, respectively.

The u vs t trace for a trajectory originating at the point marked x_b is shown in Figure 46B. It would appear that we have a bursting solution, contradicting the statement requiring continuous spiking. However, eventually the trajectory is attracted to the (AFS) equilibrium, and constant spiking occurs. For all $x_0 > x_b$ on Γ_{HC} (and (u_0, w_0) initial conditions on $\mathcal{S}_L$) trajectories are attracted to the (AFS) equilibrium. As further support, we also see the trajectory originating at x_c in the basin of attraction, in both Figures 46A and C.

The trajectory originating at x_d is in the basin of attraction of the equilibrium on $\mathcal{S}_L$ (see Figures 46A and D). All trajectories with $x_0 < x_d$ on Γ_{HC} (on $\mathcal{S}_L$) are also attracted to this $\mathcal{S}_L$ equilibrium.

The qualitative features of (FULL) described in this example persist over a range of parameters and ε values. However, we are interested in bursting solutions of (FULL). Examples of this type may lead one to believe that a bursting solution exists, but one does not. Furthermore, bursting is not possible for a range of parameters near those selected for this example.

We have not yet looked at our numerical map construction in an example where there was not a fixed point of the map, in other word where bursting solutions were not possible. We show the map construction for the parameters in (5.21) in Figure 47. Little explanation is needed in the now familiar map illustrations. We remark, that the domain $D(\widetilde{\phi}) = \{x : x > 1.720\}$ in Figure 47B supports our discussion above. More importantly, we see in Figure 47C that the map does not have a fixed point.

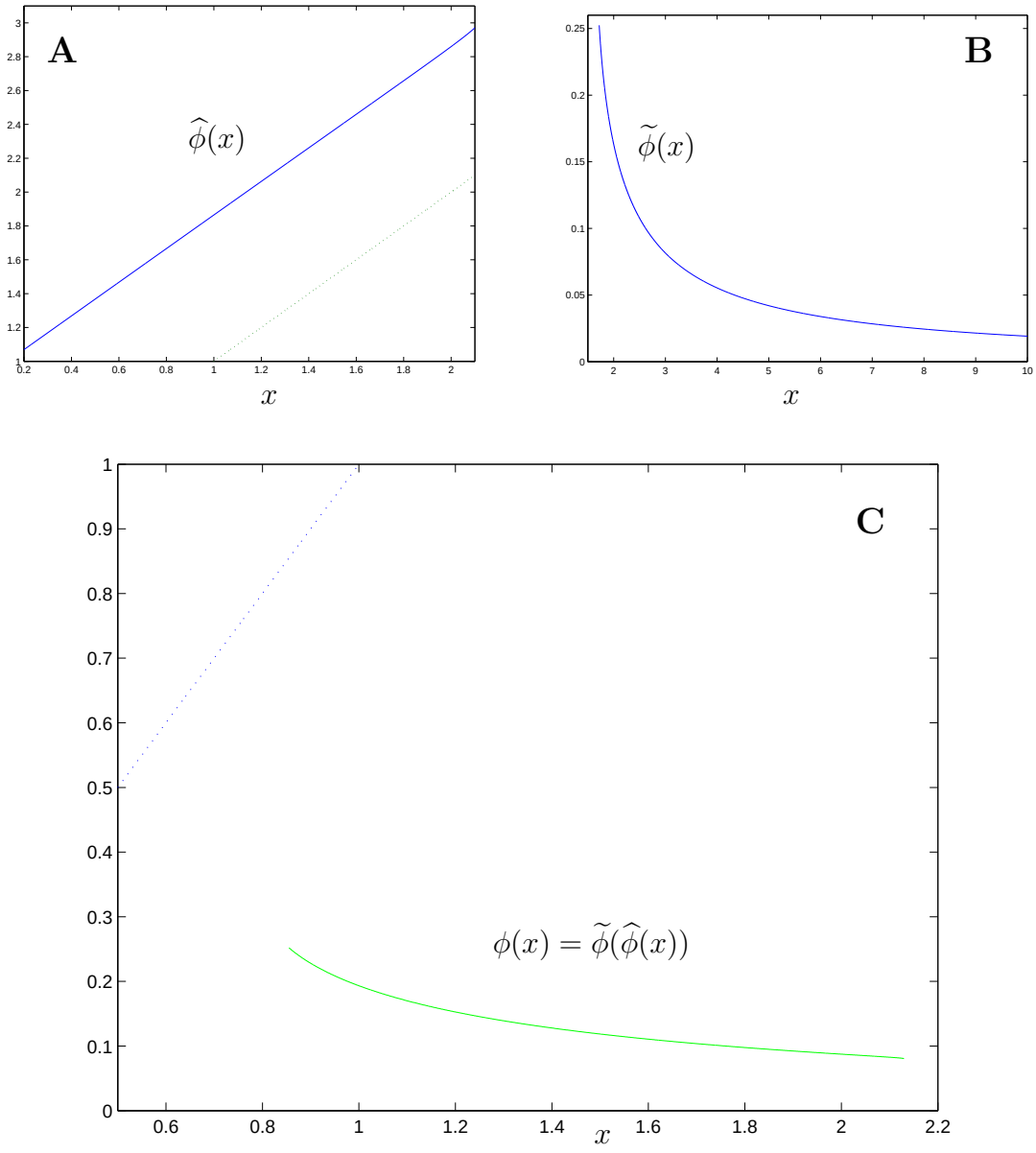


Figure 47: Numerical map construction of this example from Figure 47. AUTO generated map with the parameters in (5.21). A,B and C show the map construction for $\widehat{\phi}$, $\widetilde{\phi}$ and $\phi = \widetilde{\phi} \circ \widehat{\phi}$, respectively. The dotted line in C is the line $y = x$, added to facilitate the location of the fixed point $\bar{x}$ of ϕ, which clearly does not exist in this example. The lack of a map fixed point in this example corresponds to the absence of bursting solutions of (FULL) with these parameters.

CHAPTER 6

CONCLUSIONS AND FUTURE WORK

This thesis has opened many avenues for further exploration. We mention several projects considered for future work. The first such project will be the numerical construction of the map using AUTO. In Chapter 4 we explain our use of AUTO to numerically generate the composite maps $\widehat{\phi}$ and $\widetilde{\phi}$, which we then compose as $\phi = \widetilde{\phi} \circ \widehat{\phi}$ to get the map ϕ. We would like to investigate the feasibility of generating the map ϕ directly using AUTO instead of generating the composite maps separately. If it turns out that this process is possible it will be a great asset in finishing the characterization of the slow parameter space.

In Chapter 2 we began the characterization of the slow parameter space, as to number, location and type of equilibria. A natural project would be the completion of this characterization. As a means for enhancing this project, we would like to delineate regions of the slow parameter space where different classes of bursters are possible, in the classification scheme of Izhikevich (2000) [29]. Throughout this thesis we mentioned the prior work done organizing the fast parameters [42], [14], [3]. We would like to incorporate that complete characterization with our above completed characterization of (SS) into a comprehensive characterization of (FULL). Another project not yet considered, would be a characterization of (AFS) equilibria.

Also, in Chapter 2 we developed a method for determining parameter values such that an equilibrium on $\mathcal{S}_L$ is a Hopf point. But we never addressed the criticality of the Hopf bifurcation. This future work, though not an easy project, would be useful, for example, in locating parameters yielding bistability.

Another project that could be investigated is the perturbation of the degenerate case. Recall, in Chapter 3 we defined the one dimensional return map ϕ. We used

some of the special features of our model to reduce from the two dimensional map $\Phi : \mathbb{R}^2 \to \mathbb{R}^2$, where

$$\Phi(\mathbf{X}) = \Phi \begin{pmatrix} x \\ y \end{pmatrix} = \begin{pmatrix} \phi(x) \\ \frac{z_{HC} - \phi(x)}{\gamma} \end{pmatrix}. \tag{6.1}$$

Were we interested in true solutions as perturbations of the singular limit, Φ in (6.1) might be more appropriately viewed as the leading order term $\bar{\Phi}_0$ in an expansion of the form:

$$\bar{\Phi}(\mathbf{X}, \varepsilon) = \bar{\Phi}_0(\mathbf{X}) + \varepsilon^\alpha \bar{\Phi}_1(\mathbf{X}) + O(\varepsilon^\alpha), \tag{6.2}$$

for some $\alpha > 0$. Such an expansion would need to have more detailed accounts of the dynamics near Γ_- and Γ_{HC} such as that done by Terman [58] when examining models with one slow variable. We did not consider such issues here. Nor did we determine the first order correction term Φ_1, since we were not interested in true solutions, except in their approximation by our singular solutions. Further, our lack of interest in true solutions alleviated associated complications such as whether this approximation does perturb smoothly to the true solution.

In considering perturbations of the degenerate case we would focus our attention on the perturbations of the singular solutions in some other parameter and acknowledge there are many difficulties associated with expansions near the fold bifurcation and the homoclinic bifurcation. We would begin such analysis by defining our perturbation parameter:

$$\delta \equiv \tau_2 - \tau_1, \tag{6.3}$$

and assume an expansion of the form:

$$\bar{\Phi}_0(\mathbf{X}, \delta) = \Phi_0(\mathbf{X}) + \delta \Phi_1(\mathbf{X}) + O(\delta^2), \tag{6.4}$$

where (as we did in the map definition) we construct the map in pieces for the slow and active phases. This particular project would be difficult and at present we are

unsure as to its worth.

Lastly, in Chapter 5 we present Theorem 5.1 to prove the existence of fixed points of the map ϕ. We then develop some tools to determine the domain and range of each of the composite maps $\widehat{\phi}$ and $\widetilde{\phi}$. Subsequently we used these tools to numerically verify the hypotheses of the theorem. We would like to determine trapping regions for these specific examples to extend our 'numerical proof' to an actual proof. With these trapping regions determined for the specific cases discussed we would like to generalize this result to broad classes of (FULL); such as the classification in Chapter 5 for our domain and range discussion. This development could further allow a generalization of the domain and range determination.

REFERENCES CITED

[1] B. Alving, *Spontaneous activity in isolated somata of Aplysia pacemaker neurons*, J. Gen. Physiol., 51 (1968), pp. 29–45.

[2] I. Atwater, C. Dawson, A. Scott, G. Eddlestone, and E. Rojas, *The nature of the oscillatory behavior in electrical activity from pancreatic β-cell*, Hormone and Metabolic Research Supplement, 10 (1980), pp. 100–107.

[3] R. Bertram, M. Butte, T. Kiemel, and A. Sherman, *Topological and phenomenological classification of bursting oscillations*, Bull. Math. Biol., 57 (1995), pp. 413–439.

[4] R. Bertram, J. Previte, A. Sherman, T. Kinard, and L. Satin, *The phantom burster model for pancreatic β-cells*, Biophys. J., 79 (2000), pp. 2880–2892.

[5] R. Bertram, P. Smolen, A. Sherman, D. Mears, I. Atwater, and F. Martin, *A role for calcium release-activated current (CRAC) in cholinergic modulation of electrical activity in pancreatic β-cells*, Biophys. J., 68 (1995), pp. 2323–2332.

[6] W. Beyer, ed., *CRC Standard Mathematical Tables and Formulae*, CRC Press, twenty-ninth ed., 1991.

[7] A. Bose, N. Kopell, and D. Terman, *Almost-synchronous solutions for mutually coupled excitatory neurons*, Physica D, 140 (2000), pp. 69–94.

[8] R. Butera, *Multirhythmic bursting*, Chaos, 8 (1998), pp. 274–284.

[9] T. Chay, *Chaos in a three-variable model of an excitable cell*, Phys. D., 16 (1985), pp. 233–242.

[10] ——, *On the effect of intracellular calcium-sensitive K^+ channel in the bursting pancreatic β-cell*, Biophys. Jour., 50 (1986), pp. 765–777.

[11] ——, *Effect of compartmentalized Ca^{2+} ions on electrical bursting activity of pancreatic β-cells*, Am. J. Physiol., 258 (1990), pp. C955–C965.

[12] T. Chay and D. Cook, *Endogenous bursting patterens in excitable cells*, Math. Biosci, 90 (1988), pp. 139–153.

[13] T. Chay and J. Keizer, *Minimal model for membrane oscillations in the pancreatic β-cell*, Biophys. Jour., 42 (1983), pp. 181–190.

[14] G. de Vries, *Multiple bifurcations in a polynomial model of bursting oscillations*, J. Nonlinear Sc., 8 (1998), pp. 281–316.

[15] G. de Vries and R. Miura, *Analysis of a class of models of bursting electrical activity in pancreatic β-cells*, SIAM J. Appl. Math., 58 (1998), pp. 607–635.

[16] G. de Vries, A. Sherman, and H. Zhu, *Diffusively coupled bursters: effects of cell heterogeneity*, Bull. Math. Biol., 60 (1998), pp. 1167–1200.

[17] M. Deschênes, J. Roy, and M. Steriade, *Thalamic bursting mechanism: an inward slow current revealed by membrane hyperpolarization*, Brain Res., 239 (1982), pp. 289–293.

[18] E. J. Doedel, *AUTO: A program for the automatic bifurcation analysis of autonomous systems*, Cong. Num., 30 (1981), pp. 265–284. Proc. 10th Manitoba Conf. on Num. Math. and Comp., Univ. of Manitoba, Winnipeg, Canada.

[19] B. Ermentrout, *Simulating, Analyzing, and Animating Dynamical Systems: A Guide to XPPAUT for Researchers and Students*, SIAM, Philadelphia, 2002.

[20] R. Fitzhugh, *Impulses and physiological states in theoretical models of nerve membrane*, Biophys. Jour., 1 (1961), pp. 445–466.

[21] J. Hale, *Ordinary Differential Equations*, Krieger, Malabar, Florida, 1980.

[22] R. Harris-Warrick and R. Flamm, *Multiple mechanism of bursting in a conditioned bursting neuron*, J. Neurosci., 7 (1987), pp. 2113–2128.

[23] D. Himmel and T. Chay, *Theoretical studies on the electrical activity of pancreatic β-cells as a function of glucose*, Biophys. Jour., 51 (1987), pp. 89–107.

[24] J. Hindmarsh and R. Rose, *A model of neuronal bursting using three coupled first order differential equations*, Proc. Roy. Soc. London B, 221 (1984), pp. 87–102.

[25] A. Hodgkin and A. Huxley, *A quantitative description of membrane current and its application to conduction and excitation in nerve*, J. Physiol. (London), 117 (1952), pp. 500–544.

[26] M. Holmes, *Introduction to Perturbation Methods*, vol. 20 of Texts in Applied Math., Springer-Verlag, New York, 1995.

[27] F. Hoppensteadt and E. Izhikevich, *Weakly Connected Neural Networks*, vol. 126 of Applied Mathematical Sciences, Springer-Verlag, 1997.

[28] ——, *Thalamo-cortical interactions modeled by weakly connected oscillators: could the brain us FM radio principles?*, Biosystems, 48 (1998), pp. 85–94.

[29] E. Izhikevich, *Neural excitability, spiking and bursting*, Inter. J. of Bifurcation and Chaos, 10 (2000), pp. 1171–1266.

[30] ——, *Subcritical elliptic bursting of bautin type*, SIAM J. Appl. Math., 60 (2000), pp. 503–535.

[31] E. Izhikevich, N. Desai, E. Walcott, and F. Hoppensteadt, *Bursts as a unit of neural information: selective communication via resonance*, Trends in Neurosci., in press, (2003).

[32] J. Keener and J. Sneyd, *Mathematical Physiology*, Springer-Verlag, New York, 1998.

[33] J. Keizer and G. Magnus, *Atp-sensitive potassium channel and bursting in the pancreatic β cell*, Biophys. J., 56 (1989), pp. 229–242.

[34] J. Keizer and P. Smolen, *Bursting electrical activity in pancreatic β-cells caused by Ca^{2+} - and voltage-inactivated Ca^{2+} channels*, Proc. Natl. Acad. Sci., 88 (1991), pp. 3897–3901.

[35] A. Kepecs and X. Wang, *Analysis of complex bursting in cortical pyramidal neuron models*, Neurocomputing, 32-33 (2000), pp. 181–187.

[36] J. Kevorkian and J. Cole, *Perturbation Methods in Applied Mathematics*, Springer-Verlag, New York, 1981.

[37] I. Levitan and L. Kaczmarek, *The Neuron: Cell and Molecular Biology*, Oxford University Press, New York, third ed., 2002.

[38] J. Lisman, *Bursts as a unit of neural information: making unreliable synapses reliable*, Trends in Neurosci., 20 (1997), pp. 38–43.

[39] C. Morris and H. Lecar, *Voltage oscillations in the barnacle giant muscle fiber*, Biophys. Jour., 35 (1981), pp. 193–213.

[40] J. Nicholls, A. Martin, B. Wallace, and P. Fuchs, *From Neuron to Brain*, Sinauer Associates, Inc., Sunderland, MA, USA, fourth ed., 2001.

[41] M. Pernarowski, *The Mathematical Analysis of Bursting Electrical Activity in Pancreatic Beta Cells*, PhD thesis, University of Washington, Seattle, WA, 1990.

[42] ——, *Fast subsystem bifurcations in a slowly varying Liénard system exhibiting bursting*, SIAM J. Appl. Math., 54 (1994), pp. 814–832.

[43] ——, *Fast and slow subsystems for a continuum model of bursting activity in the pancreatic islet*, SIAM J. Appl. Math., 58 (1998), pp. 1667–1687.

[44] M. Pernarowski, R. Miura, and J. Kevorkian, *Perturbation techniques for models of bursting electrical activity in the pancreatic β-cell*, SIAM J. Appl. Math., 52 (1992), pp. 1627–1650.

[45] R. Plant and M. Kim, *Mathematical description of a bursting pacemaker neuron by a modification of the Hodgkin-Huxley equations*, Biophys. Jour., 16 (1976), pp. 227–244.

[46] Purves, Augustine, Fitzpatrick, Katz, LaMantia, McNamara, and Williams, eds., *Neuroscience*, Sinauer Associates, Inc., Sunderland, MA, USA, second ed., 2001.

[47] J. Rinzel, *Bursting oscillations in an excitable membrane model*, in Ordinary and Partial Differential Equations, B. Sleeman and R. Jarvis, eds., vol. 1151 of Lecture Notes in Math., Springer-Verlag, New York, 1985, pp. 304–316.

[48] ——, *A formal classification of bursting mechanisms in excitable systems*, in Mathematical Topics in Population Biology, Morphogenesis, and Neurosciences, E. Teramato and M. Yamaguti, eds., vol. 71 of Lecture Notes in Biomathematics, Springer-Verlag, Berlin, 1987, pp. 267–281.

[49] J. Sanders and F. Verhulst, *Averaging Methods in Nonlinear Dynamical Systems*, vol. 59 of Applied Mathematical Sciences, Springer-Verlag, New York, 1985.

[50] A. Sherman, *Anti-phase, asymmetric and aperiodic oscillations in excitable cells - I. coupled bursters*, Bull. Math. Biol., 56 (1994), pp. 811–835.

[51] A. Sherman, *Case Studies in Mathematical Modeling—Ecology, Physiology, and Cell Biology*, Prentice-Hall, 1997, ch. Calcium and Membrane Potential Oscillations in Pancreatic β-Cells,, pp. 199–217.

[52] A. Sherman and J. Rinzel, *Model for synchronization of pancreatic β-cells by gap junctions*, Biophys. Jour., 59 (1991), pp. 547–559.

[53] A. Sherman, J. Rinzel, and J. Keizer, *Emergence of organized bursting in clusters of panreactic β-cells by channel sharing*, Biophys. Jour., 54 (1988), pp. 411–425.

[54] P. Smolen and J. Keizer, *Slow voltage-inactivation of Ca^{2+} currents and bursting mechanisms for the mouse pancreatic β-cell*, J. Memb. Biol., 127 (1992), pp. 9–19.

[55] P. Smolen, J. Rinzel, and A. Sherman, *Why pancreatic islets burst but single β-cells do not: The heterogeneity hypothesis*, Biophys. J., 64 (1993), pp. 1668–1680.

[56] P. Smolen, D. Terman, and J. Rinzel, *Properties of a bursting model with two slow inhibitory variables*, SIAM J. Appl. Math., 53 (1993), pp. 861–892.

[57] F. Strumwasser, *Types of information stored in single neurons*, in Invertebrate Nervous Systems: Their Significance for Mammalian Neurophysiology, C. Wiersma, ed., The University of Chicago Press, Chicago, 1967, pp. 290–319.

[58] D. Terman, *Chaotic spikes arising from a model for bursting in excitable membranes*, SIAM J. Appl. Math., 51 (1991), pp. 1418–1450.

[59] F. Verhulst, *Nonlinear Differential Equations and Dynamical Systems*, Springer-Verlag, Berlin, 1990.

[60] X. Wang, *Fast burst firing and short-term synaptic plasticity: a model of neocortical chattering neurons*, Neuroscience, 89 (1999), pp. 347–362.

[61] R. Wong and D. Prince, *Afterpotential generation in hippocampal pyramidal cells*, J. Neurophysiol., 45 (1981), pp. 86–97.

[62] E. Zeidler, *Applied Functional Analysis, Applications to Mathematical Physics*, vol. 108 of Applied Mathematical Sciences, Springer-Verlag, New York, 1995.